Boundary-interior exchanges controlling the labrador sea dynamics

Georgiou, S.

DOI
10.4233/uuid:37028134-4e97-46b3-a50b-54ab2cdc25c4

Publication date
2021

Document Version
Final published version

Citation (APA)
Georgiou, S. (2021). *Boundary-interior exchanges controlling the labrador sea dynamics*. [Dissertation (TU Delft), Delft University of Technology]. https://doi.org/10.4233/uuid:37028134-4e97-46b3-a50b-54ab2cdc25c4

BOUNDARY-INTERIOR EXCHANGES CONTROLLING THE LABRADOR SEA DYNAMICS

BOUNDARY-INTERIOR EXCHANGES CONTROLLING THE LABRADOR SEA DYNAMICS

Dissertation

for the purpose of obtaining the degree of doctor
at Delft University of Technology,
by the authority of Rector Magnificus, prof.dr.ir. T.H.J.J. van der Hagen,
chair of the Board for Doctorates,
to be defended publicly on
Wednesday 24 March 2021 at 15:00 o'clock

by

Sotiria GEORGIOU

Master of Science in Environmental Physics,
University of Athens, Athens, Greece.
born in Athens, Greece.

This dissertation has been approved by the promotor and the copromotor.

Composition of the doctoral committee:

Rector Magnificus,	chairperson
Prof.dr. J.D. Pietrzak,	Delft University of Technology, promotor
Dr. C.A. Katsman,	Delft University of Technology, copromotor

Independent members:

Prof.dr.ir. A.J.H.M. Reniers,	Delft University of Technology
Prof.dr. H. Johnson,	University of Oxford, United Kingdom
Prof.dr. P.N. Holliday,	National Oceanography Centre, United Kingdom
Dr.ir. R. Gelderloos,	Johns Hopkins University, United States
Dr. M.F. de Jong,	Royal Netherlands Institute for Sea Research
Prof.dr.ir. S.G.J. Aarninkhof,	Delft University of Technology, reserve member

This research was carried out with the financial support of the Netherlands Organization for Scientific Research (NWO) through the VIDI-Grand 864.13.011.

Printed by: Proefschrift All In One (AIO)
Cover by: Christos Georgiou

ISBN 978-94-6366-390-8

Λόγος
το καράβι μου
πανιά οι λέξεις μου
να ταξιδέψω μακριά
σ΄ Ιθάκες ονειρεμένες

Ανδρέας Χ. Γεωργίου

Contents

Summary

The Atlantic Meridional Overturning Circulation (AMOC) quantifies the strength of the northward surface transports and southward deeper transports in the Atlantic Ocean. In particular, as warm surface waters flow northward in the Atlantic they gradually cool on they journey releasing heat to the atmosphere. Then, in the subpolar and polar regions these surface waters become dense enough to sink forming cold deep waters, which return southward through the Atlantic Ocean. This oceanic circulation pattern is of high importance for the Earth's climate since it is the main distributor of heat, biogeochemical tracers and water masses globally. For decades, both the ocean and climate communities have focused on understanding the dynamics that shape the AMOC strength and most importantly its variability. Although, a lot of progress has been made towards this goal, it is still unclear how the AMOC will respond in a changing climate.

Observational and numerical modelling studies are focusing on regions within the Atlantic Ocean that are known to play an important role in shaping the AMOC dynamics. Marginal seas are considered to be such key regions. There the deep waters are formed and then are transported to the global ocean. Although deep water formation regions are located in the interior of the marginal seas it is known that they are not associated with net vertical motions. Instead, several studies suggest that the net downwelling occurs along the perimeter of the marginal seas and that the ocean eddies play an important role in regulating this process. The Labrador Sea, which is located between the west coast of Greenland and the Labrador Peninsula, is known to be one of these key regions in the subpolar North Atlantic. It is characterized by a rich activity of different scale vortices (eddies) that act as a bridge between the boundary current system that encircles the basin and its interior. Therefore, a daunting challenge in physical oceanography is to understand how the ocean eddies interact with the large-scale circulation that sets the strength of the AMOC. This thesis aims to provide a better understanding of the role of the interactions between the boundary current and the interior of the Labrador Sea on its dynamics. It employs a combination of an idealized model, a realistic model and observational data to probe the connection between the key physical processes that shape the Labrador Sea dynamics. Furthermore, it examines to what extent changes in the surface heat fluxes can affect these connections and thus the Labrador Sea dynamics.

Over the last decades, there has been significant progress in the numerical modelling of the ocean. Unfortunately, resolving oceanic eddies in global, long simulations is still a challenge for the numerical modelling community. This is due to the fact that a sufficient horizontal resolution is required to resolve such processes, which results in computationally expensive simulations. Idealized configurations of numerical models allow the use of high horizontal resolution and facilitate the investigation of certain physical processes. In this thesis, an idealized eddy-resolving model is employed to examine the interplay between the ocean eddies, the deep water formation process and the downwelling in the Labrador Sea. The results highlight the necessity of properly resolving the eddy activity in the Labrador Sea in order to represent the downwelling and overturning in the North Atlantic Ocean, and also to predict its response to changing environmental conditions.

There is a limited understanding of how the locally formed water mass leaves the interior of the Labrador Sea. An additional objective of this thesis is to investigate the pathways and the transformation of the water masses in a reference frame that moves along with the flow. This is done by using a Lagrangian particle tracking tool which is initialized by the three-dimensional velocity fields from both idealized and realistic ocean models. In particular, numerical particles are released within the boundary current at the exit of the Labrador Sea and are traced backwards in time. The results presented in this thesis reveal that prior to exiting the domain the water masses follow either a fast, direct route within the boundary current or a slow, indirect route that involves boundary current-interior exchanges. These exchanges are regulated by the presence of mesoscale eddies. Additional analyses of Argo float trajectories confirm the existence of these routes. Moreover, it is shown that the water mass transformation along these routes differs. Denser waters are formed in the interior of the basin and follow the indirect route to exit the basin. Instead, lighter waters are formed within or close to the boundary current and follow the direct route to leave the basin. This means that boundary-interior exchanges are important for the pathways and the properties of the water masses that exit the Labrador Sea. This underlines the necessity of resolving the mesoscale features required to capture the interior-boundary current exchange in order to correctly represent the export of the newly-formed water masses.

In a changing climate, to accurately make future climate projections, it is necessary to improve our knowledge on how the ocean affects the climate and vice versa. In this thesis, the response of the dynamics of a marginal sea subjected to surface heat loss, such as the Labrador Sea, to changes in the atmospheric forcing is investigated. The results show that complex interactions between the boundary current and interior are established via the eddy activity, and in concert determine the downwelling in the basin as well as the process of deep water formation. Furthermore, the results reveal that in a colder (warmer) regime the strength of the upstream pathways of the water masses exiting the Labrador Sea is affected in a non-linear way and also the transformation of these water masses results in denser (lighter) water masses. The latter, yields a shift of the local overturning maximum in density space towards a higher (lower) density layer.

Taken together, this dissertation emphasizes the importance of the interaction between the boundary current and the interior of the Labrador Sea for the dynamics of the basin. In particular, it highlights the crucial role of the eddies for the transformation and export of deep waters and the associated timescales from the basin to the global ocean. Furthermore, the results presented in this thesis show that the response of the Labrador Sea dynamics to changes in the atmospheric forcing is indirect mainly due to the presence of the rich eddy activity in the basin. Therefore, it is essential to improve our understanding of the boundary current-interior interaction in the marginal seas of the North Atlantic to reduce uncertainty in the estimates of the AMOC and thus, future climate predictions.

Samenvatting[1]

In de Atlantische Oceaan stromen de ondiepe watermassa's noordwaarts en de dieper gelegen watermassa's zuidwaarts. Als de warme ondiepe watermassa's noordwaarts stromen, geven ze warmte af aan de atmosfeer. Hierdoor koelen ze af en daardoor neemt hun dichtheid toe. De dichtheid van deze afgekoelde watermassa's is in de (sub)polaire regio's hoog genoeg om de koude diepe watermassa's te vormen die op diepte terugstromen in zuidwaartse richting. Deze circulatie is van groot belang voor het klimaat, omdat het de verspreiding van warmte, biochemische tracers en watermassa's in de oceaan bepaald.

De AMOC ('Atlantic Meridional Overturning Circulation') is een graadmeter voor de sterkte van deze grootschalige circulatie. Omdat variaties in de grootte van de AMOC direct gevolgen hebben voor het klimaat, hebben oceaan- en klimaatwetenschappers in de afgelopen decennia geprobeerd om de dynamica en de tijdsvariaties van AMOC te begrijpen. Ondanks dat er op dit gebied al veel vooruitgang is geboekt, is het nog niet bekend hoe de AMOC zal veranderen door klimaatverandering.

Een cruciaal onderdeel van deze circulatie is de connectie tussen de noordwaarts stromende ondiepe en de zuidwaarts stromende diepe watermassa's. Deze diepe watermassa's ontstaan in verschillende randzeeën van de Atlantische Oceaan. Onderzoek heeft aangetoond dat de eigenschappen van deze diepe watermassa's ver van de kust bepaald worden, maar dat het verticale transport dicht bij de kust plaatsvindt.

De Labradorzee is zo'n randzee. De Labradorzee ligt in de Noord Atlantische Oceaan tussen Groenland en het Canadese schiereiland Labrador. Deze zee heeft een breed scala aan oceaanwervels. Omdat de oceaanwervels de sterkte van het verticale transport beïnvloeden, is het onduidelijk hoe de dynamica in de Labradorzee de sterkte van AMOC beïnvloedt. In dit proefschrift wordt gekeken naar de invloed van oceaanwervels op de interactie tussen de stromingen langs de kust en de aflandige gebieden in de Labradorzee. Hiervoor worden plaatselijke metingen en modellen met versimpelde en realistische configuraties gebruikt.

De versimpelde configuratie van de Labradorzee wordt gebruikt om te kijken hoe verschillende processen de dynamica beïnvloeden. In deze configuratie kan, in tegenstelling tot lange simulaties in mondiale modellen, een hoge resolutie gebruikt worden. Met deze hoge resolutie kunnen oceaanwervels worden gemodelleerd, en kan dus de wisselwerking tussen de wervels, het ontstaan van diepe watermassa's en het verticale transport in de Labradorzee onderzocht worden. De resultaten tonen aan dat de oceaanwervels noodzakelijk zijn voor de totstandkoming van het verticale transport. Deze wervels zijn daarom nodig om accurate voorspellingen te doen van de grootschalige circulatie in de Noord-Atlantische Oceaan.

---

translated in Dutch by Carine van der Boog

Een combinatie van versimpelde en realistische configuraties wordt gebruikt om te onderzoeken hoe de nieuwgevormde diepe watermassa's hun ontstaansregio in de Labradorzee verlaten. Hiervoor wordt een methode gebruikt waarin het referentiekader met de stroming meebeweegt. Dit referentiekader wordt geïmplementeerd met daartoe ontwikkelde Lagrangiaanse deeltjesvolger die gebruik maakt van driedimensionale snelheidsvelden. Het voordeel hiervan is dat daardoor tegelijkertijd veranderingen in de eigenschappen van deze watermassa's kan worden onderzocht.

In beide configuraties worden numerieke waterdeeltjes losgelaten in de uitstroom van de Labradorzee en vervolgens terug in de tijd gevolgd. De resultaten laten zien dat, voordat de watermassa's de Labradorzee uitstromen, deze een directe of indirecte route volgen. De directe route is relatief snel en volgt de krachtige stromingen langs de kust. In de indirecte route is er een uitwisseling met aflandige gebieden. Deze uitwisseling wordt gereguleerd door oceaanwervels. De aanwezigheid van deze routes is bevestigd met behulp van plaatselijke metingen van Argo boeien.

Daarnaast geven de resultaten van de Lagrangiaanse deeltjesvolger en van deze Argoboeien aan dat eigenschappen van watermassa's veranderen langs hun pad. De deeltjes die de indirecte route volgen hebben gemiddeld een hogere dichtheid als ze de Labradorzee uitstromen. Dit komt omdat deze deeltjes een uitwisseling hebben met de aflandige gebieden waar de diepe watermassa's met een hoge dichtheid worden gevormd. De deeltjes die de directe route volgen hebben gemiddeld een relatief lage dichtheid. Deze dichtheid komt overeen met de dichtheid van de watermassa's die ontstaan in de krachtige stroming langs de kust.

Omdat de directe en indirecte route verschillende watermassa's in de uitstroom representeren, is het belangrijk om uitwisseling tussen het water dichtbij en ver van de kust te begrijpen. Deze uitwisseling bepaald namelijk de verhouding van het aantal deeltjes die de directe of indirecte route nemen. Deze uitwisseling vindt plaats op de mesoschaal. Daarom is het noodzakelijk om deze processen, waaronder de oceaanwervels, te modelleren. Op die manier kan de uitstroom van watermassa's uit de Labradorzee correct weergegeven worden.

Het ontstaan van watermassa's en de sterkte van het verticale transport in de Labradorzee wordt beïnvloed door de temperatuur van de atmosfeer. In dit proefschrift wordt dit verband verder onderzocht met een model met een versimpelde configuratie. De resultaten tonen aan dat een koelere (warmere) atmosfeer resulteert in watermassa's met een hogere (lagere) dichtheid. Deze dichtheidsverschillen worden onder andere veroorzaakt doordat de temperatuur van atmosfeer de sterkte van de stromingen reguleert. Deze dichtheidsverschillen veroorzaken, op hun beurt, een verschuiving van het maximale verticale transport naar watermassa's met hogere (lagere) dichtheden.

Samengevat benadrukt dit proefschrift het belang van de wisselwerking tussen de kuststroming en de aflandige gebieden in de Labradorzee. Er is aangetoond dat de oceaanwervels een cruciale rol middels hun invloed op het ontstaan, de transformatie en de tijdsvariabiliteit van de watermassa's. Daarnaast tonen de resultaten in dit proefschrift aan dat atmosfeer de dynamica van de Labradorzee ook indirect beïnvloed via de oceaanwervels. Daarom is het belangrijk om deze wisselwerking nog beter te begrijpen. Op die manier kunnen onzekerheden die geassocieerd worden met voorspellingen van de AMOC worden gereduceerd.

Chapter 1

Introduction

Give it a whirl[1]

Sivert Høyem

1.1. The Atlantic Meridional Overturning Circulation

The exploration of the ocean began when people living in coastal areas wanted to use its resources and to explore the unknown. This takes us back thousands of years, to around 7000 B.C, where evidence shows the extensive seafaring and sailing of great distances carried out by civilizations such as the Polynesians, Greeks and Egyptians. Today, knowing that the ocean controls the Earth's climate, the exploration of the ocean is motivated by the need to understand its dynamics and to predict the impacts of its variability in a changing climate.

One of the most important systems in the ocean is the Atlantic Meridional Overturning Circulation (or AMOC, Johnson et al., 2019). It quantifies the strength of the northward surface transports and southward deeper transports in the Atlantic Ocean. Warm surface waters flow northward along vast distances in the Atlantic (Figure 1.1). This current flow gradually cools on its journey northward releasing heat to the atmosphere. In the subpolar and polar regions the surface waters become dense enough to sink forming cold deep waters, which return southward through the Atlantic Ocean. The northward transport of heat due to the AMOC is responsible for a relatively warm climate in the Northern Hemisphere compared to that of the Southern Hemisphere (Buckley and Marshall, 2016). Moreover, the AMOC is one of the key processes controlling the uptake and distribution of biogeochemical tracers (i.e., CO_2) that are important for the climate system (Fontela et al., 2016).

Because of its role for climate, the AMOC is a focus, in both atmospheric and oceanographic communities, for understanding present and future climate change. The AMOC is frequently schematized as a conveyor belt (Figure 1.1) implying a laminar and coherent ocean transport. However, observing systems that have been deployed throughout the Atlantic Ocean, such as the RAPID array at 26.5 ^{o}N (Smeed et al., 2018), have revolutionized understanding of AMOC variability and have clearly indicated that in reality

---

[1] `https://www.youtube.com/watch?v=4IUR7agj6Mg`

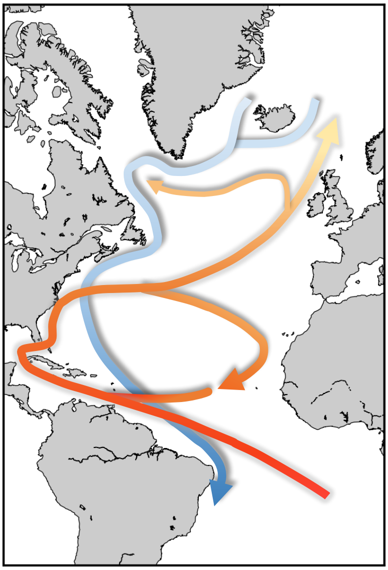

Figure 1.1: Schematic of the Atlantic Meridional Overturning Circulation (AMOC); relatively warm waters (red) flow northwards in the upper layers of the Atlantic Ocean while colder water (blue) returns southwards in deeper layers. Figure is adapted from Marotzke (2012).

an undisturbed representation of the AMOC as seen in Figure 1.1 is not possible. For example, the existence of the mesoscale ocean variability affects the pathways of both the surface and deep currents that constitute the AMOC and thus, is not compatible with a laminar view (Buckley and Marshall, 2016, and references therein). Therefore, to determine the strength, structure, and variability of the AMOC a combination of complex physical processes needs to be considered (McCarthy et al., 2020).

Traditionally, the strength of the AMOC is estimated in depth coordinates to emphasize the vertical transport of water masses. It is commonly defined in depth space as the total northward transport in the upper 1000 m or so of the water column (Wunsch and Heimbach, 2006; Cunningham et al., 2007). Therefore, AMOC in depth space tends to emphasize sinking (i.e., vertical mass flux). An alternative representation of the AMOC is in density space which emphasizes the transformation of lighter to denser water masses (e.g., Xu et al., 2016; Brüggemann and Katsman, 2019). Deep ocean convection is the process that describes how the surface waters become denser and mix vertically with the deeper layers (Marshall and Schott, 1999). There are few regions in the ocean where deep convection occurs. Observations in the marginal seas of the North Atlantic (i.e. the Labrador, the Irminger and the Nordic Seas) reveal convected waters in layers deeper than 1500 m (e.g., Dickson et al., 1996; Lazier et al., 2002; Pickart et al., 2002; Våge et al., 2011a; de Jong et al., 2012; Eldevik et al., 2009). Therefore, to emphasize the transformation of lighter to denser water masses a more appropriate estimate of the AMOC strength at high latitudes is in density coordinates (Zhang, 2010; Xu et al., 2016; Li et al., 2017; Desbruyères et al., 2019; Lozier et al., 2019).

The AMOC strength reported in several studies ranges between 16 to 18 Sv (1 Sv = 10^6 m^3 s^{-1}, Sarafanov et al., 2012; McCarthy et al., 2015). The timeseries between 2004-2012 at the RAPID array (at 26.5 ^{o}N) indicated a decline of the AMOC strength of about 0.54 Sv y^{-1} (Smeed et al., 2014). Although, the updated timeseries up to 2018 display an increasing tendency of the AMOC starting from 2009, this increase has yet low statistical significance (Moat et al., 2020). Furthermore, over the course of the twenty-first century, climate models predict a possible weakening of the AMOC's strength rather than an abrupt transition or shut down (IPCC, 2014). Since the AMOC is a key component of the global climate system, a weakening of its strength could lead to abrupt changes in the Earth's climate (Srokosz et al., 2012). For instance, a weakening AMOC could cause a cooling over the subpolar North Atlantic (e.g., Drijfhout et al., 2012) and in general the northern hemisphere, an increase of the North Atlantic storms and large changes in precipitation in the tropics (Jackson et al., 2015).

Several studies have suggested a strong connection between the AMOC variability and the process of deep convection in the North Atlantic (Eden and Willebrand, 2001; Rahmstorf et al., 2005; Biastoch et al., 2008). However, recent observational studies have cast doubts on the importance of deep water formation in the Labrador Sea for the AMOC. In particular, measurements along an array across the subpolar North Atlantic (placed north of 52^{o}N) within the Overturning in the Subpolar North Atlantic Program (Lozier et al., 2017) indicated that the contribution of the Labrador Sea to the overturning is very small compared to the eastern part of the subpolar North Atlantic (Lozier et al., 2019; Zou et al., 2020). In this view, the observational study of Chafik and Rossby (2019) suggested that the transformation of water masses in the Nordic Seas regulates the AMOC strength rather the one in the Labrador Sea. However, the Labrador Sea remains a key region in the North Atlantic. It is one of the rare locations where dense waters that contribute to the lower limb of the AMOC are formed (e.g., Johnson et al., 2019). In addition, the equatorward transport of dense waters that formed elsewhere in the North Atlantic is mainly achieved through the Labrador Sea (Lozier et al., 2013; Bower et al., 2019). In terms of climate, it is thus important to fully understand the processes that govern the AMOC and its response to projected changes in the formation and spreading of deep water masses.

1.2. The role of the Labrador Sea for the AMOC

The prevailing circulation pattern of the Labrador Sea together with the extreme heat loss that the basin experiences create favorable conditions for the production of dense water masses in the Labrador Sea (Marshall and Schott, 1999). In this section, the general circulation of the Labrador Sea is first introduced, followed by the description of the process of deep convection that occurs in the interior of the basin. Furthermore, the observed variability of the properties of deep convection is discussed in this section. Last, this section provides details on the mechanism behind a resulting overturning cell in a marginal sea subject to strong heat loss, such as the Labrador Sea.

1.2.1. General circulation in the Labrador Sea

The Labrador Sea, located between the west coast of Greenland and the Labrador Peninsula, is a marginal sea of the subpolar North Atlantic. Its circulation can be generally described by a strong boundary current system and a relatively quiescent flow in the interior of the basin (Figure 1.2, Lavender et al., 2000).

East of Greenland the warm, salty Irminger Current (IC) flows alongside the cold, fresh East Greenland Current (EGC). At the southern tip of Greenland the EGC and the IC continue as the West Greenland Current (WGC) flowing on the continental shelf (Gascard and Clarke, 1983; Fratantoni and Pickart, 2007). More accurately, the ECG and IC are thought to continue as the WGC in the Labrador Sea because they have comparable velocities (Pickart et al., 2005), but the differences in their thermohaline properties mentioned above still hold. At the northern edge of the Labrador Sea the WGC separates into a part that continues northward to Davis Strait (Curry et al., 2014) and a part that flows westward and joins the cold, fresh outflow from Davis Strait forming the Labrador Current (LC, Lazier and Wright, 1993).

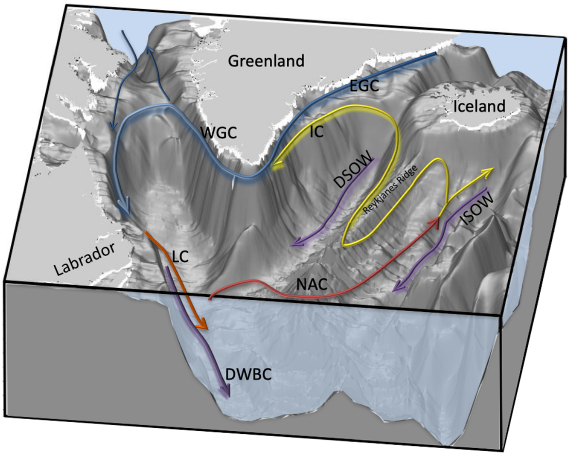

Figure 1.2: Map of the subpolar North Atlantic compiled from ETOPO1 data (Amante and Eakins, 2009). A schematic of the circulation is shown; EGC and WGC: East and West Greenland Currents, respectively. LC: Labrador Current, IC: Irminger Current, NAC: North Atlantic Current, DSOW: Denmark Strait Overflow Water, ISOW: Iceland Scotland Overflow Water and DWBC: Deep Western Boundary Current.

Below the WGC and the LC, the Deep Western Boundary Current (DWBC) transports both dense waters formed in the subpolar North Atlantic and overflow waters from the Nordic Seas. These overflow waters enter the subpolar North Atlantic by crossing either the Denmark Strait (Denmark Strait Overflow Water, DSOW; Jochumsen et al., 2017) or the Faroe-Bank Channel (Iceland Scotland Overflow Water, ISOW; Hansen et al., 2016).

1.2.2. Deep convection

Every winter, cold outbreaks from the Canadian Arctic create very large heat losses over the ice-free waters of the Labrador Sea (Cuny et al., 2005). The prevailing anti-clockwise (cyclonic) circulation pattern in the Labrador Sea (Figure 1.2) has a preconditioning effect on the occurrence of deep convections in the basin. Under these circumstances, isopycnals dome upwards in the interior of the basin, which in turn exposes weakly stratified water from the interior to strong surface heat fluxes, reducing the stratification of the water column through vertical mixing (Marshall and Schott, 1999). These heat fluxes together with the prevailing circulation pattern in the basin foster deep convection events and with them the formation of the Labrador Sea Water (LSW). This water mass contains high concentrations of oxygen and other climatically important trace gases from the ocean surface (Rhein et al., 2017). The ventilation of the LSW is the process that describes the transport of these surface signals into the Labrador Sea interior, which subsequently they spread into the intermediate to deep layers of the Atlantic Ocean. This water mass can be ventilated when the wintertime convection reaches sufficiently deep (Brandt et al., 2007). Furthermore, LSW is very important since is the upper constituent of the lower branch of the AMOC (e.g., Rhein et al., 2017).

A diagnostic that is commonly used to study the properties of deep convection is the mixed layer depth (MLD, Figure 1.3). It is usually defined using a density difference criterion: the depth at which the density is ρ =0.01 kg m^{-3} higher than the surface value (e.g., Courtois et al., 2017). In the winters of 2014 and 2015, an extended phase of strong surface heat loss resulted in MLD in 2015 beyond 2100 m (Figure 1.3 and Yashayaev and Loder, 2017; Piron et al., 2017). Such intensity of convection had not been observed since the beginning of 1990 (Yashayaev and Loder, 2017).

Additionally, Figure 1.3 indicates that the winter MLD in the Labrador Sea is subject to considerable interranual variability since both the depth and the horizontal expansion of the convection region differ from winter to winter. Estimates of maximum MLD in the Labrador Sea for the period 1993-2009 derived from moorings, ship-based measurements and autonomous profiling floats are summarized in the study of Gelderloos et al. (2013). Their literature review illustrated that the deep convection cycle in the Labrador Sea exhibits considerable interannual variability. This variability is regularly correlated with the strength of the wintertime surface heat loss (Pickart et al., 2002). In the case of subsequent cold winters, the restratification of the basin cannot be fully achieved since the strength of the deep convection is larger, allowing the basin to remember previous winters. However, the response of the deep convection to atmospheric forcing is not straightforward. Observations reveal a rapid warming of intermediate layers after deep convection events that cannot be explained from the surface warming alone (Lilly et al., 1999), but also requires a contribution from lateral buoyancy fluxes. In particular, several studies suggested that changes in the boundary currents, and thus in the lateral fluxes, can also regulate the variability of the properties of deep convection on interannual time scales (Straneo et al., 2013; Rykova et al., 2015). Therefore, in terms of climate, it is of fundamental importance to understand the mechanisms responsible for the variability of deep convection in the Labrador Sea.

1.2.3. Overturning in the Labrador Sea

The prevailing circulation of the Labrador Sea is considered to be a vital mechanism for its dynamics (Spall and Pickart, 2001). The boundary current system in a marginal sea subject to intense heat loss (such as the Labrador Sea), becomes more dense in the

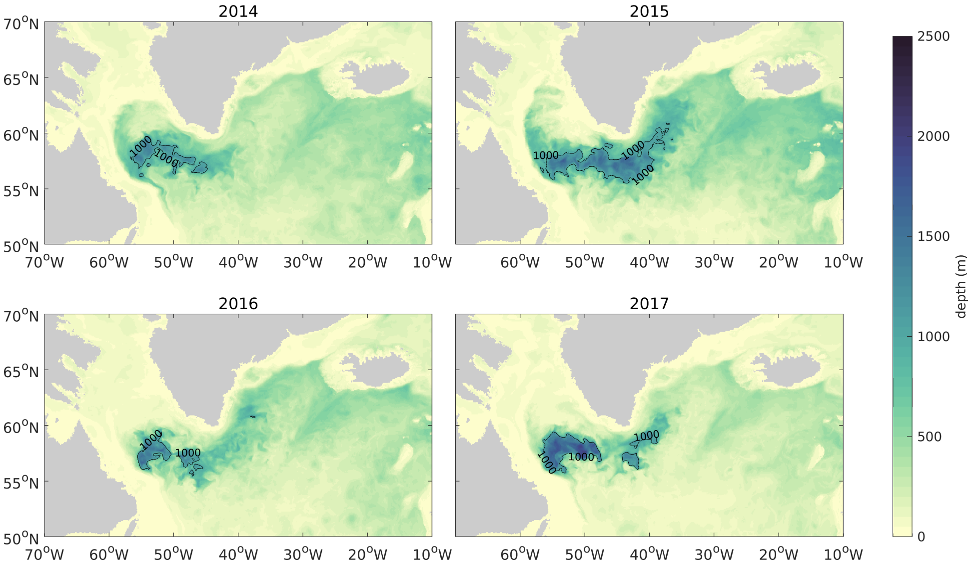

Figure 1.3: Mean March mixed layer depth in the subpolar North Atlantic in (a) 2014, (b) 2015, (c) 2016 and (d) 2017. Black contours denote maximum mixed layer deeper than 1000 m. Data is obtained from the global ocean 1/12^o physics analysis and forecast product from the EU Copernicus Marine Services (https://marine.copernicus.eu).

downstream direction (Spall, 2004; Straneo, 2006a). This densification of the boundary current is achieved by the strong surface heat loss and also by the lateral heat fluxes (Spall and Pickart, 2001; Spall, 2004; Straneo, 2006a; Brüggemann and Katsman, 2019, chapter 2). An important concept of the general circulation in the Labrador Sea relevant to climate is the overturning circulation, which results from this densification of the boundary current.

The overturning reflects the amount of water that exits the basin at a different depth than at which it entered due to the densification of the boundary current (Straneo, 2006a). The theory behind the mechanism of the overturning in a convective marginal sea requires that the boundary current system complies with the thermal wind balance (Spall, 2004). The thermal wind balance, under the geostrophic and hydrostatic balance, is given by equation 1.1 in vector form:

$$f\frac{\partial \vec{u}}{\partial z} = \frac{g}{\rho_o} \times \nabla_h \rho \tag{1.1}$$

where f is the Coriolis parameter, $\vec{u}$ is the horizontal flow component, g is the gravitational acceleration, ∇_h is the horizontal gradient operator (i.e., $\nabla_h \rho = \frac{\partial \rho}{\partial x}\hat{i} + \frac{\partial \rho}{\partial y}\hat{j}$) and ρ is the density.

In a marginal sea that is characterized by a buoyant boundary current and a denser interior, the densification of the boundary current results in a reduction of the horizontal density difference between the boundary current and the interior in its downstream direction. The thermal wind balance yields that the vertical shear of the velocity of the boundary current also reduces, since equation 1.1 simply states that wherever there are horizontal density gradients, the horizontal flow must change with depth. As shown in the idealized studies of Spall and Pickart (2001), Spall (2004) and Straneo (2006a), an immediate consequence of this relation is that the upper part of the boundary current slows down in downstream direction, while the lower part speeds up. This process causes the boundary current to become more barotropic as it encircles the basin (Spall and Pickart, 2001; Straneo, 2006a), reflecting a reduction of transport in the upper part of the boundary current and an increase of transport in its lower part. That is, an overturning occurs somewhere in the basin.

Observational data support the view of an overturning cell in the Labrador Sea. Pickart and Spall (2007) reported an overturning estimate for the Labrador Sea of 2 Sv using a composite of hydrographic sections in the Labrador Sea over the period of 1990-1997. More recently, the continuous measurements along an array across the Labrador Sea (placed north of 52^oN) within the Overturning in the Subpolar North Atlantic Program (OSNAP West, Lozier et al., 2017) provided an overturning estimate in density space of 3.3 Sv from data gathered between August 2014 and April 2016 (Zou et al., 2020). These estimates are in line with the theoretical estimate of the overturning derived in the study of Spall and Pickart (2001).

The recent idealized numerical study of Brüggemann and Katsman (2019) raised questions on how these changes in boundary current transport arise. The two-layer conceptual model of Straneo (2006a) suggests that there is a mass transfer from the upper part of the boundary current towards its lower part. This implies that there is a diapycnal mass flux, thus water mass transformation, within the stratified boundary current itself. However, idealized and realistic model simulations show that strong net downward motions do occur near the boundary (Spall, 2004; Katsman et al., 2018; Sayol et al., 2019). In particular, these studies found that that these downward motions peak well below the mixed layer, where diapycnal processes are known to be small. The highly idealized study of Brüggemann and Katsman (2019) clearly shows that diapycnal downwelling into the densest isopycnal layers only occurs in the interior and indicates that exchanges between the boundary current and the interior play an important role for the local overturning.

1.3. Boundary current-interior interaction

It becomes apparent from the discussion in the previous sections that the interaction between the boundary current and the interior of the Labrador Sea is an essential component of the dynamics of the basin. This section elaborates the importance of this interaction on the key processes that occur in a marginal sea, such as the Labrador Sea that is characterized by a buoyant boundary current and a denser interior and is subjected to strong surface heat loss (Figure 1.4). In particular, this section introduces how this interaction may have an impact on the restratification of the basin after deep convection events due to the heat loss to the atmosphere and also on determining the location where the downwelling occurs in the basin.

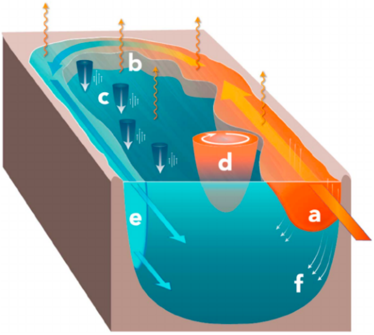

Figure 1.4: A schematic illustrating the key circulation features in a convective marginal sea subjected to surface heat loss (adapted from Johnson et al., 2019): (a) buoyant inflowing boundary current, (b) buoyancy loss to the atmosphere, (c) convective plumes, (d) buoyant eddies shed from the boundary current, (e) denser outflowing boundary current and (f) downwelling along the topography.

1.3.1. Restratification after deep convection

The heat that is lost to the atmosphere during winter in the Labrador Sea needs to be replaced, because otherwise the water column will continue to get colder. However, it is known from long-term measurements that this is not happening and that the warming during summer is not sufficient since the solar radiation cannot reach deeper layers. As mentioned in section 1.2.2, the rapid warming of the interior of the Labrador Sea after deep convection events can be only explained by the combination of the surface warming after the wintertime and lateral heat fluxes (Lilly et al., 1999). These lateral heat fluxes can be achieved by the advection of water masses from the buoyant boundary current system into the interior of the basin (e.g., Prater, 2002; Lilly et al., 2003), driven by the abundant eddy activity observed in the Labrador Sea (Figure 1.5).

There is rich literature (e.g., Prater, 2002; Eden and Böning, 2002; Lilly et al., 2003; Katsman et al., 2004; Bracco et al., 2008; Chanut et al., 2008; Gelderloos et al., 2011; Kawasaki and Hasumi, 2014; Rieck et al., 2019) on the role of the eddy activity in the Labrador Sea for the process of restratification. The eddy field in the Labrador Sea is characterized by vortices ranging from small-scale to mesoscale. A great example of the strong eddy activity that is found in the Labrador Sea can be seen in Figure 1.5. The swirls of color visible in the waters delineate eddies which have diameters ranging from a couple of kilometers to a couple of hundred kilometers.

Three types of eddy have been identified in the Labrador Sea (Gelderloos et al., 2011; Rieck et al., 2019, and references therein): Irminger Rings (IR), convective eddies (CE), and boundary current eddies (BCE). Around the convection region a rim current develops and by the process of baroclinic instability sheds the small-scale CE (Jones and Marshall, 1997). The formation of the BCE is by the process of baroclinic instability distributed around the basin. In particular, BCE's are generated due to the density differences between the fresh and cold WGC encircling the Labrador Sea and the interior. The diameter of both the CE and BCE ranges between 10-30 km.

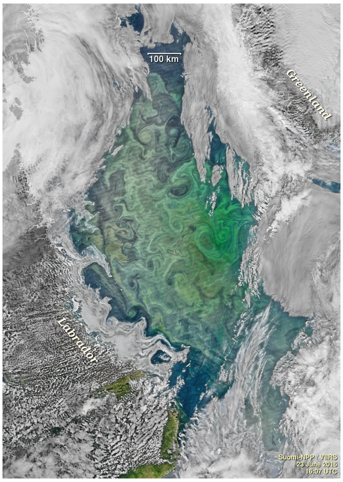

Figure 1.5: Eddy activity in the Labrador Sea as seen in mapped satellite ocean color data. The ocean color is given by the spectral distribution of reflected sunlight and can be used to infer the biological activity that grows in the surface waters. This image was downloaded from `https://oceancolor.gsfc.nasa.gov/` and created by the Visible Infrared Imaging Radiometer Suite (VIIRS) onboard the Suomi National Polar-orbiting Partnership (SNPP) satellite platform on June 23, 2016.

The Irminger Rings (IR) are large eddies with a warm, saline core topped by a colder and relatively fresh near-surface layer (Hátún et al., 2007; de Jong et al., 2014). IRs are shed from the boundary current along the west coast of Greenland where the topography is steep. It is the combination of instability due to the local bathymetry and the baroclinicity of the boundary current that leads to their formation (Eden and Böning, 2002; Katsman et al., 2004; Bracco et al., 2008). These eddies have a diameter of about 60 km and they carry buoyant water from the boundary current. Although IRs are formed away from the Labrador Sea interior, they are able to transport buoyant water to the convected area because they are very energetic (Lilly et al., 2003).

The presence of eddies in the Labrador Sea can restratify the interior of the basin by transporting buoyant water from the boundary current toward the interior (Figure 1.4). The relative importance of the different eddy types for the process of restratification in the Labrador Sea is yet unclear since it depends on their lifespan, vertical extent and how far they can propagate from their formation region towards the interior of the basin. However, it is clear that eddies play a key role in the exchange of heat fluxes between the boundary current and the convective region and thus for the dynamics of the Labrador Sea.

1.3.2. Deep convection versus downwelling

The general idea of the deep convection is that the dense waters are produced in the interior of the marginal seas, where the stratification is weak and the surface waters are exposed to strong heat losses (Marshall and Schott, 1999). Deep convection is characterized by a downward motion within very localized convective plumes which is compensated by upward motion surrounding the plumes (Figure 1.4). Therefore, the net vertical motion over deep convection areas is relatively small (Send and Marshall, 1995).

The study of Spall and Pickart (2001) aimed to have a better understanding of where the waters formed by deep convection sink and what the physical processes are that control this location. They found by using a simple theoretical estimate that a widespread downwelling in a marginal sea at high latitudes would have to be balanced by an unrealistically large horizontal circulation. Instead, they suggested that the downwelling of water can occur in the boundary current system along the perimeter of the marginal seas where the dynamical constraints do not hold (Figure 1.4). This implies that the connection between the convective region and the surrounding circulation must also be taken into account.

A few years later, Spall (2004) and Straneo (2006a), using idealized models, examined the interplay of the convective region with the surrounding circulation in a marginal sea. The aim of these studies was to understand how the dense water is removed from the convection region and how the annual mean heat losses to the atmosphere are compensated. Spall (2004) found that significant downwelling can occur at the topographic boundaries. Straneo (2006a) showed also that downwelling occurs in the boundary current as a result of mass conservation, while remaining in geostrophic balance. Both studies found that a cyclonic boundary current balances the heat loss in the interior by advecting buoyant water towards the interior, where the convection occurs, and draining the dense water out. This heat transfer between the boundary current and the interior is assumed to be mainly driven by eddies that are generated from instabilities of the boundary current.

The fact that there is a strong signal of downwelling motion in a narrow region close to the boundary has been shown in numerous idealized regional model studies (e.g., Pedlosky and Spall, 2005; Spall, 2004, 2010, 2011) and in laboratory experiments (Cenedese, 2012). In addition, most recent global ocean model studies (Katsman et al., 2018; Waldman et al., 2018; Sayol et al., 2019) have also shown that net downwelling occurs in a narrow region near the topographic boundaries. In particular, Katsman et al. (2018) demonstrated that this downward motion in the Labrador Sea is not uniformly spread along the boundaries but has a stronger signal in the areas where the mesoscale eddy activity is enhanced.

Furthermore, Brüggemann and Katsman (2019) building on the existing studies regarding the downwelling in depth space (i.e., mass transport from a shallower to greater depth layer; Spall, 2004, 2010) and in density space (i.e., mass transport from a lighter to denser isopycnal layer; Brandt et al., 2007; Xu et al., 2018) emphasized the important distinction between these two processes. Note that the downwelling in density space is associated with water mass transformation since there is a transport from an isopycnal layer to another and it is also referred as diapycnal downwelling. Brüggemann and Katsman (2019) concluded that while there is a strong near-boundary downwelling signal in depth space, there is no substantial downwelling in density space in this region. On the contrary, they showed that the diapycnal downwelling mainly occurs in the interior of the marginal sea and along the boundary current but at a different location where there is strong downwelling in depth space.

1.4. Research objectives

As outlined in the previous sections, climate models predict that the AMOC will slow over the next centuries. What hinders the complete understanding of the processes that govern the AMOC and its response to projected climate changes, is a better understanding of the various physical processes that compose the North Atlantic circulation. A number of idealized studies (Spall, 2004; Katsman et al., 2004; Straneo, 2006a; Gelderloos et al., 2011; Brüggemann and Katsman, 2019) suggest that the presence of mesoscale eddies is crucial in determining the deep convection, downwelling and the characteristics of the circulation in marginal seas subjected to strong surface heat loss. So far, the climate models that are used to make the AMOC projections and show a significant decline over the 21st century, have a resolution on the order of 1^{o} (~100 km) and hence are not able to appropriately resolve the mesoscale eddies. In the absence of these eddies, climate models may misrepresent the deep convection properties and the surface fluxes, adding an uncertainty on the AMOC projections using those models (Randall et al., 2007). In addition, the quantitative impacts of the eddies on the local downwelling and their interplay with the interior is still an open question. Although idealized eddy-resolving models provide helpful qualitative insights on this interplay, to address this question eddy resolving realistic models are more appropriate.

A question that arises from the previous section is whether the strong downwelling signal in the Labrador Sea is associated with dense water masses that either formed in the boundary current itself in this region or elsewhere in the basin. Although, the idealized study of Brüggemann and Katsman (2019) clearly indicated that the location where these waters are formed differs from the location where the strong downwelling occurs (section 1.3.2), it is yet unclear how these locations are connected. To address this question in detail a better understanding of the pathways that the LSW follows from its formation region to the global ocean is needed. While there are several studies that suggest possible export routes of the LSW (e.g., Talley and McCartney, 1982; Lavender et al., 2000; Straneo et al., 2003; Brandt et al., 2007; Palter et al., 2008; Bower et al., 2009; Rhein et al., 2015; Feucher et al., 2019), the various pathways and the associated timescales are yet to be clarified.

Monitoring the AMOC at a specific latitude as the RAPID array (at 26 ^{o}N, Smeed et al., 2018) has resulted in reliable estimates for its current strength at this latitude. However, at this latitude, it is difficult to investigate the connection between the processes involved in the deep water formation and the AMOC variability. Observations of the AMOC in the subpolar North Atlantic along the OSNAP array (north of 52 ^{o}N, Lozier et al., 2017) aim to improve our understanding on buoyancy-forced AMOC variations. Recent studies based on observations obtained from the OSNAP array suggested a minimal contribution of the Labrador Sea to the AMOC strength (Lozier et al., 2019; Zou et al., 2020). Yet it is unclear what the time frame of these observations should be to accurately make assumptions on possible connections. Furthermore, as discussed in the previous sections, boundary current-interior exchanges in the Labrador Sea might obscure the connection between the deep water formation and AMOC variability in short-term observations such as the OSNAP array.

In this thesis, a combination of numerical modelling techniques and observational data is used to provide new insights on the relationship between the formation, export and associated timescales of deep water masses, and the variability therein. In particular, this thesis aims for a better understanding on the role of the boundary current-interior exchange on the processes that are crucial to determine the AMOC strength and its variability. Hence, this thesis is centered around the following question:

What role does the interaction between the boundary current and the interior of the Labrador Sea play for its dynamics?

1.5. Thesis outline

This section provides an outline of the remaining chapters of this thesis (chapter 2-chapter 6). Each chapter deals with the research question that formulated in the previous section.

Chapter 2 explores the influence of the eddies on deep convection properties in the basin. In addition, chapter 2 identifies the regions where the net downwelling of waters occurs and to advance our understanding of the physics that govern these processes. The analysis performed in chapter 2 is based on a high-resolution idealized numerical model for the Labrador Sea. Idealized regional models have been identified as appropriate tools to represent the processes that occur in the marginal seas in a realistic way (Spall, 2004, 2010, 2011; Katsman et al., 2004; Straneo, 2006a; Gelderloos et al., 2011; Våge et al., 2011b). Moreover, chapter 2 deals with the response of deep convection and downwelling to changes in the surface heat fluxes. Although the main method followed in chapter 2 uses an Eulerian framework, an attempt to track where the newly-formed dense water goes after leaving its formation region is also presented in chapter 2. To do so, a passive tracer is initialized within the area of deep convection and the areas with high concentration of this tracer are identified.

Chapter 2 and also the study of Brüggemann and Katsman (2019) indicate that the convected water is transported from the interior of the basin towards the boundary and in particular the regions where the eddy activity is enhanced. Strongly motivated by this result, a Lagrangian analysis is performed in chapter 3. This analysis investigates the origin and transformation of different water masses found within the boundary current at the exit of the Labrador Sea and assesses the role of the prominent eddy field for exporting these water masses. The Lagrangian analysis followed in chapter 3 is based on analyzing the trajectories of numerical particles that are advected using the output from the idealized model applied in chapter 2. In particular, the idealized model study in a Lagrangian framework that is followed in chapter 3 provides helpful insights on the nature of the interior-boundary current exchange and its role for the LSW export.

The approach and analyses followed in chapter 4, strongly build on the qualitative insights gained in chapter 3. Chapter 4 delves deeper into the possible export pathways of the water masses exiting the Labrador Sea using both observational data and the output of a realistic global ocean model. The trajectories of available Argo floats that drift within the Labrador Sea are analyzed to identify pathways and associated timescales of deeper water masses within the Labrador Sea from an observational point of view. The use of output from a realistic simulation introduces among others more realistic atmospheric forcing and bathymetry, the effects of salinity, potential connections between the subbasins of the subpolar North Atlantic and the presence of overflow waters. These aspects were not included in the idealized model used in chapter 2 and chapter 3. Thus, the methodology followed in this chapter allows a more realistic and quantitative characterization of the transports and water mass transformation along different pathways.

Chapter 5 contains a sensitivity study of the pathways that water masses follow prior to exiting the Labrador Sea with respect to variations in the surface heat loss. The response of the deep convection to changes in the surface heat fluxes that has been analyzed in chapter 2 already suggested a rather complicated connection between dense water formation, eddies and surface forcing. Chapter 5 investigates how the export of the convected water and the associated timescales are affected by the changes in the surface heat flux. The methodology followed in this chapter combines the output of the idealized sensitivity simulations performed in chapter 2 with a Lagrangian tracking tool. Knowledge on the response of the pathways of the convected water in a changing climate is important to direct further observational and modelling efforts.

Chapter 6 presents the conclusions of this thesis, reflecting about the role of the boundary current-interior exchange on the dynamics of the Labrador Sea along with potential directions for future research.

Chapter 2

On the interplay between downwelling, deep convection and mesoscale eddies in the Labrador Sea

In this study, an idealized eddy-resolving model is employed to examine the interplay between the downwelling, ocean convection and mesoscale eddies in the Labrador Sea and the spreading of dense water masses. The model output demonstrates a good agreement with observations with regard to the eddy field and convection characteristics. It also displays a basin mean net downwelling of 3.0 Sv. Our analysis confirms that the downwelling occurs near the west Greenland coast and that the eddies spawned from the boundary current play a major role in controlling the dynamics of the downwelling. The magnitude of the downwelling is positively correlated to the magnitude of the applied surface heat loss. However, we argue that this connection is indirect: the heat fluxes affect the convection properties as well as the eddy field, while the latter governs the Eulerian downwelling. With a passive tracer analysis we show that dense water is transported from the interior towards the boundary, predominantly towards the Labrador coast in shallow layers and towards the Greenland coast in deeper layers. The latter transport is steered by the presence of the eddy field. The outcome that the characteristics of the downwelling in a marginal sea like the Labrador Sea depend crucially on the properties of the eddy field emphasizes that it is essential to resolve the eddies to properly represent the downwelling and overturning in the North Atlantic Ocean, and its response to changing environmental conditions.

This chapter has been published in *Ocean Modelling* **135**. (2019) 56-70.

2.1. Introduction

The Atlantic Meridional Overturning Circulation (AMOC) quantifies the zonally integrated meridional volume transport of water masses in the Atlantic Ocean. A prominent feature of the AMOC is an overturning cell where roughly 18 Sv (1 Sv = 10^6 m^3 s^{-1}, Cunningham et al. 2007; Kanzow et al. 2007; Johns et al. 2011) of water flows northward above 1000 m, accompanied by a southward return flow at depth. As the surface waters flow northward through the Atlantic Ocean, they become dense enough to sink before they return southward at depth.

This lower limb of the AMOC contains water masses that can be traced back to specific deep ocean convection sites (Marshall and Schott, 1999). There are few regions in the world oceans where deep convection occurs, and numerous studies have revealed that the most important ones are in the marginal seas of the North Atlantic (Dickson et al., 1996; Lazier et al., 2002; Pickart et al., 2002; Eldevik et al., 2009; Våge et al., 2011a; de Jong et al., 2012; de Jong and de Steur, 2016b; de Jong et al., 2018).

Through the process of deep convection, dense waters are produced in the interior of the marginal seas, where the stratification is weak and the surface waters are exposed to strong heat losses (Marshall and Schott, 1999). While convection involves strong vertical transports of heat and salt, the interior of these marginal seas is known for a negligible amount of net downwelling. In particular, by applying the thermodynamic balance and vorticity balance to an idealized setting, Spall and Pickart (2001) pointed out that in a geostrophic regime, widespread downwelling in the interior of a marginal sea at high latitudes is unlikely, as it would have to be balanced by an unrealistically strong horizontal circulation. Instead, substantial downwelling of waters may occur along the perimeter of the marginal seas where the geostrophic dynamical constraints do not hold.

Using an idealized model, Spall (2004) demonstrated that significant downwelling indeed only occurs at the topographic slopes of a marginal sea subject to buoyancy loss. This downward motion yields an ageostrophic vorticity balance in which the vertical stretching term and lateral diffusion term near the boundary dominate (Spall, 2010). Straneo (2006a) considered the downwelling near the boundary from a different perspective, by developing an analytical two-layer model. In this study, a convective basin is represented by two regions; the interior, where dense water formation occurs due to surface buoyancy loss, and a buoyant boundary current that flows around the perimeter of the marginal sea. It is assumed that instabilities provide the lateral advection of buoyancy from the cyclonic boundary current towards the interior required to balance the atmospheric buoyancy loss over the interior. This alongstream buoyancy loss of the boundary current reduces the density difference between the boundary current and the interior along the perimeter of the marginal sea. As a consequence, the thermal wind shear of the boundary current decreases in downstream direction, and continuity then demands the water to downwell at the coast (see also Katsman et al. (2018) and references therein).

Spall and Pickart (2001) argue that the magnitude of the buoyancy loss of the boundary current determines the amount of downwelling that occurs near the boundary. While the surface buoyancy loss contributes to this buoyancy loss, it is assumed to be mainly driven by eddies generated by instabilities of the boundary current (Spall, 2004; Straneo, 2006a).

Eddies shed from the boundary current also play an important role for the cycle of ocean convection and restratification. Deep convection occurs during wintertime in the southwest Labrador Sea (Clarke and Gascard, 1983; Lavender et al., 2000; Pickart et al., 2002; Våge et al., 2008). The dense water that is formed during the convection events, Labrador Sea Water (LSW), strongly contributes to the structure of the North Atlantic Deep Water, which in turn is a crucial component of the AMOC (Lazier et al., 2002; Yashayaev et al., 2007; Pickart and Spall, 2007; Lozier, 2012). Several studies show that the thermohaline characteristics of LSW are influenced not only by external parameters like the surface heat fluxes, but also by the baroclinic structure of the boundary current that enters the Labrador Sea (Spall, 2004; Straneo, 2006b), known as the West Greenland Current (WGC), and its interannual variability (Rykova et al., 2015).

In the Labrador Sea heat is carried from the WGC into the interior by Irminger Rings (IRs): large mesoscale eddies that are formed off the west coast of Greenland in a region characterized by a steep topographic slope (Lilly et al., 2003; Katsman et al., 2004; Bracco et al., 2008; Gelderloos et al., 2011). It has been recognised that the IRs strongly contribute to compensating the annual mean heat loss to the atmosphere that occurs in the Labrador Sea (Katsman et al., 2004; Hátún et al., 2007; Kawasaki and Hasumi, 2014).

From the above, it is clear that eddies are of immense significance for the downwelling as well as for the convection and the heat budget in the Labrador Sea. The dynamics of the downwelling and how it is related to the observed export of dense water masses is a topic of ongoing research, as the quantitative effects of the interplay between downwelling, eddies and convection are far from clear. For example, in a basin subject to buoyancy loss, one expects that an increase of the heat loss will result in denser and most likely deeper mixed layers. At first glance, this will increase the horizontal density gradients within the basin, strengthen the baroclinic instability of the boundary current and hence intensify the eddy field and the strength of the downwelling. This suggests a positive feedback of the increased eddy fluxes on the downwelling. However, the enhanced efficiency of eddies to restratify the interior after convection may provide a negative feedback on the convection and it is not clear a priori what the net effect will be.

Moreover, observations show that convected waters that originate from the Labrador Sea contribute to the lower limb of the AMOC (Rhein et al., 2002; Bower et al., 2009). This suggests that there has to be a connection between the convective regions (where these dense waters are formed) and the surrounding circulation near the boundary (where waters can sink) that has not been fully explored. Eddies provide a possible natural connection between these two regions.

The aim of this chapter is to assess the quantitative impacts of the eddy field on the downwelling in the Labrador Sea and its interaction with deep convection. We seek to gain more insight in the dynamics that control the downwelling in a convective marginal sea and its response to changing forcing conditions. Towards this goal, we use a highly idealized configuration of a high-resolution regional model in order to isolate specific processes and connect the outcomes with theory. In particular, we diagnose how the eddy field influences the downwelling by exchanging heat between a warm boundary current and a cold interior basin subject to convection. We compare our results to previous theories of downwelling dynamics. In addition, we use a passive tracer study to shed light into the pathways of the dense water masses and especially focus on the role of the eddies in determining these pathways. Finally, by using two sensitivity studies reflecting a milder and colder winter climate state, we test the sensitivity of the downwelling and the export of dense waters with regard to varying surface forcing.

The chapter is organized as follows: the model setup and the simulations performed are described in section 2.2. The representation of deep convection and the characteristics of the downwelling are described in section 2.3. The response of the deep convection and the time mean downwelling to changes in the surface forcing is presented in section 2.4, followed by a discussion in section 2.5. The conclusions of this work are presented in section 2.6.

2.2. Model setup

2.2.1. Model domain and parameters

The numerical simulations performed in this study are carried out using the MIT general circulation model (Marshall et al., 1997) in an idealized configuration for the Labrador Sea. MITgcm solves the hydrostatic primitive equations of motion on a fixed Cartesian, staggered C-grid in the horizontal. The configuration of the model is an improved version of the one used in the idealized studies of Katsman et al. (2004) and Gelderloos et al. (2011), which now incorporates seasonal variations of both the surface forcing and the boundary current and enhanced vertical resolution.

The model domain is 1575 km in the meridional direction and 1215 km in the zonal direction. It has a horizontal resolution of 3.75 km in x and y direction (Figure 2.1a), which is below the internal Rossby radius of deformation for the first baroclinic mode in the Labrador Sea (~7.5 km, Gascard and Clarke 1983). The model has 40 levels in the vertical with a resolution of 20 m in the upper layers up to 200 m near the bottom. The maximum depth is 3000 m and a continental slope is present along the northern and western boundaries (Figure 2.1a). Following Katsman et al. (2004) and Gelderloos et al. (2011), we apply a narrowing of the topography to mimic the observed steepening of the slope along the west coast of Greenland, which is crucial for the shedding of the IRs from the boundary current (Figure 2.1a, Bracco et al. 2008). The continental shelves are not included. There are two open boundaries (each roughly 100 km wide), one in the east and one in the southwest, where the prescribed boundary current enters and exits the domain. All the other boundaries are closed (Figure 2.1a).

Subgrid-scale mixing is parameterized using Laplacian viscosity and diffusivity in the vertical direction and biharmonic viscosity and diffusivity in the horizontal direction. The horizontal and vertical eddy viscosity are $A_h = 0.25 \times 10^9$ m^4 s^{-1} and $A_v = 1.0 \times 10^{-5}$ m^2 s^{-1} respectively, while the horizontal diffusion coefficient is $K_h = 0.125 \times 10^9$ m^4 s^{-1}. The vertical diffusion coefficient is described by a horizontally constant profile which decays exponentially with depth as $K_v(z) = K_b + K_0 \times e^{(-z/z_b)}$, where $K_b = 10^{-5}$ m^2 s^{-1}, $K_0 = 10^{-3}$m^2 s^{-1} and $z_b = 100$ m. Temperature is advected with a quasi-second order Adams-Bashforth scheme. In case of statically unstable conditions, convection is parameterized through enhanced vertical diffusivity ($K_v = 10$ m^2 s^{-1}). A linear bottom drag with coefficient 2×10^{-4} m s^{-1} is applied.

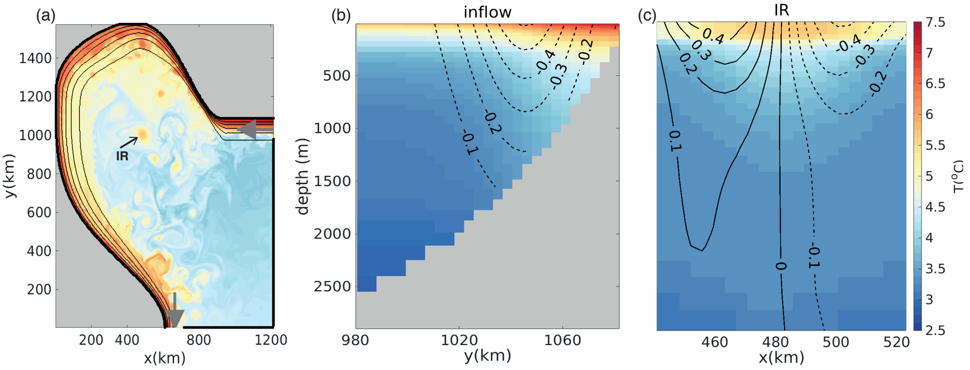

Figure 2.1: (a) Snapshot of the sea surface temperature (SST) for the reference simulation (referred to in the text as REF). Black contours outline the bathymetry, the contour interval is 500 m starting from the isobath of 500 m. The grey arrows represent the inflow/outflow, where the boundaries are open (x_{inflow} =1215 km, y_{inflow}= 978.75-1083.75 km and $x_{outflow}$= 611.25-708.75 km, $y_{outflow}$ = 3.75 km) (b) Section across the inflow region (at x = 1215 km) showing the annual mean temperature (T_{in}, in °C) and meridional velocity (U_{in}, in m s^{-1}, black contours). (c) Zonal section of an example Irminger Ring in the REF simulation by means of temperature (shading, in °C) and meridional velocity (black contours, in m s^{-1}). This Irminger Ring is visible in the SST snapshot in the basin interior (x=443-525 km and y=1012.5 km) in (a).

Following Katsman et al. (2004), the model is initialized with a spatially uniform stratification, $\rho_{ref}(z)$, representative of the stratification in the western Labrador Sea in late summer along the WOCE AR7W section. Only temperature variations are considered in the model, so this stratification is represented by a vertical gradient in temperature, $T_{ref}(z)$, calculated from $\rho_{ref}(z)$ using a linear equation of state: $\rho_{ref}(z) = \rho_0$ $[1 - \alpha\,(T - T_{ref}(z))]$, where $\rho_0 = 1028\,\mathrm{kg\,m^{-3}}$ and α the thermal expansion coefficient ($\alpha = 1.7 \times 10^{-4}\,°C^{-1}$).

The effects of salinity are not incorporated in the model. In reality, salinity does affect the properties of deep convection in the Labrador Sea, as the IRs shed from the boundary current carry cold, fresh shelf waters at their core (e.g., Lilly and Rhines, 2002; de Jong et al., 2016). As shown in for example Straneo (2006b) and Gelderloos et al. (2012), the contribution of this lateral fresh water flux to the buoyancy of the Labrador Sea interior impacts the convection depth, and large salinity anomalies may in fact be partly responsible for observed episodes when deep convection shut down (Belkin et al., 1998; Dickson et al., 1988). However, since we focus here on the underlying dynamics that control the downwelling and its response to changing forcing conditions, the effects of salinity are omitted in the model for simplicity.

2.2.2. Model forcing

At the eastern open boundary, an inflow representing the WGC is specified by a meridional temperature field $T_{in}(y,z)$ and a westward flow $U_{in}(y,z)$ in geostrophic balance with this prescribed temperature (Katsman et al., 2004). Although the WGC consist of cold, fresh Arctic-origin waters and warm, salty waters from the Irminger Current (Fratantoni and Pickart, 2007) we only incorporate in the model density variations associated with the latter part. The cool, fresh surface waters are omitted, since they are found on the continental shelf, which is not included in our idealized bathymetry (Figure 2.1a). The time-mean structure of this warm boundary current is shown in Figure 2.1b. The boundary current follows the topography and flows cyclonically around the basin. The seasonal variability of the WGC seen in observations (Kulan and Myers, 2009; Rykova et al., 2015) is represented in the model by adding a sinusoidal seasonally varying term to the inflow conditions based on these observations ($\Delta U_{max} = 0.4$ cm s^{-1} that peaks in September and attains its minimum in March). At the southern open boundary an Orlanski radiation condition (Orlanski, 1976) for momentum and tracers is applied.

At the surface, only a temporally and spatially varying surface heat flux is applied, which is an idealized version of the climatology of WHOI OAFlux project (Yu et al., 2008). The strongest heat loss occurs on the northwestern side of the basin (Figure 2.2), and its amplitude decays linearly away from this heat loss maximum (white marker in Figure 2.2b). The net annual heat loss over the entire model domain of the reference simulation (hereinafter REF) is -18 W m^{-2}. The time dependence of the amplitude of the surface heat fluxes (Figure 2.2c) is also based on the observations, ranging from -320 W m^{-2} (January) to 140 W m^{-2} (July) at the location of the heat loss maximum.

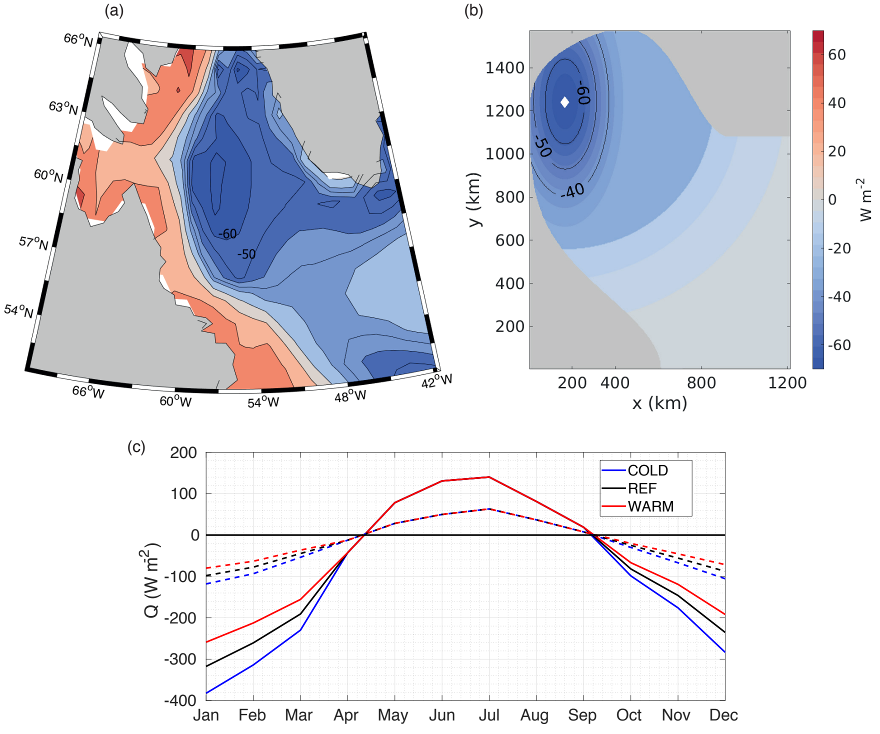

Figure 2.2: (a) 1983-2009 mean of heat flux from the climatology of WHOI OAFlux project (Yu et al., 2008). (b) Annual mean surface heat flux applied to the model. Q< 0 means cooling of the sea surface, Q in W m^{-2}. (c) Seasonal cycle of the amplitude of the heat flux at the location where the amplitude is maximum (white marker in b, solid lines) and the mean over the basin (dashed lines) for the three different simulations (black: REF, red: WARM and blue: COLD).

One of the main objectives of this study is to investigate how changes in the surface heat fluxes influence the evolution of convection, eddy activity and the magnitude of the downwelling. For this reason, we perform sensitivity studies, in which we change the atmospheric cooling in wintertime by 50% with respect to the reference simulation (Figure 2.2c). The net annual heat loss over the entire model domain for these simulations with a colder and warmer wintertime regime (hereinafter COLD and WARM) is -25 and -12 W m^{-2} respectively or a 33% increase (28% decrease) in heat loss with respect to REF. In agreement with Gelderloos et al. (2012) and Moore et al. (2012), the mean winter heat loss (December-February, at the location of the heat loss maximum) is between -170 to -250 W m^{-2} in these simulations.

2.2.3. Model simulations

All the simulations are performed for a period of 20 years in which each model year is defined as 12 months with 30 days each for simplicity. The 2-day snapshots and the monthly means of all diagnostics are stored. For our analysis, we use the snapshots from the last five years of the simulations phase (i.e. model years 16 to 20).

Earlier studies have identified three types of eddies that may play a role for the dynamics of the Labrador Sea (Chanut et al., 2008; Gelderloos et al., 2011): the large Irminger Rings (IR) shed near the west coast of Greenland, convective eddies (CE) and boundary current eddies (BCE) that arise on fronts surrounding the convection region in winter and on the front between the boundary current and the interior, respectively. The latter two typically have a scale on the order of the Rossby deformation radius, and are much smaller than the IRs. At a resolution of 3.75 km we barely resolve these mesoscale CE and BCE. However, the IR are well represented in our model simulations.

A snapshot of the sea surface temperature for REF (Figure 2.1a) illustrates that in the idealized model, warm core IRs are formed at the west coast of Greenland, where the slope is steep. A cross section of a representative IR is shown in Figure 2.1c. The maximum velocity in the IR ranges between 0.5 and 0.8 m s^{-1} and the radius is approximately 30 km. This is in line with the observational studies of Lilly et al. (2003) and de Jong et al. (2014) who find maximum velocities between 0.3 to 0.8 m s^{-1} and diameters of 30-60 km. The temperature anomaly at the core of the modelled IR (representative of its buoyancy anomaly; recall that salinity effects are omitted) reaches at 1500 m. Moreover, the average temperature between 200 and 1000 m is 4.25 ^{o}C, which is in good agreement with the observed vertical structure of IRs as characterized by de Jong et al. (2014).

Figure 2.3a shows the timeseries of the basin-mean temperature for the simulations. The impact of the seasonal cycle of the applied surface heat flux is evident. For all the simulations, after ~ 10-15 years of integration the basin-mean temperature reaches a quasi-equilibrium. In this model, such an equilibrium can only be reached if the lateral advection of heat efficiently balances the heat that is lost to the atmosphere. A heat budget analysis indicates that this idealized model can reproduce the balance between the lateral heat advection and the surface heat flux (Figure 2.3b and 2.3c), as proposed by Straneo (2006a) and Spall (2012). Although the mean heat advection and the eddy heat advection mostly cancel each other (Figure 2.3d and Figure 2.3e), the eddy heat advection dominates in the interior while the heat advection by the mean flow dominates within the boundary current. The eddy heat advection clearly shows the expected transport from the boundary to the interior (Figure 2.3d). The negative contribution of the mean heat advection in the northern part of the domain may seem puzzling at first. However, similar negative contributions are seen in the model studies by Saenko et al. (2014) and de Jong et al. (2016). We assume that this is a consequence of the fact that most eddies are anticyclones, and that they tend to follow a preferred path from east to west. As a result, the mean heat advection term contains a mean contribution of this “train of buoyant eddies”. Once the eddies have detached from the boundary current, they move westward and cool along their path, which corresponds to a negative contribution to the mean heat advection. As a consequence, the eddies are responsible for an interior warming and the mean flow is responsible for a warming along the boundary. Both are necessary to balance the heat loss that occurs over the interior as well as over the boundary current. In addition, a cross section of the eddy heat advection over the interior confirms that the eddies transport a significant amount of heat into the interior at depths down to 500m (Figure 2.3f).

From the above and earlier studies with a similar version of the model (Gelderloos et al., 2011) it is evident that with this set of parameters the model is able to resolve the main characteristics of the eddy field, and to capture the properties of the mesoscale eddies (in particular the IRs). Although with the horizontal resolution of 3.75 km the submesoscale eddies are not fully resolved in our model, we consider it appropriate for this study since we focus on the dynamics of the downwelling in the presence of mesoscale eddies.

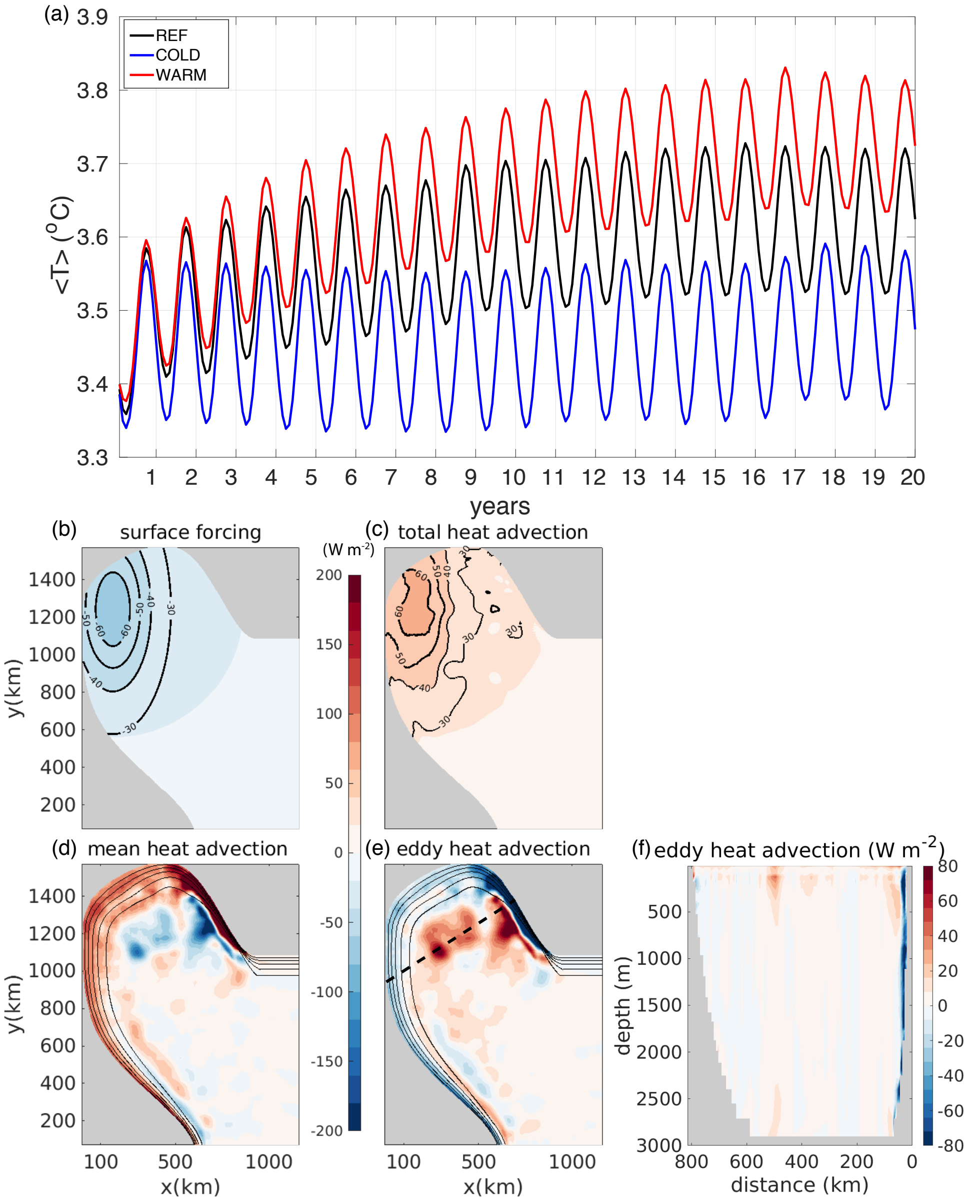

Figure 2.3: (a) Timeseries of the basin-mean temperature of all simulations. (b-e) Depth-integrated terms of heat budget (in W m^{-2}) for the REF simulation (average over years 16-20): (b) surface heat flux (Q), (c) total heat advection (sum of mean and eddy component), (d) mean heat advection, $\nabla \cdot (\overline{\mathbf{U}}\,\overline{\mathrm{T}})$, and (e) eddy heat advection, $\nabla \cdot (\overline{\mathbf{U}'\mathrm{T}'})$. Overbars denote the five year means, primes the anomalies with this respect to this mean and $\mathbf{U} = (u, v, w)$ is the velocity vector. In (d) and (e) the black contours outline the bathymetry, the contour interval is 500 m starting from the 500 m isobath. (f) Eddy heat advection (in W m^{-2}) over the section indicated by the black dashed line in (e).

2.3. Deep convection and downwelling in the basin

First, we examine the location and the size of the deep convection area and its connection to the properties of the eddy field for the reference simulation. We also investigate the characteristics of the downwelling, which is expected to peak in regions of high eddy activity, as discussed in section 2.1.

2.3.1. Properties of the mixed layer depth and eddy field

We calculate the mixed layer depth (MLD), following Katsman et al. (2004), as the depth at which the temperature is 0.025 °C lower than the surface temperature (equivalent to a change in density of 5×10^{-3} kg m^{-3}). The black contours in Figure 2.4a show the winter (February-March, FM) mean patterns of the mixed layer depth (MLD) averaged over the last 5 years of the reference simulation (REF). The deepest convection is found in the southwestern part of the Labrador Sea, reaching depths of 1700 m. Note that the deepest mixed layers are not located where the maximum heat loss is applied (blue contours in Figure 2.4a). A mean hydrographic section across the domain in late spring (May, Figure 2.4b) shows that in this idealized model the convected water is found between the isopycnals of $\sigma = \rho - 1000 = 28.32 - 28.40$ kg m^{-3}. In addition, the surface layer is getting warmer at this time suggesting the beginning of the restratification phase as seen in observations (Lilly et al., 1999; Pickart and Spall, 2007). Overall, in REF the location and the depth of the convection area agree well with observations (Lavender et al., 2000; Pickart et al., 2002; Våge et al., 2009; Yashayaev and Loder, 2009) and complex high-resolution model simulations (Böning et al., 2016), certainly considering the idealizations applied in the model.

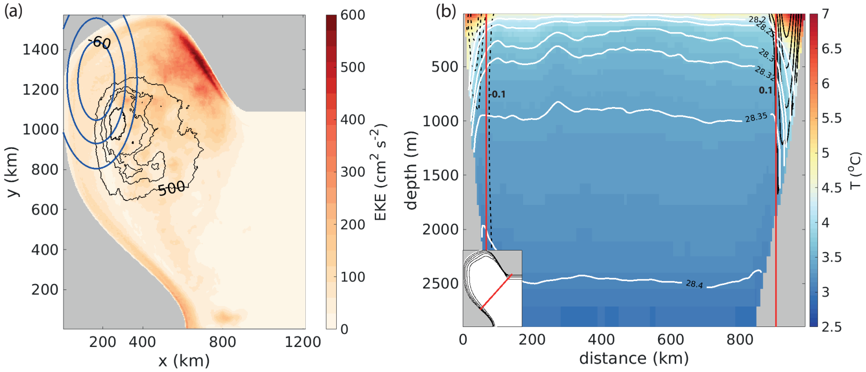

Figure 2.4: (a) Mean eddy kinetic energy (EKE in cm^2 s^{-2}, shading) superimposed on the contours of the winter mixed layer depth (MLD in m, contour interval is 500 m) for REF. Blue contours denote the annual mean surface heat fluxes in W m^{-2} that have been applied to the simulation (contour interval is 10 W m^{-2}). (b) Late spring (May) mean temperature (shading, in °C) and density $\sigma = \rho - 1000$ (in kg m^{-3}; contour interval is 0.05 kg m^{-3}) over a section indicated by the red line in the inset figure, for REF. The section is plotted against distance from the west coast (km). Positive (negative) velocity contours are shown in black solid (dashed) lines (contour interval is 0.1 cm s^{-1}). The vertical red line indicates the limits of the boundary current based on the barotropic streamfunction. Values are averaged over years 16-20.

In REF, IRs propagate from their formation site near the coast towards the interior, as is shown in Figure 2.5a by means of the relative vorticity at the surface. Their signal is weaker but still evident in deeper layers (Figure 2.5b-d). This is in agreement with the example cross-section of an IR (Figure 2.1c), which displays a vertical extent of 1000-1500 m. The IRs carry buoyant water from the boundary current into the interior Labrador Sea and they effectively limit the extent of convection. To illustrate the extent of the impact of the IRs, we use the surface eddy kinetic energy, defined as $\mathrm{EKE} = \frac{1}{2}\,(\overline{u'^{\,2} + v'^{\,2}})$, where the overbar indicates the time averaged values of the five years considered and the primes are the deviations from the 5-year mean fields (shading in Figure 2.4a). The EKE has a maximum of 625 $\mathrm{cm}^2\,\mathrm{s}^{-2}$ near the West Greenland continental slope and fades away offshore in a tongue-like shape. Its magnitude and pattern are in quantitative agreement with studies that derive EKE from altimetry (Prater, 2002; Lilly et al., 2003; Brandt et al., 2004; Zhang and Yan, 2018). Enhanced EKE is also observed along the Labrador coast with maximum values of 200 $\mathrm{cm}^2\,\mathrm{s}^{-2}$, which is also associated with local instability of the boundary current (Brandt et al., 2004).

It is noteworthy that this highly idealized configuration is able to produce a realistic surface EKE and mixed layer, with regard to depth, location and extent (Figure 2.4a). These mixed layer properties are not prescribed, in contrast to the study by Gelderloos et al. (2011), in which a convective patch was artificially created in the domain in a similar configuration of the model. Together with Figure 2.3, this indicates that the current model setup captures the physical processes that are essential to the cycle of convection and restratification in the Labrador Sea, and hence is suited for this type of process study.

2.3.2. Vertical velocities and downwelling

To analyze the downwelling in the basin, we first calculate the time-mean vertical velocity integrated over the total domain and within four areas (Figure 2.6a). Each of these areas is characterized by different dynamics: area 1 is the region where the IRs are formed, area 2 is the region where the strongest heat loss is applied, area 3 is the region in the southwest part of the domain where the second EKE maximum is found (Figure 2.4a) and area 4 defines the interior, where the bottom is flat. In particular, the distinction between the interior and the boundary current areas is based on a cutoff value for depth (i.e. 2900m). The western edge of area 1 is defined to be well downstream of the EKE maximum.

It appears that in this idealized model an overturning is present. The net vertical transport over the total domain is downward (black line in Figure 2.6b). It amounts to 3.0 Sv and peaks at a depth of 1000 m.

The horizontal distribution of the time-mean vertical velocities at this depth of maximum downward transport (i.e. 1000 m) in REF (Figure 2.6c) shows two regions of strong vertical velocities along the lateral boundaries: one close to the steepening of the slope at the northeastern part of the domain and one close to the Labrador coast. This finding that high values of vertical velocity occur in a narrow area close to the lateral boundaries, in particular in areas characterized by elevated surface EKE (Figure 2.4a), is in line with results from several idealized model studies (Spall and Pickart, 2001; Spall, 2004, 2010; Pedlosky and Spall, 2005) and global model studies (Luo et al., 2014; Katsman

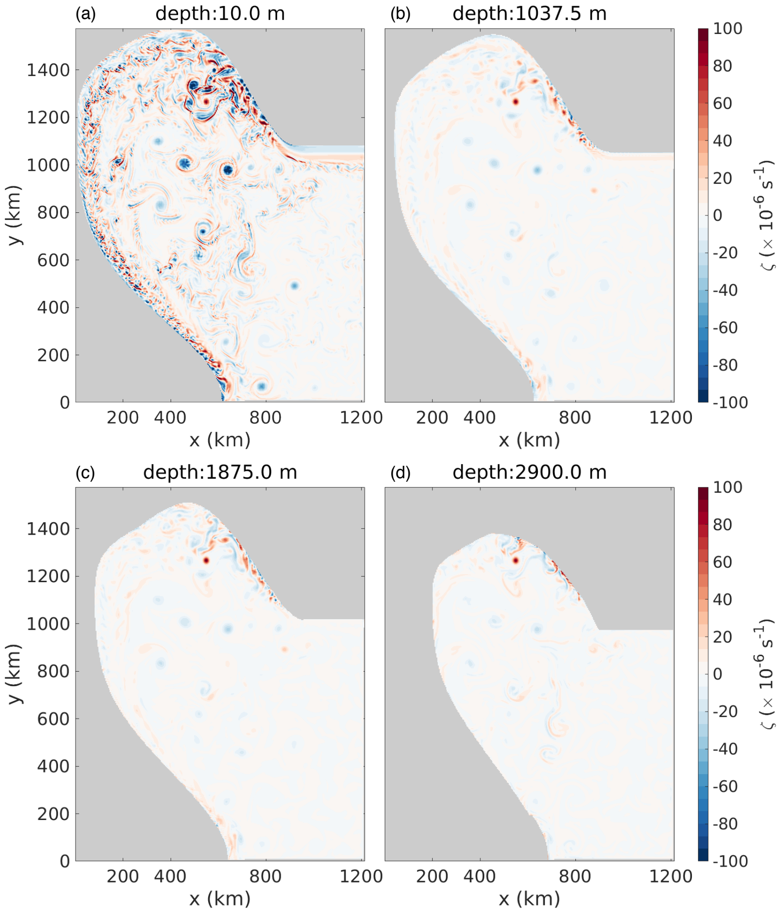

Figure 2.5: Snapshot of the relative vorticity ($\zeta = \frac{\partial v}{\partial x} - \frac{\partial u}{\partial y}$, in 10^{-6} s^{-1}) for REF at the beginning of year 18 of the simulation at a depth of (a) 10.0 m, (b) 1037.5 m, (c) 1875.0 m and (d) 2900.0 m.

et al., 2018; Sayol et al., 2019). The outcome that the west coast of Greenland (area 1) and the Labrador coast (area 3) are identified as regions of enhanced downwelling again highlights the importance of the eddies for the dynamics of the Labrador Sea (see Figure 2.4a).

Figure 2.6b, which shows the vertical transport as a function of depth integrated over the full domain and the four areas, confirms that indeed the net downward transport seen in the model takes place in areas 1 and 3. The downwelling peaks in area 1 at a depth of 1000 m (green line in Figure 2.6b) and amounts to 3.4 Sv, while in area 3 it amounts to 1.0 Sv at a depth of 1525 m. The areas 2 and 4 are characterized by a small net upwelling despite the fact that these two areas are subjected to the strongest surface heat loss. Focusing on the formation area of the IRs, we next analyze the vertical velocity over a cross section in area 1 (Figure 2.6d). It is evident from this figure that the mean vertical transports in the interior are very low (at a distance greater than 60 km from the coast). Similarly to Spall (2004), the downwelling is concentrated close to the boundary, while there is an upwelling region farther offshore. This cell-like structure is what is expected from boundary layer dynamics (Pedlosky and Spall, 2005). Overall, as shown in Figure 2.6b, the net transport in this area is downward.

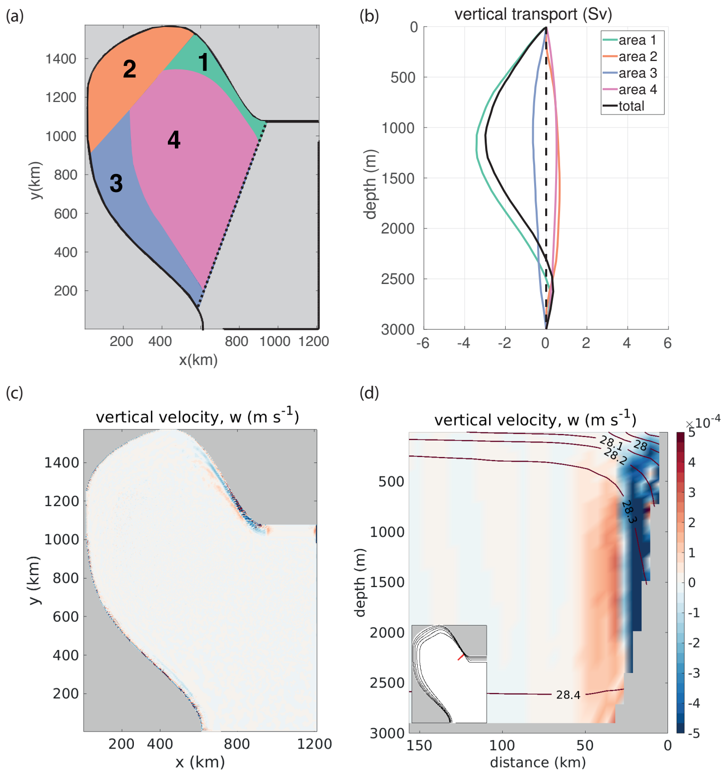

Figure 2.6: (a) Definition of four areas (see text for detailed description). The total area of our interest is defined by the dashed line. (b) Vertical transport in depth space over the total domain and for the four areas (color-coded according to the map in (a)) for the REF simulation. (c-d) Vertical velocity at (c) 1000 m depth and (d) over a section across the boundary current near Greenland, indicated by the red line in the inset figure. The section is plotted against distance from the coast (km). Values are averaged over years 16-20.

2.3.3. Spreading of dense waters

A counterintuitive aspect that stands out from this analysis is the fact that the strongest downward motions occur at the lateral boundaries: a region associated with relatively buoyant waters rather than dense waters, while at the same time it is clear from observations that dense, convected waters contribute to the overturning circulation (Rhein et al., 2002; Bower et al., 2009).

To investigate the spreading of the dense waters, we released a passive tracer at the core of the convection area. The tracer is initialized with a value of 1 in a cylinder of a radius 190 km and from the surface to a depth of 1575 m (inset in Figure 2.7a) at the beginning of year 16. The maximum depth for the initialization of the tracer corresponds well to the depth of the winter (February-March) mixed layer of the modelled year 16. It is monitored for a period of five years. After one year, the tracer is found in deeper layers in the section across the domain (Figure 2.7a). During winter, the tracer is brought to deeper layers by convection, but by the end of the year its concentration is still bounded by the isopycnals of the convected water (i.e. $\sigma = 28.32 - 28.40$ kg m^{-3}, Figure 2.4b). The tracer is directly advected into the boundary current at the western side of the basin (Figure 2.7b-f), similarly to the export route suggested by Brandt et al. (2007). However, this export route mainly occurs at shallower depths (z < 1575m), while in deeper layers the tracer also moves towards areas 1 and 2 (Figure 2.7d-h). (More details on the evolution of the concentration of the passive tracer can be found in the movie in the supplementary material in Georgiou et al., 2019). This tracer advection is clearly steered by the eddy field. Once the tracer reaches area 1, which has been characterized as downwelling region, it can be advected by the mean boundary current and exported out of the Labrador Sea following the boundary current (Straneo et al., 2003).

This view is supported by the time evolution of the vertical distribution of the tracer averaged over the four areas that is shown in Figure 2.8. The tracer reaches area 1 after 4 months and only at depths larger than 500 m (Figure 2.8a). It peaks after 13 months at a depth of 1675 m and then reduces gradually over time. Although the tracer is partly initialized in area 2 (Figure 2.8b), its concentration peaks after 14 months and at a depth of 1412.5 m. This provides an indication that the tracer that reaches area 1 at depth is then advected by the mean boundary current towards area 2, and thereby contributes in the increase of the tracer concentration in area 2. Notably, the tracer peaks at shallower depths in area 2 than in area 1. This suggests that it follows the isopycnals, which are rising along the boundary (Figure 2.4b and Figure 2.7a). In area 3, the amount of tracer decreases from the start and hardly penetrates deeper than the initialization depth (Figure 2.8c). This is in line with the view that the tracer in area 3 is predominantly directly exported by the boundary current (Figure 2.7c-d). Lastly, in area 4 the amount of tracer reduces slowly over time (Figure 2.8d).

Figure 2.5 shows that the signal of the eddies extends to large depths, in line with the observational study by Lilly and Rhines (2002). A feature that stands out in Figure 2.7b-h is a small area (centered at x = 425 km and y = 865 km) with a peak tracer concentration that extends down to 2000m, which is tracer trapped in the core of an IR. This feature should not be mistaken for an indication that westward travelling IRs capture the dense waters. This specific IR was present in the region where the tracer was initialized, and hence the tracer was added to its core. The tracer subsequently remains captured in the eddy (see movie in the supplementary material in Georgiou et al., 2019). Nevertheless, the eddies do seem to indirectly govern the tracer advection. The tracer transport towards the boundary occurs because of the strong shear that is present in the velocity field around the eddies, and is strongest close to the region where the eddies are shed.

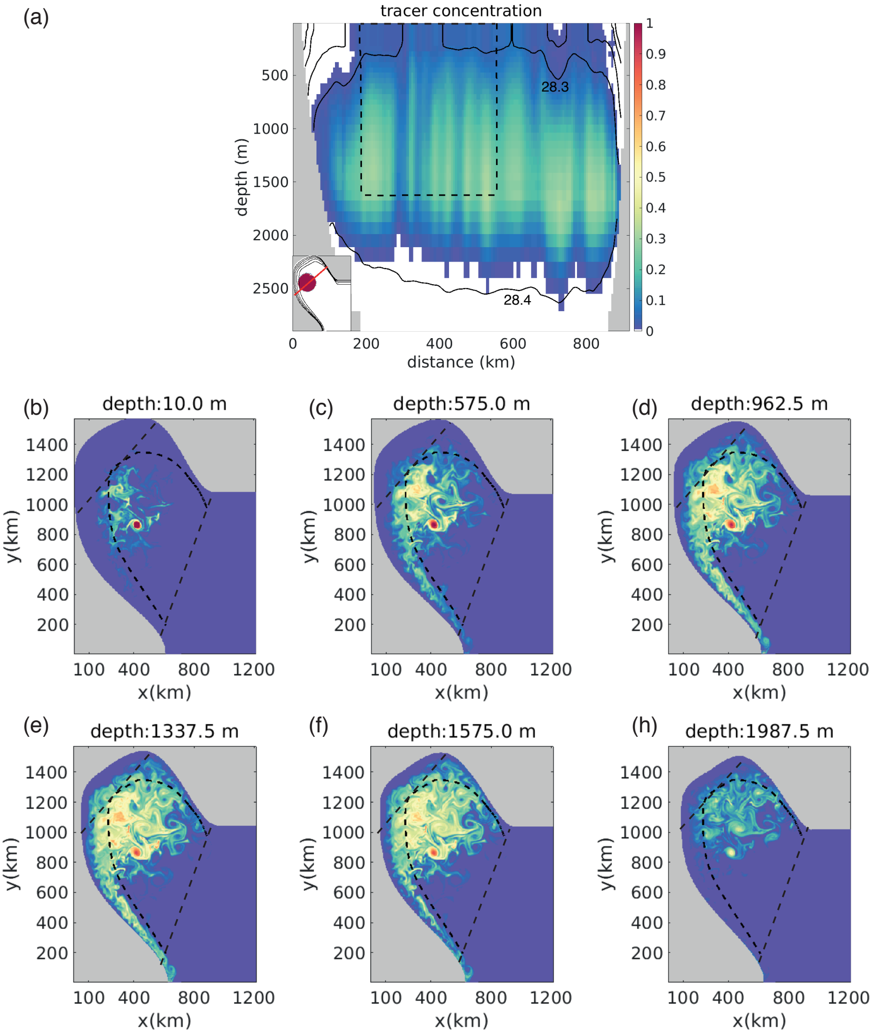

Figure 2.7: (a) Cross section of the vertical distribution of the passive tracer at the end of year 16 for REF, at the section indicated by the red line in the inset figure, together with the isopycnal surfaces (in kg m^{-3}, black contours). The passive tracer is released at the beginning of year 16 over a cylinder that coincides with the convection area (dashed lines and inset figure). (b-h) Snapshots of the concentration of the passive tracer 5 months after its release at a depth of (b) 10.0 m, (c) 575.0 m, (d) 962.5 m, (e) 1337.5 m, (f) 1575.0 m and (h) 1987.5 m. Black dashed lines denote the areas defined in Figure 2.6a.

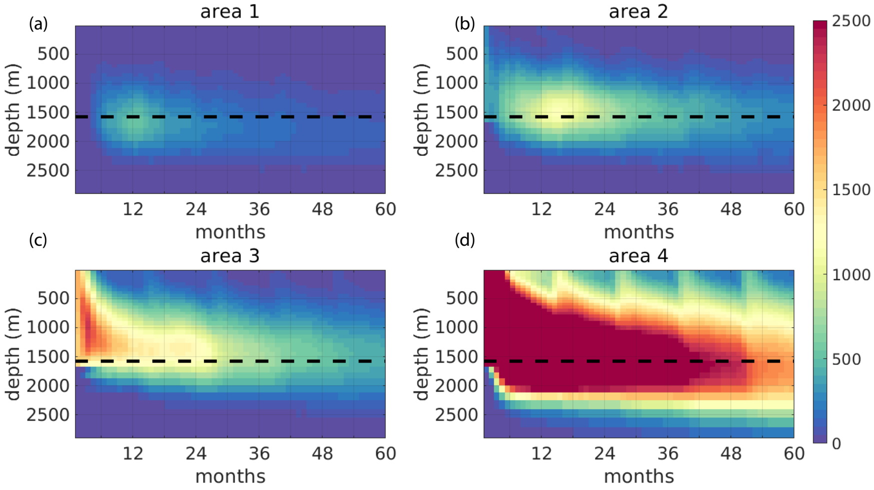

Figure 2.8: Time evolution of the total amount of passive tracer in depth, integrated over (a) area 1, (b) area 2, (c) area 3 and (d) area 4 for REF. The black dashed line denotes the initial maximum depth of the tracer. The areas are defined in Figure 2.6a.

2.4. Sensitivity to winter time surface heat loss

In this section, we assess the response of the eddies, convection and downwelling in two sensitivity simulations, in which the surface forcing is modified (see section 2.2.2 for details). Although the lateral eddy heat flux still balances the surface heat loss when the surface heat flux is changed in simulations COLD and WARM, as indicated by the regular seasonal cycle in the basin mean temperature (Figure 2.3), it is expected that the properties of both the MLD and the EKE change. First, we focus on the response of the convection and the eddy field in both simulations. Next, we assess the impact of the changes in the surface forcing on the downwelling and the spreading of dense waters.

2.4.1. Response of convection and the eddy field

Under the scenario of a stronger winter surface heat flux (COLD), one expects that the winter mixed layer deepens, that the convection region becomes wider, and that denser waters are produced. In addition, one also expects that as the temperature gradient between the interior and the boundary current increases due to stronger surface cooling, the eddy activity is enhanced (Saenko et al., 2014; de Jong et al., 2016). Figure 2.9a and Figure 2.9c illustrate that when the surface heat loss is increased, EKE is indeed more intense near the Greenland coast with a maximum of 750 $\mathrm{cm}^2\ \mathrm{s}^{-2}$, and the MLD becomes deeper, reaching depths of 2100 m. In WARM, the EKE is weaker (maximum value 575 $\mathrm{cm}^2\ \mathrm{s}^{-2}$, Figure 2.9b and Figure 2.9d) and the reduced surface heat loss results in a much shallower mixed layer, reaching depths of 960 m, and a narrower convective area. The model displays an asymmetric response of the MLD to changes in the heat flux: the same percentage change in the applied surface forcing results in changes of +25% (Figure 2.9c) and -45% (Figure 2.9d) in the maximum depth of the winter mixed layer. This asymmetry can be partly attributed to the stratification, which increases at larger depths, and partly to the changes in the baroclinicity of the boundary current and the associated eddy activity as is discussed in the next paragraph.

Figure 2.10 shows the eddy advection of heat for the three simulations. The eddy component of the advective heat flux is negative for the boundary current, while it is positive for the interior, once more confirming that the eddies extract heat from the boundary current and transport it towards the convection region. Also, the mean advection of heat in COLD and WARM changes (not shown). As for REF (Figure 2.3b-e), it almost cancels the eddy advection. The total heat advection balances the applied surface heat loss, confirming that an equilibrium is reached. Strong eddy heat fluxes originate from the regions with enhanced values of EKE that have been discussed in section 2.3 (i.e. along the Labrador coast and in particular at the steep West Greenland continental slope). In COLD, not only the eddy activity is stronger than in the REF case (Figure 2.9c) but also the eddy advection of heat from the boundary current into the interior is enhanced (Figure 2.10a). Thus, as the surface cooling is stronger, the restratification of the water column after convection also intensifies, counteracting the deepening of the convection induced by the increased surface heat loss. However, this negative feedback is apparently weaker than the direct impact of the increased surface heat loss on the convection depth, as the MLD deepens. In WARM, the surface heat loss is smaller, but the eddy heat advection into the interior weakens as well (Figure 2.10c). The eddy heat ad-

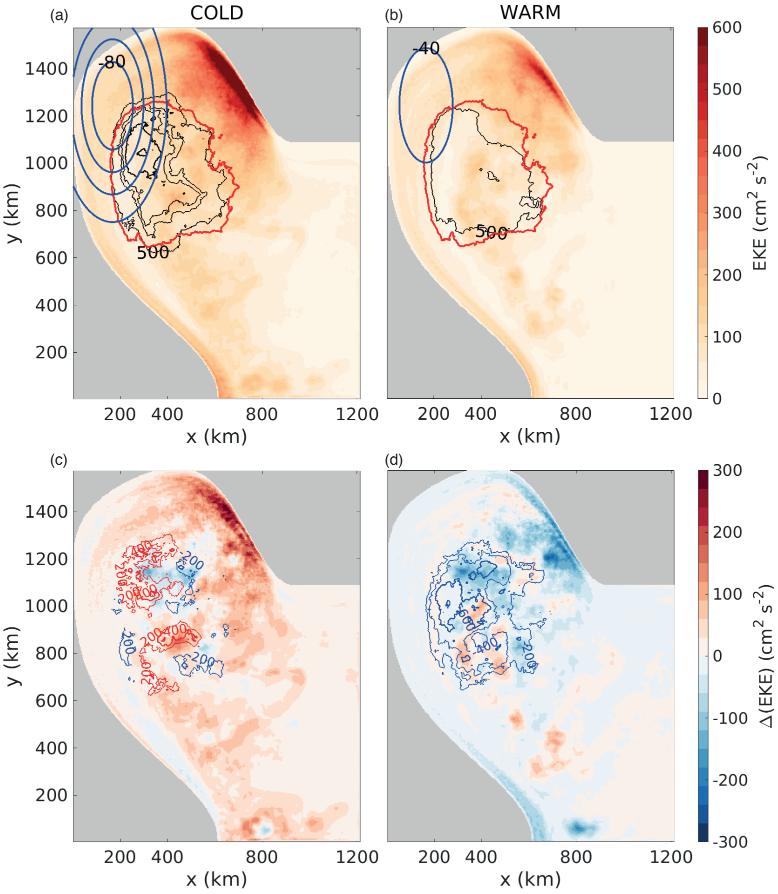

Figure 2.9: (a)-(b) Wintertime (February-March) MLD and EKE, as in Figure 2.4, but for the simulations (a) COLD and (b) WARM. (c)-(d) Anomalies from REF simulation of MLD (in m, contours) and EKE (in cm^2 s^{-2}, shading) for COLD and WARM, respectively. For comparison, the 500 m contour of the MLD for REF is shown in red in (a) and (b).

vection averaged over the interior (area 4, Figure 2.6a) amounts to 24 W m^{-2}, 28 W m^{-2} and 46 W m^{-2} for WARM, REF and COLD respectively. This confirms that changes in the eddy heat advection into the interior are not simply proportional to the changes in the applied heat loss and that the surface heat fluxes and lateral eddy fluxes combined regulate the properties of the convection.

So clearly, along the entire West Greenland continental slope both the EKE and the eddy component of the advective heat flux are affected by the changes in the wintertime heat loss (Figure 2.9c-d and Figure 2.10). It is likely that this change in the eddy field will affect the dynamics of the downwelling and therefore its magnitude as well.

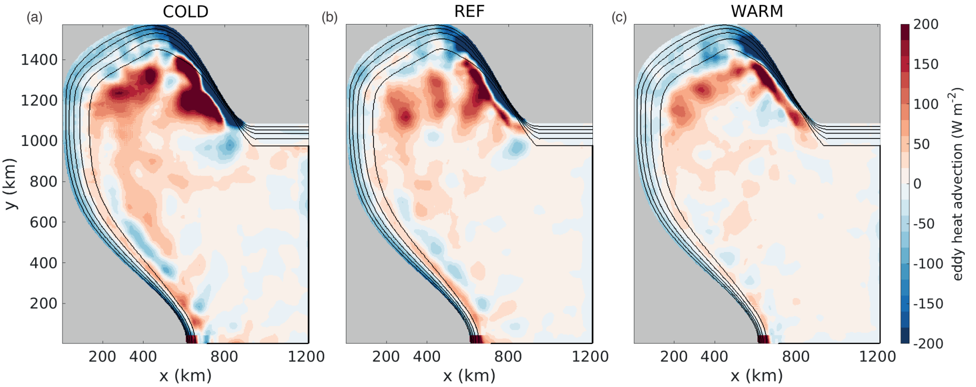

Figure 2.10: Depth integrated eddy advection of heat (in W m^{-2}) for (a) WARM, (b) REF and (c) COLD. Note that panel (b) is the same as Figure 2.3e and shown again here for easy comparison.

2.4.2. Response of the downwelling

Spall and Pickart (2001) and Straneo (2006a) state that the magnitude of the downwelling is controlled by the densification of the boundary current, suggesting that the magnitude of the downwelling will increase when the surface heat loss is stronger. Moreover, as shown in section 2.4, also the lateral eddy heat fluxes from the boundary current to the interior increase (Figure 2.10), which is expected to further increase the downwelling. To assess how changes in the surface heat fluxes regulate the magnitude of the downwelling in the Labrador Sea, we also analyze the vertical velocities of the simulations COLD and WARM.

Figure 2.11a shows that the time-mean vertical velocity integrated over the total domain is proportional to the applied surface heat loss. In response to an increase (decrease) of the winter heat loss by 50% compared to REF, the maximum basin-integrated downwelling increases (decreases) by 21% (-26%) or in terms of transport by +0.6 Sv (-0.8 Sv). In section 2.4, it has been shown that changes in surface heat losses influence the eddy field in the basin and this is now reflected in the magnitude of the downwelling. The downwelling in area 1 is the major contributor of the total downwelling in the basin. In COLD (WARM), the surface EKE at the west Greenland continental slope (area 1) becomes stronger (weaker) (Figure 2.9c-d) and the heat loss of the boundary current increases (decreases) (Figure 2.10a and Figure 2.10c) resulting in an increase (decrease) of the vertical transport in this region of +6% (-18%).

Next, we investigate whether the changes in the magnitude of the downwelling (Figure 2.11a) are related to changes in the properties of the boundary current in all simulations. Figure 2.11b and Figure 2.11c show the difference between the velocity ($\delta V = V_{\text{outflow}} - V_{\text{inflow}}$) and the density ($\delta\rho = \rho_{\text{outflow}} - \rho_{\text{inflow}}$), respectively, at the outflow and inflow for the three simulations. In all simulations the outflow gets more barotropic. There is a slight tendency for this barotropization to increase as the applied surface heat loss is stronger. The density difference between the outflow and the inflow (Figure 2.11c) shows that the upper layer of the boundary current becomes denser along the basin perimeter and that this density change increases with increasing heat loss. This can be attributed to both the surface forcing and lateral eddy heat advection of the boundary current (Figure 2.10). In REF, the density of the waters at the outflow is slightly larger than at the inflow in the lower part of the boundary current (z>400 m). In COLD, this difference is larger and the opposite holds for WARM. This is in line with the view emerging from Figure 2.7 that convected waters are entrained in the boundary current. The properties of the convected waters are in turn affected by the applied heat loss (i.e. denser in COLD than in WARM).

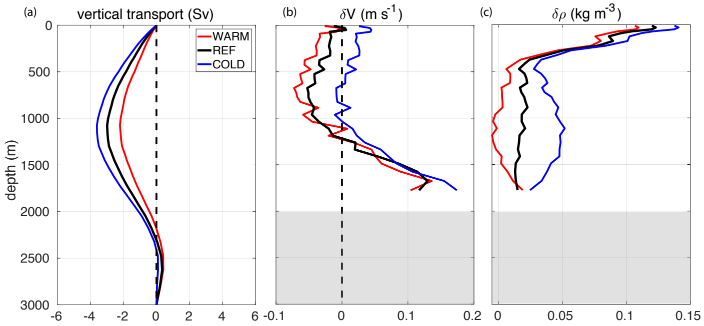

Figure 2.11: (a) Vertical transport integrated horizontally over the whole domain for all the simulations. (b-c) Difference of the mean (b) velocity ($\delta V = V_{\text{outflow}}$ - V_{inflow}), positive denotes an increase in the boundary current velocity and (c) density ($\delta\rho = \rho_{\text{outflow}} - \rho_{\text{inflow}}$) of the boundary current between the eastern (close to the outflow region) and western (close to the inflow region) side of the cross section shown in the inset figure of Figure 2.4b. All values are averages over the 5 years considered.

2.4.3. Response of the spreading of dense waters

Also in WARM and COLD we performed a tracer experiment to investigate the spreading of water masses that originate from the convection region. The tracer is initialized as described in section 2.3. Qualitatively, the behavior of the tracer in both WARM and COLD is the same as in REF, with a shallower pathway directly into the boundary current at the western side of the domain, and part of a deeper pathway towards Greenland (area 1). In all four areas, the depth at which the maximum tracer concentration occurs increases as the surface heat loss gets stronger and vice versa when the heat loss is reduced, and this is apparently affected by the convection depth. In particular, the concentration peaks at a depth of 1800 m and 1260 m for COLD and WARM in area 1, respectively (Figure 2.12). Surprisingly, the amount of tracer peaks earlier (after 7 months) in both WARM and COLD (Figure 2.12a and Figure 2.12b, respectively) than in REF induced by more vigorous eddy field. We observe similar behavior in area 2 and area 3 (not shown). The earlier peak in the concentration of the tracer in COLD may be related to the faster export of the convected waters than in REF. The finding that the timescale of this transport from interior towards the boundary does not display a simple relation to the heat loss emphasizes once more that complex interactions exist between convection and the eddy field.

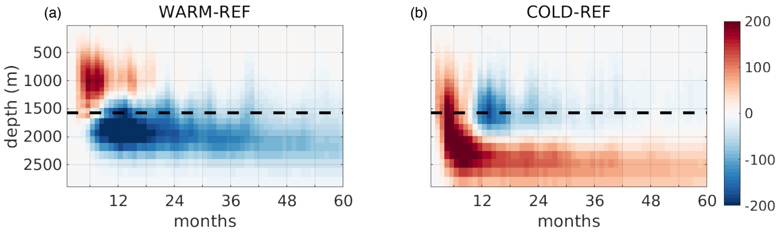

Figure 2.12: Difference in the time evolution of the total amount of tracer integrated over area 1 as a function of depth for (a) WARM, (b) COLD, with respect to the REF simulation shown in Figure 2.8a. The black dashed line denotes the initial maximum depth of the tracer.

2.5. Discussion

In the previous section, we showed that substantial downwelling is predominantly appearing in areas with strong eddy activity and the magnitude of the downwelling in these eddy-rich areas is positively correlated with the magnitude of the surface heat flux. This link between the wintertime cooling and the overturning in the North Atlantic has been pointed out in many numerical and observational studies (e.g. Biastoch et al., 2008; Curry et al., 1998), but here we demonstrate that this link is indirect (Figure 2.13).

As shown in this chapter, both the convection and the eddy field are affected by the changes in the surface forcing. In response to a stronger (weaker) surface winter heat loss, convection is stronger and the temperature gradient between the interior and the boundary current increases (decreases). This directly impacts the eddy field; as the temperature gradient increases, the baroclinicity of the boundary current increases, and the boundary current becomes more unstable.

While the generation of the eddies is known to be governed by local processes, their impacts are not restricted to their generation region since they propagate away towards the interior (Figure 2.4). As a result, the associated eddy heat transport from the boundary current towards the interior strengthens (Figure 2.9, Figure 2.10). This increases the heat loss of the boundary current, which in turn governs the magnitude of the downwelling (Spall and Pickart, 2001; Straneo, 2006a; Katsman et al., 2018), and at the same time provides a negative feedback on the convection depth. These idealized simulations thus highlight that complex interactions between the boundary current and interior are established via the eddy activity, and in concert determine the downwelling in the basin as well as the characteristics of convection.

In this chapter we focused on the Eulerian downwelling in depth space. This quantity is frequently used to describe the meridional overturning circulation, e.g. in the RAPID array (McCarthy et al., 2015), and in this regard it is of importance to understand the underlying physics and its sensitivity to changing surface forcing conditions. The view on the overturning based on this Eulerian downwelling differs from the view based on downwelling in density space (e.g. Mercier et al., 2015; Xu et al., 2016, 2018), which is a quantity that accounts for diapycnal processes and in particular dense water formation. While a full analysis of the watermass transformation in the basin is outside the scope of this study, we can estimate the overturning in our model using the theoretical framework outlined in Straneo (2006a).

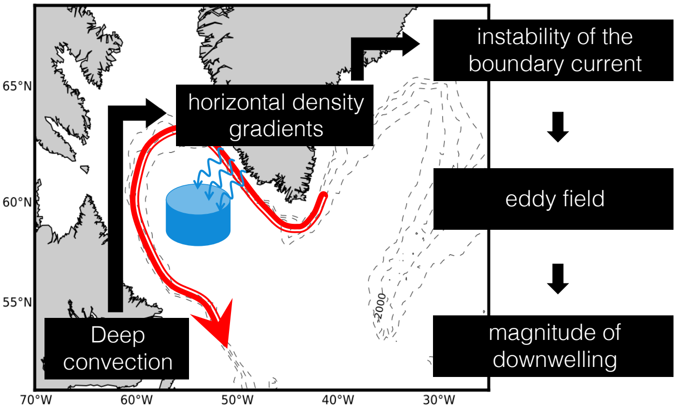

Figure 2.13: Schematic showing the indirect link between convection and downwelling strength. The horizontal density gradient between the interior and the boundary current (red arrow) set by convection (blue cylinder) affects the instability of the boundary current. The eddy field and the buoyancy loss of the boundary current along the west Greenland coast govern the dynamics of the downwelling in this region.

In Figure 2.4b one can clearly see a temperature difference between the eastern and western side of the displayed cross-section, which reflects the fact that the boundary current loses heat along its path. That is, the isotherms (or isopycnals) rise along the path of the boundary current between the eastern and western side of the domain. The associated reduction of the density gradient between the boundary and the interior yields a decrease of the baroclinic flow and, assuming no mass transport in cross-shore direction, a downward diapycnal transport in the boundary current (see Straneo (2006a) figure 1).

An analysis of the changes in the boundary current between the inflow and the outflow region in our model simulations reveals that in all three simulations the outflow indeed gets more barotropic: the transport in the upper 1000m reduces, and the transport below that increases (Figure 2.11b-c).

According to the two-layer model proposed by Straneo (2006a), the magnitude of the overturning w_o, i.e. the transport associated with diapycnal mass fluxes from the light to the dense layer in the boundary current, can be estimated from (Eq.17 in Straneo 2006a):

$$w_o = L\int_0^P h_2 \frac{\partial V_2}{\partial l} dl \tag{2.1}$$

where L is the width of the boundary current, V_2 the velocity of the dense lower layer, P the total perimeter of the domain and l the along-boundary coordinate. To assess w_o from our model simulations, we choose the $\sigma = 28.32$ kg m^{-3}, isopycnal as the boundary between the light and dense layer (Figure 2.4b). We define the width of the boundary current by the location of the 18 Sv streamline of the barotropic streamfunction (vertical red line in Figure 2.4b), which yields $L = 66$ km. When we average the velocity of the dense layer at inflow and outflow across the boundary current, an increase of $\Delta V_2 = +0.04$ m s^{-1} in the velocity of the denser part of the water column is found. According to Eq. 2.1, this yields an overturning of $w_o = 2.7$ Sv, which is slightly smaller than the Eulerian downwelling calculated directly from the vertical velocity field in our model (i.e. 3.0 Sv).

The result that the changing properties of the boundary current yield an overturning does not necessarily imply that all diapycnal mixing (i.e. transformation of watermasses) also takes place within the boundary, as it has been assumed in Straneo (2006a). Our tracer analysis shows that dense waters in the interior of the Labrador Sea are directly entrained in the boundary current at shallower depths at the western side of the basin. In deeper layers, the tracer moves towards the downwelling region near Greenland (Figure 2.7d-h), and is then entrained in the boundary current. Thereby, the assumption that the eddy activity only yields a lateral buoyancy transport and no mass transport, applied in the model by Straneo (2006a), may not be correct. The pathways and the timescales by which this transport of dense waters towards the boundary occurs are complex and will be addressed in more detail in a follow up study focusing on the differences and connections between the Eulerian downwelling and downwelling in density space.

2.6. Summary and conclusions

In this chapter we explore how changes in the surface heat fluxes affect the magnitude of the downwelling, the evolution of deep ocean convection in the Labrador Sea and their interplay through the eddy activity. The motivation of this study stems from the need to improve our understanding of the location where the downwelling takes place at high latitudes and its response to changes in the forcing conditions in light of a changing climate.

Under the simplifications of an idealized model for the Labrador Sea region, our analysis once more emphasizes that the presence of the IRs is crucial to balance the heat loss over the basin (Figure 2.3) and to represent the restratification of the interior of the Labrador Sea (Katsman et al., 2004; Hátún et al., 2007; Gelderloos et al., 2011; de Jong et al., 2016; Kawasaki and Hasumi, 2014; Saenko et al., 2014). In addition, this study once more underlines that with a proper representation of the mesoscale activity in the Labrador Sea the model can reproduce the winter mixed layer depths and in particular the location of deep convection (Figure 2.4a) seen in observations (Pickart et al., 2002; Våge et al., 2009).

The model results show a total Eulerian downwelling in the basin of 3.0 Sv at a depth of 1000 m. Spall and Pickart (2001) estimated the magnitude of the net downward transport in the Labrador Sea, based on observations of the alongshore density variations, to be roughly of 1.0 Sv in the basin. In their recent study, Holte and Straneo (2017) used horizontal velocity sections based on Argo floats to investigate the overturning in the Labrador Sea and its variability and found a mean overturning of 0.9 ± 0.5 Sv. The total net downwelling in our idealized model is in the same order of magnitude as these observation-based estimates, albeit stronger. However, in both studies, the downwelling is deduced from the large-scale hydrography rather than observed directly and also the number of available observations is limited.

The downwelling is concentrated along the lateral boundaries and not where the heat loss is strongest or where convection is deepest. Moreover, our analysis shows that this near-boundary vertical transport is not uniform: the area where the IRs are formed contributes by far the most to the total downwelling (almost 4.0 Sv of downward transport). In addition, it has been shown that the time- and basin- mean downwelling is proportional to the applied surface heat loss, while the downwelling near the Greenland coast (area 1) displays a non-linear response to the change in heat loss.

This study emphasizes that a proper representation of the eddy field in models is one of the key elements for representing the interplay between the downwelling and convection in marginal seas at high latitudes, and their responses to changing forcing conditions. The outcome that eddies are a crucial element in the chain of events, determining changes in downwelling in the North Atlantic Ocean and hence changes in the strength of the AMOC, obviously raises the question if climate-change scenarios for AMOC changes based on coarse, non-eddy resolving climate models can properly represent the physical processes at hand. A first study that addresses this subject (Katsman et al., 2018) showed that while also in complex models the downwelling occurs near the boundary, the processes thought to govern the downwelling are not well represented in the coarse ocean model that was studied. An obvious next step is to carefully evaluate the response of the downwelling to changing forcing conditions in such coarse resolution climate models.

Chapter 3

Pathways of the water masses exiting the Labrador Sea: the importance of boundary-interior exchanges

The water masses exiting the Labrador Sea, and in particular the dense water mass formed by convection (i.e. Labrador Sea Water, LSW), are important components of the Atlantic Meridional Overturning Circulation (AMOC). Several studies have questioned the connection of the LSW production to the AMOC variability. This is partly due to the limited understanding of how this locally formed water mass leaves the interior of the Labrador Sea. In this study, the pathways and the timescales of the water masses exiting the Labrador Sea via the boundary current are investigated by Lagrangian particle tracking. This method is applied to the output of a strongly-eddying idealized model that is capable of representing the essential physical processes involved in the cycle of convection and restratification in the Labrador Sea. The Lagrangian trajectories reveal that prior to exiting the domain the water masses follow either a fast route within the boundary current or a slower route that involves boundary current-interior exchanges. The densest water masses exiting the Labrador Sea stem from this slow route, where particles experience strong water mass transformation while in the interior. In contrast, the particles that follow the fast route experience water mass transformation in the boundary current at the western side of the domain only, yielding a lighter product. Although both routes carry roughly the same transport, we show that 60% of the overturning in density space is associated with the volume transport carried by particles that follow the slow route. This study further highlights that the export of dense water masses, which is governed by the eddy activity in the basin, yields export timescales that are usually longer than a year. This underlines the necessity of resolving the mesoscale features required to capture the interior-boundary current exchange in order to correctly represent the export of the LSW.

This chapter has been published in *Ocean Modelling* (2020).

3.1. Introduction

The Atlantic Meridional Overturning Circulation (AMOC) describes the conversion of lighter, shallow Atlantic water masses flowing northward into denser, deep water masses flowing southward, involving diabatic processes like deep convection in the marginal seas of the North Atlantic. The strength of the AMOC is commonly estimated as the total northward transport in the upper 1000m or so of the water column and can be either viewed in depth space, emphasizing the vertical transport (Wunsch and Heimbach, 2006; Cunningham et al., 2007) or in density space emphasizing the transformation of lighter to denser water masses (e.g., Xu et al., 2016; Li et al., 2017; Desbruyères et al., 2019; Lozier et al., 2019; Brüggemann and Katsman, 2019). Climate model studies suggest a substantial weakening of the AMOC over the 21st century (Collins et al., 2013; Weijer et al., 2019), with the potential to affect the global climate. Therefore, over the last decade, there has been an increased effort to understand the drivers of AMOC variability (e.g., Johnson et al., 2019; Lozier et al., 2019).

One of these potential drivers is the process of deep convection in the Labrador Sea, resulting in the production of Labrador Sea Water (LSW); one of the water masses that contribute to the lower limb of the AMOC (e.g., Rhein et al., 2017). While earlier modelling studies have suggested a close connection between the LSW production and AMOC variability (Biastoch et al., 2008; Zhang, 2010; Yeager and Danabasoglu, 2014), up-to-date observations at the RAPID 26^oN (Smeed et al., 2018) and OSNAP (Lozier et al., 2019) arrays and recent numerical studies (Zou and Lozier, 2016; Li and Lozier, 2018; Georgiou et al., 2019) have cast doubts on this, suggesting a rather complex connection between the two. Moreover, the recent study of Lozier et al. (2019) suggests that the variability of the overturning is dominated by the water mass transformation taking place in the eastern half of subpolar gyre rather than in the Labrador Sea.

The recent debate on the importance of the LSW for AMOC variability is partly the result of limited understanding on how this water mass leaves the interior of the Labrador Sea, in particular about its export routes and the associated timescales. Several studies showed that newly-formed LSW is rapidly exported by spreading laterally and entraining in the Deep Western Boundary Current (DWBC) near the Labrador coast (e.g., Talley and McCartney, 1982; Brandt et al., 2007; Feucher et al., 2019). Moreover, a mid-depth recirculation of the LSW within the subpolar gyre has been reported in a number of studies (e.g., Lavender et al., 2000; Pickart et al., 2003; Stramma et al., 2004; Bower et al., 2009; Holliday et al., 2009; Lozier et al., 2013). Last, a slower export route has been suggested in the studies of Straneo et al. (2003) and Palter et al. (2008). In particular, they identify the existence of a pathway which transports convected water from the interior towards the West coast of Greenland. These multiple export routes of LSW, of which the relative importance is still unclear, might result in a complex relation between the LSW formation and its export timescales, and the AMOC variability.

The recent highly idealized numerical study of a convective marginal sea by Brüggemann and Katsman (2019) clearly highlights the important role of the exchange of waters between the interior and the boundary current, which in turn is governed by the eddy activity, for the export pathways of convected water and the associated timescales. Their results indicated that the densest water masses are formed in the interior and are laterally steered towards the region of high eddy activity and then entrained in the boundary current, thus following an indirect route to leave the marginal sea. In addition, they showed that a lighter product of convection within the boundary current itself is directly and rapidly exported via that boundary current. The underlying idea of an eddy-induced entrainment of LSW in the boundary current was pointed out by Khatiwala and Visbeck (2000). However, they linked this entrainment to the summertime restratification process and the associated horizontal density gradients. That is, they assumed no spatial variations and by linking it to the restratification implied that this only occurs in summer. In contrast, both Brüggemann and Katsman (2019) and chapter 2, show that there is a preferred region for the re-entrainment, which coincides with the region where the eddy activity peaks. However, both studies conclude this based on an analysis of passive tracers, which does not allow the investigation of the pathways and transformation of water masses, which in the end determine the LSW export.

The direct and indirect export routes of the convected water recently identified in idealized models (chapter 2 and in Brüggemann and Katsman, 2019) are in line with the indications of such routes from observations (e.g., Palter et al., 2008; Bower et al., 2009). However, due to the limited number of observations, the relative importance of a direct export route on the Labrador side of the basin and an indirect route via the Greenland coast is yet unclear.

In this study, we analyze the origin and transformation of different water masses found within the boundary current at the exit of the Labrador Sea. We use a Lagrangian approach applied to the output from the idealized model used in chapter 2, which allows us to elucidate the complex structure of the flow (Bower et al., 2019). From this we distinguish different pathways, identify where water mass transformation occurs and assess what role the prominent eddy field plays for exporting these water masses. This idealized model study provides helpful insights on the nature of the interior-boundary current exchange and its role for the LSW export. The results can guide the analyses of observations and more realistic model simulations, thus improving our overall understanding of the AMOC.

The structure of this chapter is as follows. The model setup and the Lagrangian approach are described in section 3.2. First, the pathways that the water masses follow before exiting the Labrador Sea are analyzed in section 3.3. Next, we explore the importance of each pathway for the net overturning in depth and density space (section 3.4) and the location where the water masses subduct (section 3.5). In section 3.6, we focus on the lateral exchange between the boundary current and the interior by identifying the locations where this exchange occurs and how it affects the properties of the water masses exiting the Labrador Sea. The associated export timescales are addressed in section 3.7, followed by a discussion and conclusions in section 3.8.

3.2. Numerical model and methods

3.2.1. Model configuration and flow characteristics

The numerical simulation analyzed in this study is carried out using a hydrostatic configuration of the MITgcm (Marshall et al., 1997). The model configuration captures the key features of the circulation in the Labrador Sea, like the annual cycle of the convection and restratification and the properties of the mesoscale eddy field. This model and its results have been previously used in section 2.2 and we refer the reader to this chapter for a more detailed description of the model setup. A short description of the model setup and the main flow characteristics are presented in the following paragraphs.

The model has a horizontal resolution of 3.75 km and 40 levels in the vertical with a resolution of 20 m in the upper layers up to 200 m at a maximum depth of 3000 m. The model domain has two open boundaries (each roughly 100 km wide), one in the northeast and one in the southwest, where a boundary current enters and exits the domain. All other boundaries are closed (Figure 3.1). At the northeastern open boundary, a warm boundary current is specified by a meridional temperature field $T_{in}(y, z)$ and a westward flow $U_{in}(y, z)$ in geostrophic balance with this prescribed temperature distribution. A sinusoidal seasonally varying term is added to the inflow conditions to mimic the observed seasonal variability of the West Greenland Current ($\Delta U_{max} = 0.4$ m s^{-1}, with maximum and minimum in September and March respectively, Kulan and Myers 2009; Rykova et al. 2015). Note that total outflow transport is prescribed, but the properties of the boundary current at the outflow are determined by the internal model dynamics. Following the topography, this boundary current flows cyclonically around the basin (Figure 3.1a). At the northwestern side, a narrowing of the topography is present (grey contours in Figure 3.1a) as observed near the west coast of Greenland. This steepening leads to an increased instability of the boundary current and mostly warm anticyclonic eddies are shed, with similar characteristics as the Irminger Rings (IRs) as shown in Katsman et al. (2004), Gelderloos et al. (2011) and chapter 2. At the surface, a temporally and spatially varying surface heat flux is applied resulting in a net annual heat loss of 18 W m^{-2} over the entire model domain (blue contours in Figure 3.1b).

A linear equation of state is used, with temperature as the only active tracer. Note that the effects of salinity are not incorporated in the model although in reality the lateral fresh water flux carried by the IRs (e.g., de Jong et al., 2016) influences the properties of convection (e.g., Gelderloos et al., 2012). In this study our focus is on the dynamics that control the interior-boundary current exchange in the Labrador Sea, and hence the effects of salinity are omitted in the model for simplicity.

As a result of the applied surface heat loss (blue contours in Figure 3.1b) the model displays deep convection in the interior. The winter mean mixed layer reaches a depth of 1700 m (Figure 3.1b). As shown in chapter 2, the deepest mixed layers are located away from areas with strong eddy activity (red contours in Figure 3.1b) albeit slightly closer to the maximum of buoyancy loss than observed. In the regions of strong eddy activity the associated eddy heat transport from the boundary current towards the interior is stronger and the water column is too stratified to sustain deep convection. In the model we do not consider the shelf and overflow waters or the effects of wind (Gelderloos et al., 2011), and prescribe a transport at the inflow (19.7 Sv) that is weaker than estimates over the full depth (40-50 Sv, Pickart et al., 2002; Fischer et al., 2004). The maximum barotropic streamfunction is about 27 Sv (Figure 3.1c) due to some recirculation in the basin. In this study, we use the three dimensional velocity field from the last six years of the reference simulation (i.e. model years 15-20) described in chapter 2 to track Lagrangian particles.

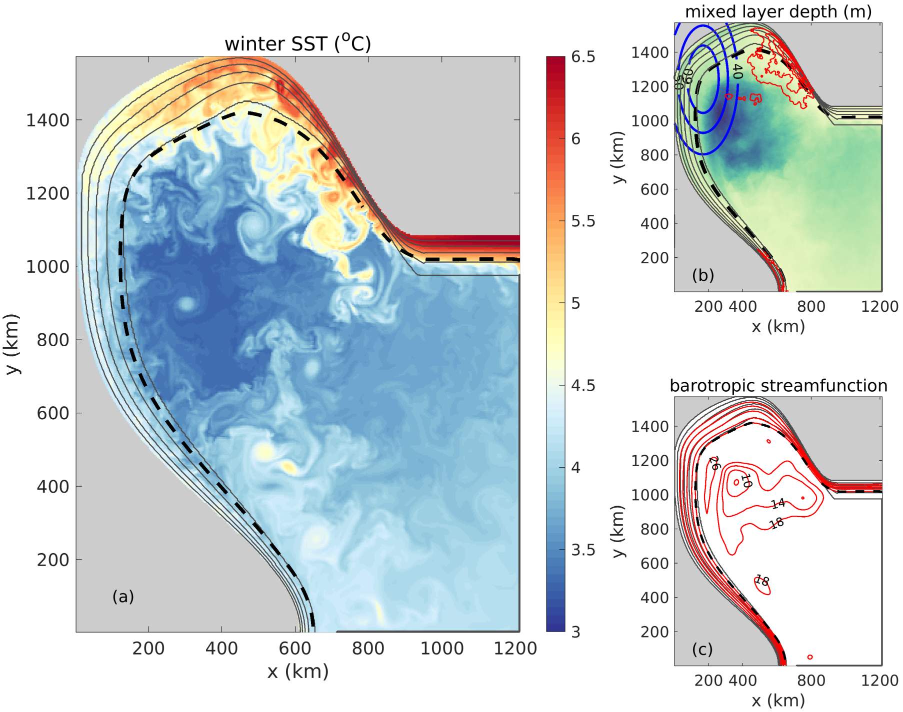

Figure 3.1: (a) Snapshot of the sea surface temperature (SST) in mid-March of model year 16. (b) Winter (February-March) mixed layer depth (MLD in m, shading), eddy kinetic energy (EKE, red contours, contour interval is 200 $cm^2\ s^{-2}$) and annual mean surface heat flux (contours in blue, contour interval is 10 $W\ m^{-2}$). (c) Mean barotropic streamfunction (Ψ_b, contour interval is 4 Sv). All model data are from the reference simulation described in chapter 2; values in (b) and (c) are averaged over years 16-20. In all figures, black dashed line indicates the 18 Sv contour line of Ψ_b and grey contours outline the bathymetry (contour interval is 500 m starting from the isobath of 500 m).

3.2.2. Lagrangian particle tracking

The offline Lagrangian tool Connectivity Modeling System (CMS, Paris et al., 2013) is used to investigate the possible pathways of the waters exiting the model domain and water mass transformation that occurs along these pathways. To this end, numerical particles are released at the outflow region in the south (the only export route of the convected water mass out of the domain). The particles are advected backward in time using a timestep of 1 hour within the 2-day snapshots of the three dimensional velocity fields of the simulation described in the previous section. The movement of the numerical particles is parameterized as described by Paris et al. (2013): a Runge-Kutta 4th order stepping in time and a tricubic spatial interpolation are used to determine the location of the particles; no additional horizontal diffusivity is applied. To account for the increased vertical diffusion during the process of convection, particles that are located within the mixed layer are moved randomly in the vertical within the mixed layer with a maximum velocity of w=10 cm s^{-1} (van Sebille et al., 2013).

Particles are released at the outflow (y=3.75 km, red line in Figure 3.2a) every 2 days over a period of one year with a particle resolution of 1 km in the zonal direction and 50 m vertically and are traced backward in time. Doing so, we track 217349 Lagrangian particles over a period of 6 years. Since we are interested in distinguishing the pathways of the water masses in terms of volume transport, a volume transport is assigned to each particle upon release and it is conserved along the trajectory (van Sebille et al., 2018). This is determined by multiplying the meridional velocity by the area of the grid cell in which the particle is released (Döös, 1995; Ypma et al., 2019). Although the particles were released at the outflow and tracked backwards, we will mostly refer to their trajectories forward in time.

3.3. Upstream pathways of the water masses exiting the LS

In this study, we explore the origin of the waters found in the boundary current at the outflow of the Labrador Sea. In particular, we investigate the role of exchange water between the boundary current and the interior. To this end, we define a particle as being in the interior when it is offshore of the 18 Sv contour line of the 5-year mean barotropic streamfunction (Ψ_b, black dashed line in Figure 3.1 and Figure 3.2a). To filter out possible short and fast excursions of particles into the interior and back, we also require that the particle stays offshore of this streamline for more than 20 days. The results of the analyses presented in this study are not very sensitive to the exact choice made for distinguishing the boundary current from the interior: the presented results are consistent for different choices of Ψ_b or using an isobath.

Within the 6 year advection time, 90% of the particles (i.e. 195528 particles) reach the eastern open boundary (inflow). Since these particles travel from the inflow towards the outflow we will refer to them as *wholeLoop* particles. The 10% of the particles that remain in the basin during the 6 year simulation are referred to as *interiorLong* particles.

A particle density plot (Figure 3.2a) highlights the paths that the *wholeLoop* and *interiorLong* particles are prone to follow. It is constructed by regridding the position of each particle at every timestep on an x-y grid with a resolution of 3.75 km. This particle density is calculated as described in Ypma et al. (2019); at each location (in the new grid) the transport assigned to each particle is divided by the total transport carried by the particles. In the interior, the particle density is enhanced at the northwestern side of the basin (close to the topographic narrowing, Figure 3.2a). This indicates that a significant number of particles enter the interior of the basin there, suggesting a connection with the eddy activity found at this location (Figure 3.1b). However, such a possible connection is masked by the fact that the highest particle density occurs along the boundary current, which suggests that the particles are found somewhere within the boundary current during their lifetime. We therefore subdivide the *wholeLoop* particles in two groups: particles that cross the 18 Sv contour line of Ψ_b into the interior at some location (hereinafter, *interiorShort* particles) and particles that never cross the 18 Sv contour line and thus never leave the boundary current (hereinafter, *withinBC* particles). It appears that of all the *wholeLoop* particles, 60% falls into the *interiorShort* category and 40% in the *withinBC* category (Figure 3.3). The volume transport carried by the $withinBC$, *interiorShort* and *interiorLong* particles amounts to 6.8 Sv, 8.4 Sv and 2.0 Sv, respectively

(Figure 3.3). Note that at the eastern side of the domain (x>800 km and y<1000 km) the particle density is low (< 1%, Figure 3.2a). This reflects the weak circulation in this part of the domain (Figure 3.1c). This is a consequence of the closed southeastern boundary of the idealized model. The bathymetry forces the boundary current to follow the northern and western side of the domain.

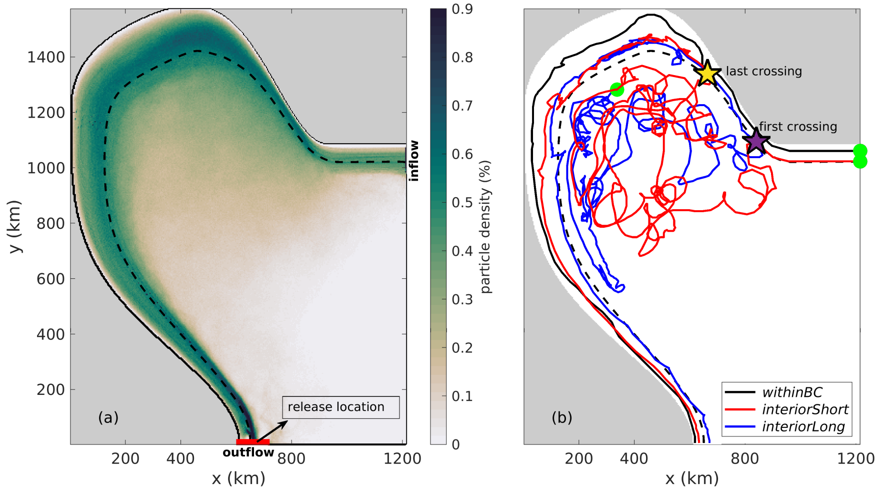

Figure 3.2: (a) Density of the position of particles released at y= 3.75 km (red line). The black dashed line shows the 18 Sv barotropic streamfunction (Ψ_b) which is used to distinguish the boundary current from the interior. (b) Example trajectories of a particle following the boundary current (*withinBC*, black line), a particle crossing into the interior (*interiorShort*, red line) and a particle that does not leave the basin during the 6-year simulation (*interiorLong*, blue line). The purple (yellow) star indicates the location where the example *interiorShort* particle crosses the 18 Sv barotropic streamfunction (dashed line) for the first (last) time. Green circles indicate the location of the particles at the end of the backward advection time (i.e. at t = 6 years).

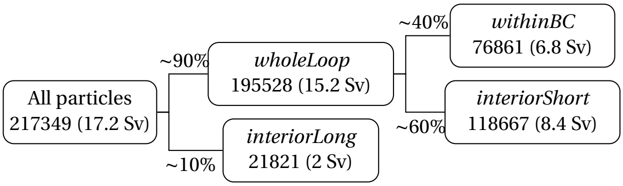

Figure 3.3: Schematic showing the number, percentage and associated volume transport of particles that fall into various categories; *wholeLoop* particles travel from the inflow towards the outflow, *interiorShort* particles cross the 18 Sv contour line of Ψ_b into the interior and back, *withinBC* particles never leave the boundary current. Last, *interiorLong* particles remain in the basin during the 6 year simulation. Examples of pathway for *withinBC*, *interiorShort* and *interiorLong* are shown in Figure 3.2b.

By construction, the *withinBC* particles (black line in Figure 3.2b) are always onshore of the 18 Sv contour line of Ψ_b. The *interiorShort* particles (red line in Figure 3.2b) also travel from the inflow to the outflow but along their path, they enter the interior (purple star in Figure 3.2b) and re-enter the boundary current (yellow star in Figure 3.2b) before exiting the domain. Last, the *interiorLong* particles recirculate in the interior of the basin for more than 6 years (blue line in Figure 3.2b).

Most of the *withinBC* particles reside close to the lateral boundaries at both the inflow and the outflow (black contours in Figure 3.4). The particles that enter the interior and leave the domain within the simulated advection time (*interiorShort*, red contours in Figure 3.4) originate farther offshore (y = 1020-1060 km) than the *withinBC* particles (y = 1040-1080 km, Figure 3.4b). Since they are at the flank of the boundary current at the inflow (Figure 3.4b), they can more easily leave the boundary current and enter the interior. Similarly, when they re-enter the boundary current, they are found on its offshore flank (Figure 3.4a), but deeper in the water column. Last, the *interiorLong* particles are found in the deepest part of the boundary current (blue contours in Figure 3.4a). Apparently, they represent the densest water masses exiting the domain.

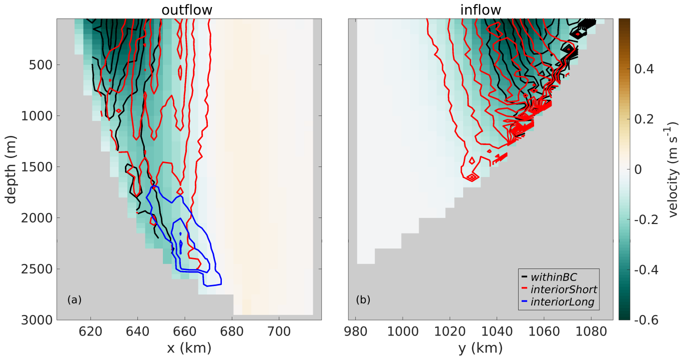

Figure 3.4: Section across (a) the outflow (at y= 3.75 km) and (b) the inflow (at x= 1215 km) showing the number of Lagrangian particles that follow the three pathways: *withinBC* (black contours), *interiorShort* (red contours) and *interiorLong* (blue contours) together with the 5 year mean velocity of the simulation (shading). The contour interval is 100 particles.

3.4. Overturning in depth and density space

The particles that represent the three pathways of the water masses prior to exiting the Labrador Sea display a depth change (Figure 3.4), which is a reflection of overturning in depth space in the basin. Moreover, using the same model setup, it is shown from an Eulerian perspective that the boundary current gets denser along its path through the Labrador Sea, yielding a net overturning in density space (section 2.5). In this section, we analyze this overturning both in depth and density space from a Lagrangian perspective and investigate the relative contribution of the different pathways to this net overturning.

3.4.1. Transport changes between the inflow and outflow in depth space

Since each of the particles represents a particular transport of water masses (section 3.2.2), we can convert the depth changes of particles between inflow (green bars) and outflow (orange bars) to the associated volume transport (Figure 3.5). Three vertical layers are defined to facilitate discussion; 0-500 m, 500-1500 m and 1500-3000 m (black horizontal lines in Figure 3.5a-c). At the inflow, almost all transport carried by either the *withinBC* or the *interiorShort* particles, is found shallower than 1500 m (6.8 Sv and 8.2 Sv respectively). This view changes at the outflow of the domain: the volume transport in the deepest layer (1500 - 3000 m) increases by 1.3 Sv for the *withinBC* and by 2.0 Sv for the *interiorShort* particles. In addition, the presence of the *interiorLong* particles at the outflow becomes apparent in this depth layer as a volume transport of 1.8 Sv (90% of the total transport these particles represent).

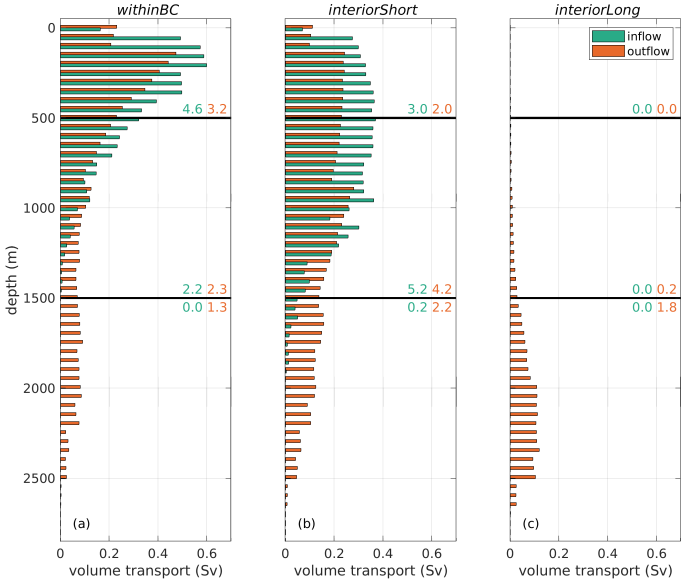

Figure 3.5: Volume transport (in Sv) at the inflow (green bars) and outflow (orange bars) binned every 50 m in depth space for the particle categories (a) *withinBC*, (b) *interiorShort* and (c) *interiorLong*. Black horizontal lines distinguish (a-c) three depth layers (0-500 m, 500-1500 m and 1500-3000 m); the values in green (orange) represent the total transport in each layer at the inflow (outflow).

3.4.2. Transport changes between the inflow and outflow in density space

Similarly, we can explore the water mass transformation that occurs between inflow and outflow from a Lagrangian perspective. Since the density in the model is associated only with temperature variations (section 3.2.1), we examine the temperature changes between inflow and outflow for each pathway. At the inflow, most of the *withinBC* particles carry warm water masses (green bars in Figure 3.6a). A shift in transport of warmer to colder water masses between inflow and outflow reveals that water mass transformation occurs within the boundary current. Since the *interiorShort* particles originate farther offshore in the boundary current (Figure 3.4b), they are characterized by lower temperatures at the inflow (green bars in Figure 3.6b). Also for this category, the transport in colder layers increases towards the outflow indicating that the particles experience water mass transformation along their path. Last, the *interiorLong* particles represent the coldest water masses at the outflow (Figure 3.6c).

To quantify the water mass transformation in density space, the total volume transport at the inflow (outflow) is summarized in Figure 3.6 for three water mass definitions: surface waters ($T > 3.5\ ^{o}$C), intermediate waters ($3.2 < T \leqslant 3.5\ ^{o}$C) and deep waters ($T \leqslant 3.2\ ^{o}$C). Note that T=3.2-3.5^{o}C is the temperature range corresponding to the convected water mass (section 2.3.1). The transport change between inflow and outflow in temperature space through the 3.5 ^{o}C isotherm derived from the particles amounts to (1.3+1.1)-0.2 = 2.2 Sv for *withinBC* (Figure 3.6a) and to (3.6+2.0)-(2.1+0.3) = 3.2 Sv for *interiorShort* (Figure 3.6b). Furthermore, the transport of water masses below 3.5 ^{o}C at the outflow is substantially higher for both the *interiorShort* and *interiorLong* particles (7.6 Sv combined, Figure 3.6b-c) than for the *withinBC* (2.4 Sv, Figure 3.6a).

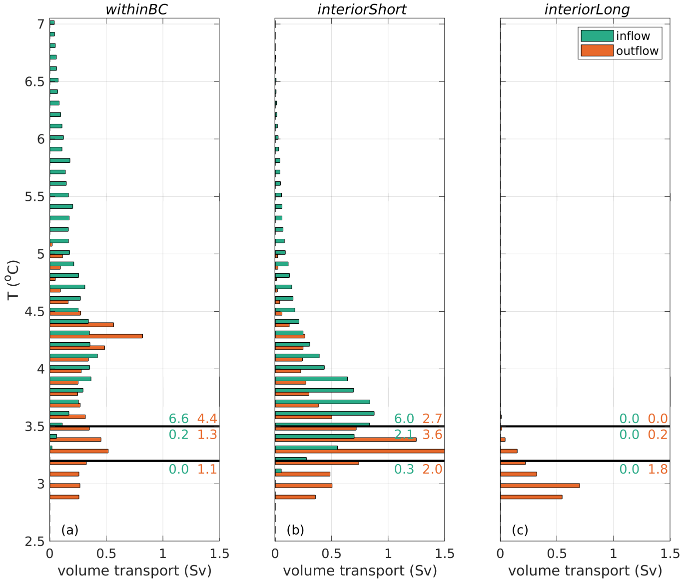

Figure 3.6: Volume transport (in Sv) at the inflow (green bars) and outflow (orange bars) binned every 0.1 ^{o}C in temperature space for the particle categories (a) *withinBC*, (b) *interiorShort* and (c) *interiorLong*. Black horizontal lines distinguish three water mass definitions: surface waters ($T > 3.5\ ^{o}$C), intermediate waters ($3.2 < T \leqslant 3.5\ ^{o}$C) and deep waters ($T \leqslant 3.2\ ^{o}$C); the values in green (orange) represent the total transport for each water mass at the inflow (outflow). Note that the intermediate waters correspond to the temperature range of the convected water mass (section 2.3.1).

3.4.3. Overturning from the Eulerian and the Lagrangian perspective

Based on Figure 3.5 and Figure 3.6, we can estimate the overturning in both depth and density space and compare this to the overturning calculated from the Eulerian velocities. The Eulerian overturning in depth space is defined as the difference in time-mean transport between the inflow and the outflow in model year 15, integrated over the same depth bins (depth space) or temperature bins (density space). Next, we calculate the Lagrangian overturning for each pathway, by taking the difference between the summed volume transport carried by all particles in a certain depth or density bin at the outflow and at the inflow. This is done for all three particle categories. Since the *interiorLong* particles never reach the inflow, the total mean Lagrangian overturning estimate is based solely on the transports carried by the *withinBC* and *interiorShort* particles. We do not expect the Eulerian and Lagrangian overturning estimates to match exactly as we lack information on the overturning associated with the *interiorLong* particles since we cannot follow them backwards in time towards the inflow.

However, the overturning derived from the particles largely agrees with the overturning obtained from the time mean Eulerian flow (compare the purple and green lines in Figure 3.7), which suggests that we can use the overturning split in pathways to get an impression of the importance of each route. In depth space, the maximum Eulerian (Lagrangian) overturning occurs at 1000 m depth and amounts to -3.8 (-4.1) Sv (Figure 3.7b). Both *withinBC* and *interiorShort* particles contribute equally to the Lagrangian overturning in depth space. In addition, the presence of the *interiorLong* particles at the outflow becomes apparent in depths greater than 1000 m.

In density space, the overturning in both the Eulerian and Lagrangian view, peaks at a temperature of 3.5 ^{o}C and amounts to -3.4 and -5.4 Sv, respectively (Figure 3.7d). When the contributions of the transport carried by each pathway to the net overturning in density space are considered, it appears that 60% of the maximum overturning (at T = 3.5 ^{o}C) can be attributed to the *interiorShort* particles and 40% to the *withinBC* particles. In contrast, the secondary peak of -4.1 Sv in the total Lagrangian overturning at T = 4.5 ^{o}C is mainly due to the *withinBC* particles. This confirms that the transformation of the *withinBC* particles results in relatively lighter water masses than the *interiorShort* particles. Notably, at this temperature, the Eulerian overturning is negligible. That is, the Eulerian transport of waters of this temperature at the inflow and outflow is the same, while the Lagrangian analysis reveals an increase in transport of this water mass. This implies that an inflow of waters of this temperature exists, which does not reach the outflow within six years and is thus not captured by the Lagrangian backtracking calculation. The temperature of this water mass corresponds to that of boundary current waters at 500-1000 m depth (see Figure 2.1b in chapter 2). We speculate that this water mass is also transported offshore from the boundary current to the interior, but has a residence time longer than the six-year duration of the Lagrangian calculation.

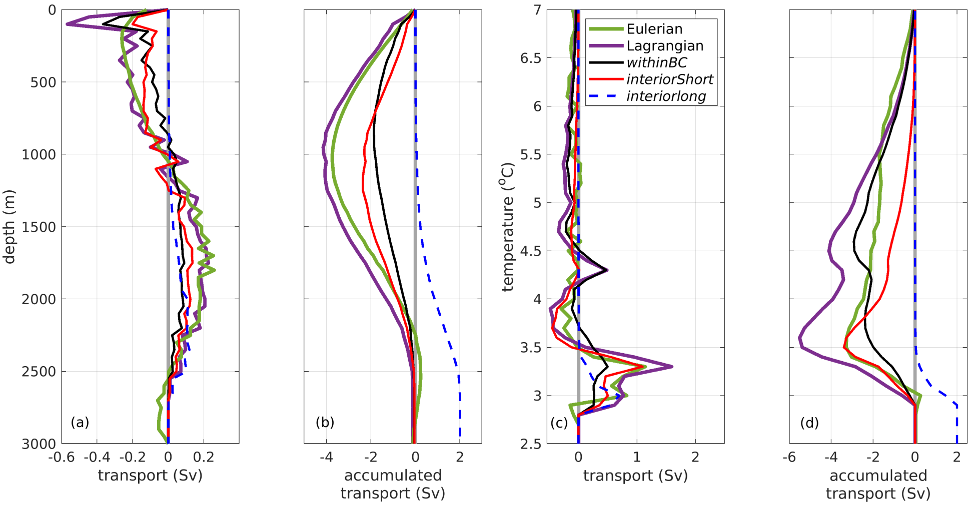

Figure 3.7: Change of the volume transport (in Sv) between the outflow and inflow binned every (a) 50 m in depth and (c) 0.1 ^{o}C in temperature space for the annual mean Eulerian values (green line, mean over year 15; the particle release year), for the *withinBC* (black line), *interiorShort* (red line) particles and their sum (Lagrangian mean, purple line). Accumulated transport in (b) depth (shallow to deep) and (d) temperature (high to low) space. Also shown is the volume transport of the *interiorLong* particles at the outflow (blue dashed line).

3.5. Subduction

As shown in Figure 3.7, both the *withinBC* and the *interiorShort* particles experience water mass transformation. Here, we identify the location where these water masses last change their properties by means of the local subduction rate. Following the analysis of Brandt et al. (2007) we define subduction as the process of a particle leaving the mixed layer. It is calculated from the trajectories of the *withinBC* and *interiorShort* particles as the sum of all transport values assigned to the particles subducted within a certain grid box. The subduction velocity (Figure 3.8) is calculated by dividing this subduction rate of each gridbox by its area. The magnitude of the subduction velocity is similar to the subduction velocities reported by Brandt et al. (2007) with elevated values in the west.

The calculation of the subduction rate is performed separately for the *withinBC* (Figure 3.8a) and *interiorShort* particles (Figure 3.8b). The main difference between the two is the location of the peak values: subduction of waters exiting the domain along the *withinBC* route mainly occurs in the western part of the Labrador Sea. This is likely associated with convection that occurs within the boundary current due to the surface buoyancy forcing. The total subduction of the *withinBC* particles amounts to 1.9 Sv. In contrast, large subduction velocities of the particles following the *interiorShort* route are found in the west, close to the edge of the boundary current. The total subduction for the *interiorShort* amounts to 3.7 Sv, of which 76% occurs in the interior (i.e. offshore of the 18 Sv contour line of Ψ_b). The remaining 24% subducts within the boundary current, after re-entering, which indicates a pathway of transformed water masses within the boundary current (Brandt et al., 2007) similar to the *withinBC* particles. Our study

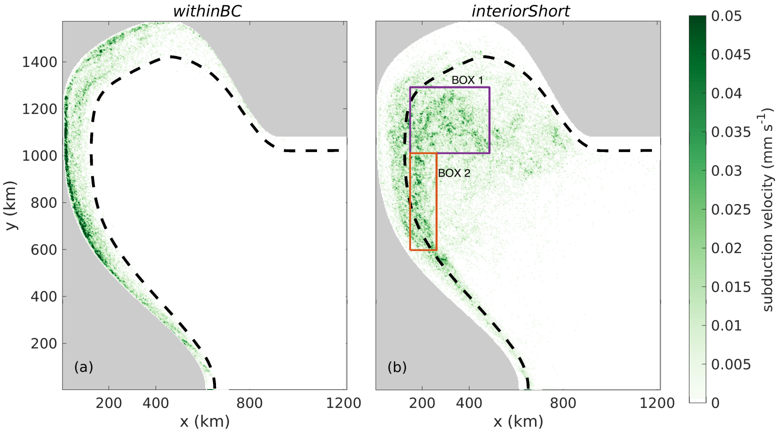

Figure 3.8: Mean subduction velocity for (a) *withinBC* and (b) *interiorShort* particles. The black dashed line shows the 18 Sv barotropic streamfunction that is used to separate the particle pathways. Also included are the boxes in purple (box 1) and orange (box 2) indicating the regions of high subduction velocity that are used in the analysis in section 3.6.

reveals that most of the *interiorShort* particles leave the mixed layer in the interior before they re-entrain into the boundary current and exit the domain (Figure 3.8b). In the following section we will show that the properties of the particles depend on the location where they subduct within the interior (i.e., box 1 and box 2 in Figure 3.8b).

3.6. Lateral exchange and water mass transformation

To explore the lateral exchange between the boundary current and the interior and water mass transformation in the interior, we next focus on the locations where the *interiorShort* particles enter and leave the interior of the domain. We define the first (last) crossing of a particle as the location at which it crosses the 18 Sv contour line of the barotropic streamfunction (Ψ_b) for the first (last) time after entering the domain (purple and yellow stars in the example trajectory shown in Figure 3.2b).

An example trajectory shows that this particle enters the basin at the eastern open boundary at a depth of 100 m (Figure 3.9c); its temperature at the inflow (green square in Figure 3.9a) is $T_{\text{inflow}} = 4.7\ ^{o}\text{C}$. It follows the boundary current until it crosses into the interior (purple star and vertical line in Figure 3.9a and b, respectively). While in the interior, the particle recirculates and shows a large drop in temperature (Figure 3.9b) when it is in the mixed layer (grey shaded area in Figure 3.9b-c). There, it reaches a temperature corresponding to that of the convected water ($T \sim 3.2\ ^{o}\text{C}$, Figure 3.9b). Once the particle is subducted (Figure 3.9c), it stays below the mixed layer in the subsequent winters and no further temperature change occurs (Figure 3.9b). The largest change in depth of the particle (blue line in Figure 3.9c) takes place between locations 5 and 6, when the particle leaves the mixed layer, without any water mass transformation. This means that the particle moves adiabatically along an isopycnal (isotherm) to deeper layers. For most of its advection time, the particle's path is steered by eddies that are present in the interior (Figure 3.9a). After being in the interior for more than 4 years, the particle re-enters the boundary current (yellow star and vertical line in Figure 3.9a-b) and it does so along this 3.2 °C isotherm. After its re-entry, the particle slightly rises in the water column (Figure 3.9c) because the isotherms rise as the boundary current loses heat in the downstream direction (Straneo, 2006a; Georgiou et al., 2019; Brüggemann and Katsman, 2019). Although it takes almost 6 years for this particle to travel from inflow to outflow, only nine months pass between the moment it re-enters the boundary current until it exits the Labrador Sea.

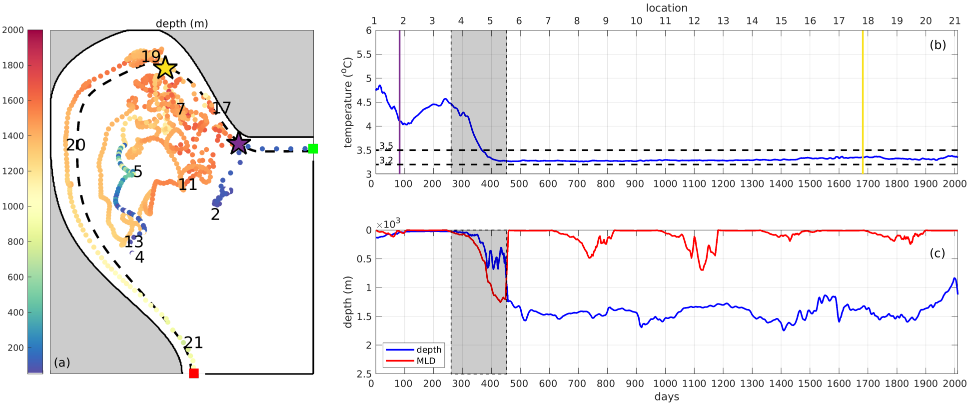

Figure 3.9: (a) Example trajectory of an *interiorShort* particle. The particle's depth at each location is shown in color. Purple (yellow) star denotes the location of the first (last) crossing between boundary current and interior. Numbers correspond to time intervals of 100 days. (b-c) Time evolution of the particle's (b) temperature, (c) depth (blue line) and mixed layer depth at the particle's location (red line). Numbers on the top axis correspond to the location of the particle on the map in (a). The dashed horizontal lines in (b) show the temperature range of the product of convection in this idealized model (i.e. $T = 3.2 - 3.5$ °C) and the purple (yellow) vertical line denotes the moment of the first (last) crossing.

Next, we consider the lateral exchange between the boundary current and interior for all *interiorShort* and *interiorLong* particles. Most particles first cross into the interior at a distance between 380-850 km from the inflow (red dashed line, Figure 3.10a). This peak in first crossings is found upstream of the peak in EKE along the boundary (~700 km downstream from the inflow, blue shading in Figure 3.10a) associated with the eddy activity near the topographic narrowing (Figure 3.1c). This is in agreement with the study of Schulze Chretien and Frajka-Williams (2018), who used Lagrangian trajectories to track the surface freshwater in the Labrador Sea and found that most of the freshwater leaves the shelf in the same area. This indicates that the topography plays a significant role in determining the interior-boundary current exchange: the enhanced EKE, due to enhanced eddy activity along the topographic narrowing (Figure 3.1c and Figure 3.10a) facilitates exchanges between the boundary current and the interior.

Most of the *interiorShort* particles also re-enter the boundary current in the area where EKE is enhanced (500-1000 km from the inflow, Figure 3.10a); a secondary peak of last crossings is seen farther downstream coinciding with a secondary peak in EKE (distance ~2500 km). Similarly, the last crossings of the *interiorLong* particles (blue line in Figure 3.10a) are also mostly found at the region of high EKE.

The average temperature of the particles entering the interior within 1000 km downstream of the inflow is 3.9 ^{o}C (dashed line in Figure 3.10b). Notably, when they re-enter the boundary current, the particles are on average 0.2 ^{o}C colder (solid line). This corroborates that water mass transformation occurs during their time in the interior. At distances greater than 1500 km downstream of the inflow (i.e. the western side of the domain) the exchange occurs almost at the same temperature. This indicates that the boundary current-interior exchange at this part of the domain does not considerably affect the properties of the water masses. It is noteworthy that the *interiorLong* particles have a mean temperature of 3 ^{o}C or lower when they leave the interior (Figure 3.10c), confirming once more that these particles represent the densest water mass in this model of the Labrador Sea.

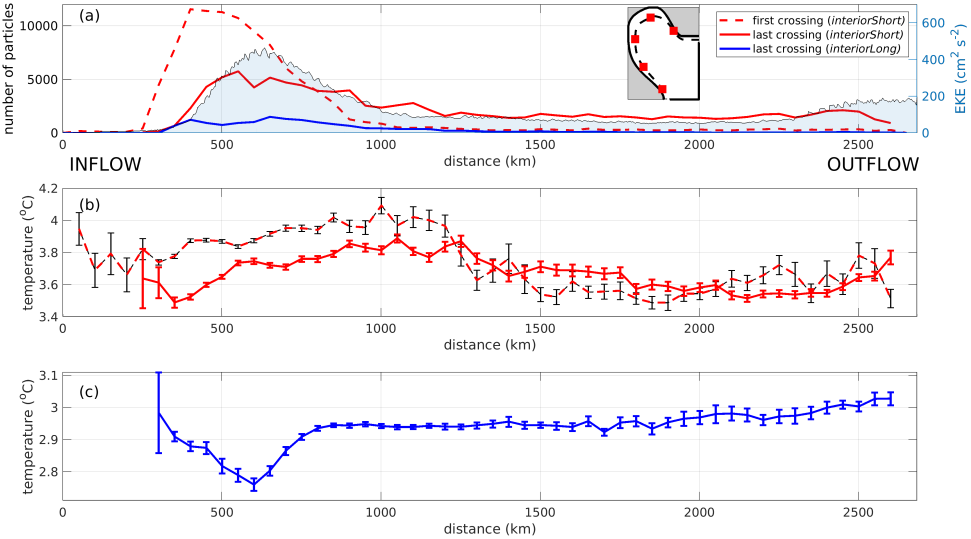

Figure 3.10: (a) Number of particles and (b) mean temperature of particles at the first (dashed line) and last (solid line) crossings for the *interiorShort* particles. (c) As in (b) but for the *interiorLong* particles. Values are binned over segments of 50 km in alongshore direction (see inset, red squares mark distances every 500 km). The blue shaded area in (a) shows the EKE as a function of distance from the inflow. The error bars in (b-c) represent the 95% confidence interval of the mean values.

To explore this connection in more detail, we now focus on the export routes of the water masses that have been subducted in the interior. We define two areas which represent regions of high subduction velocity (Figure 3.8b) in box 1 and box 2, similarly to Brandt et al. (2007), and analyze only the behavior of the particles that subduct in these two boxes. So, the particles used for this analysis represent a fraction of the *interiorShort* particles (i.e. 20% of the particles, which represent 1.6 Sv or 43% of the total subduction in the interior). These boxes are placed in regions characterized by different dynamics: box 1 is located where the deepest mixed layers are found (Figure 3.1b), while box 2 is placed near the Labrador coast where, accordingly to previous studies (e.g., Brandt et al., 2007), the newly-formed LSW is rapidly exported. It appears that the majority of the particles that subduct within box 1 (Figure 3.11a) move towards the high EKE area near the

Greenland coast (distance = 400-800 km) and re-enter the boundary current there before exiting the domain (purple line in Figure 3.11c). In contrast, a large fraction of particles that subduct within box 2 (Figure 3.11b) are directly entrained in the boundary current in the west (between 1600-2100 km, orange line in Figure 3.11c). However, the number of particles subducted in box 2 is smaller than the number that subducts in box 1 (i.e. 5643 particles difference that amounts to 0.5 Sv in terms of volume transport). This again explains the importance of the indirect export route via the West Greenland coast.

It is clear that the particles that subduct in box 1 and re-enter the boundary current where EKE peaks (distance between 400-1000 km) show a larger temperature change than the ones that subduct in box 2: they experience a mean cooling of $\Delta T_{box1}(_{400-1000\ km})$=-0.5 ^{o}C in contrast to $\Delta T_{box2}(_{400-1000\ km}) = -0.2\ ^{o}C$ (Figure 3.11d). This is due to the fact that the water masses subducted in these two boxes originate from different regions (Figure 3.1b). In box 1, the mixed layer is deeper and temperatures are lower than in box 2. Essentially, Figure 3.10b and Figure 3.11d support the view that most of the *interior-Short* particles are transformed during their time in the interior. Moreover, depending on where water mass transformation occurs the particles tend to follow a different path and hence it is expected that they will display different residence times.

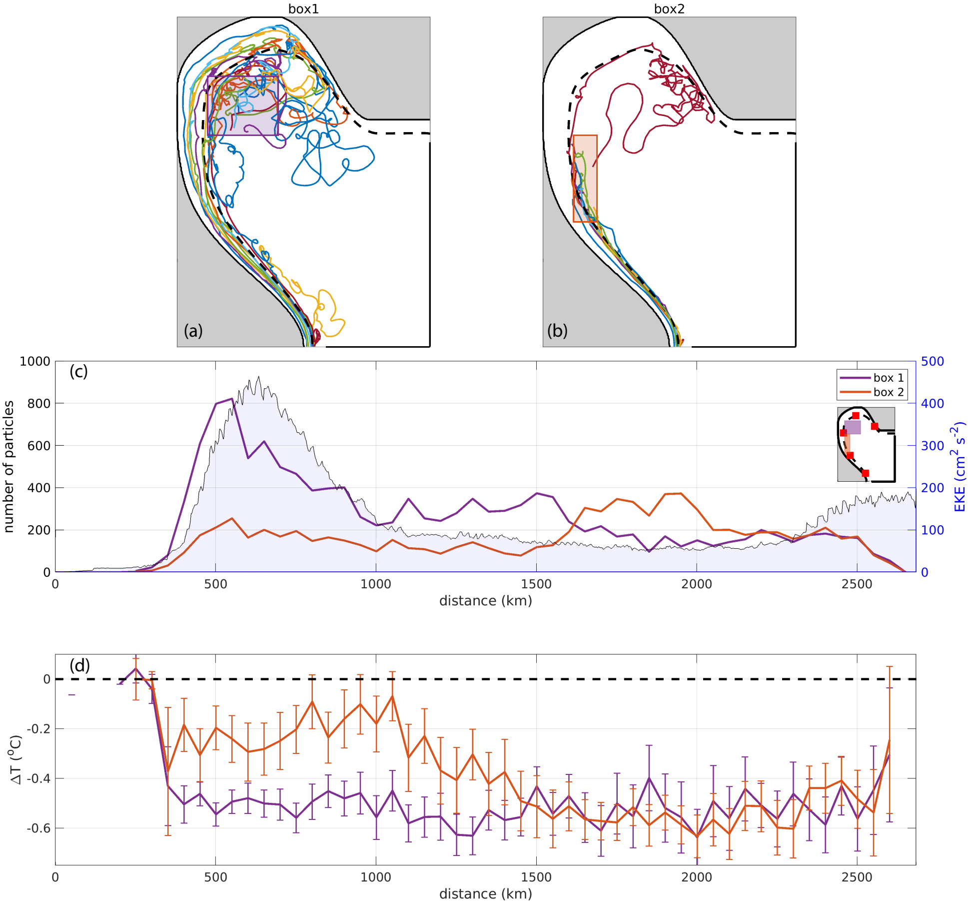

Figure 3.11: Example trajectories from the location where the particles subduct in (a) box 1 (purple rectangle) and (b) box 2 (orange rectangle) to the outflow. (c) Number of particles that cross the 18Sv contour for the last time and (d) mean temperature change (at the location of the last crossing) between the last and first crossing ($\Delta T = T_{\text{last}} - T_{\text{first}}$) as a function of distance from the inflow for the particles that subduct within box 1 (purple line) and box 2 (orange line). Values in (d) are binned over segments of 50 km in alongshore direction at the location of last crossing. The shaded area in (c) shows the EKE as a function of distance from the inflow (see inset, red squares mark distances every 500 km).

3.7. Residence time and export timescale

In this section, the residence time and export timescale of the particles are studied for each pathway. First, we investigate the residence time of the particles, defined as the time it takes a particle to travel from the inflow to the outflow. We focus on the *wholeLoop* particles, i.e. *withinBC* and *interiorShort* (Figure 3.3), which all leave the basin within 6 years. It is clear that 90% of the *withinBC* particles leave the basin within one year (black bars in Figure 3.12a); their maximum residence time is less than 2 years (black line in Figure 3.12b). This highlights the existence of a fast route of water masses that enter the Labrador Sea and travel within the boundary current. As expected based on Figure 3.9b, the *interiorShort* particles display much longer residence times of up to 6 years (Figure 3.12a-b). However, 60% of the particles still leave the basin within 2 years (red line in Figure 3.12b).

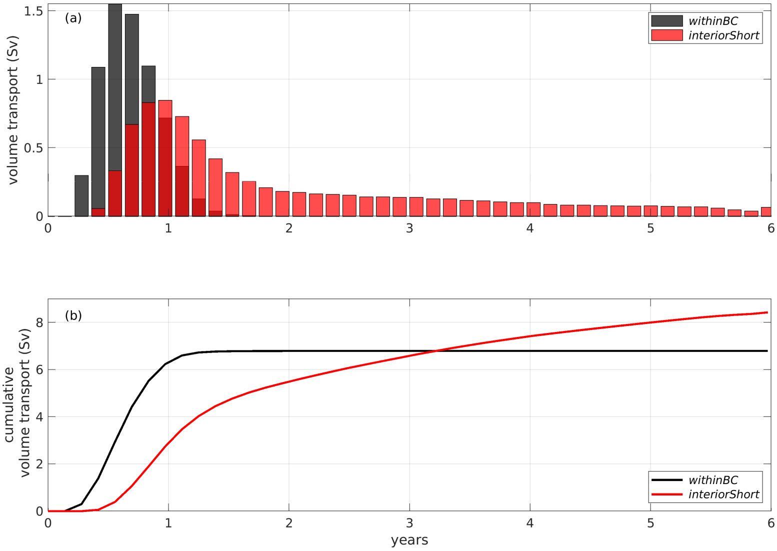

Figure 3.12: (a) Volume transport and (b) cumulative volume transport of the *withinBC* (black bars/lines) and *interiorShort* (red bars/lines) particles, both as a function to their residence time (binned every 50 days) within the model domain.

Next, we investigate if there is any connection between the properties of the water masses that exit the domain and their residence time in the basin by displaying the temperature of the particles at the outflow as a function of their residence time (Figure 3.13). From this, it is evident that most of the *withinBC* particles (i.e. 60% of the particles, Figure 3.13a) that leave the domain within one year correspond to lighter water masses (T> 3.8 ^{o}C). The residence time of the particles that exit the domain with temperatures lower than 3.8 ^{o}C is slightly longer but restricted to a maximum of 2 years. Here, the impact of the surface heat loss along the boundary in determining the properties of the local water mass is visible: the particles with T< 3.8 ^{o}C likely represent water masses formed during convection within the boundary current (Figure 3.8a). Note that these particles are found deeper in the boundary current where its speed is weaker (Figure 3.4), thus explaining their longer residence time. For the *interiorShort* particles the picture is different; 74% of the particles exits the domain with temperatures below 3.8 ^{o}C (Figure 3.13b). Remarkably, the *interiorShort* particles that leave the basin within one year are particles that stay in the interior shortly and are warmer (i.e. $\bar{\mathrm{T}}_{\mathrm{residence<1year}}$= 4 ^{o}C). That is, the water masses that stay in the interior longer get denser (i.e. $\bar{\mathrm{T}}_{\mathrm{residence>1year}}$= 3.6 ^{o}C).

Besides the residence time, we also calculated the export timescale, defined as the time it takes a particle to reach the outflow after it has subducted. As expected, the export time for the *withinBC* particles is very short: for 95% of the particles it is less than half a year. The export time of the *interiorShort* particles ranges from 4 days to 5.5 years. It appears that the water masses that are subducted within box 1 generally take more than one year before they exit the Labrador Sea; only 35% of the total transport carried by these particles is exported within one year. This is explained by the fact that the majority of these particles first moves towards the high EKE area near the Greenland coast before they re-enter the boundary current and reach the outflow (Figure 3.11a). In contrast, the *interiorShort* particles that subduct in box 2 and are entrained into the boundary current in the west (Figure 3.11b) exit the domain much quicker; 80% of the total transport carried by these particles is exported out of the Labrador Sea within 150 days.

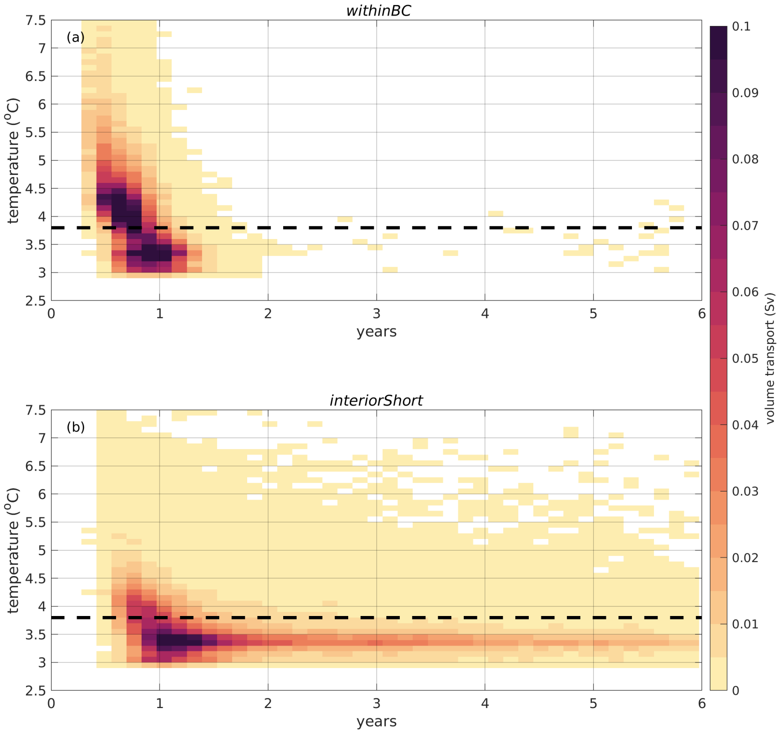

Figure 3.13: Density distribution (in terms of volume transport) of the particle temperature at the outflow compared to the particle residence time for the particles that reach the outflow (*wholeLoop*) while (a) staying within the boundary current (*withinBC* particles) and (b) passing through the interior (*interiorShort* particles). The particle density is shown per $\Delta T = 0.1\ ^{o}$C and $\Delta t = 50$ days interval. The black dashed horizontal line shows the 3.8 ^{o}C isotherm.

3.8. Discussion and conclusions

In this study, the upstream pathways of the water masses exiting the Labrador Sea have been investigated from a Lagrangian perspective, with a focus on the exchange between the boundary current and the interior and the water mass transformation that occurs within the domain. To this end, the output of a regional idealized model is used. This model is known to capture the mesoscale eddy activity in the Labrador Sea, which is most prominent at the West Greenland coast (section 2.3.1). The use of such an idealized model facilitates the exploration of the dynamics of this exchange between the boundary current and the interior and its role for LSW export. In this study, we extend the more generic study of a highly idealized marginal sea by Brüggemann and Katsman (2019), by quantifying the role of the interior-boundary exchanges in setting the properties and the associated timescales of the water masses exiting the marginal sea in more detail.

By assessing the processes from a Lagrangian viewpoint, we show that water masses follow either a direct route within the boundary current (*withinBC* particles) or an indirect route that involves boundary current-interior exchanges (*interiorShort* and *inte-*

riorLong particles) from the inflow region south of Greenland to the outflow region on the Labrador side (Figure 3.2b) that carry roughly the same transport. The distribution of the particles at the inflow and outflow (Figure 3.4) shows that their position at the inflow determines their pathway and location at the outflow. Essentially, the particles that follow the boundary current (*withinBC*) are found in the core of the boundary current with rather high velocities, while particles that pass through the interior (*interiorShort*) are found on its outer flank. That is, our results indicate that the fate of water masses is already determined upstream. This suggests that processes in the Irminger Basin and Nordic Seas impact the water mass transformation in the Labrador Sea.

Building on the generic idea proposed by Brüggemann and Katsman (2019) on the existence of a fast and a slow route for dense water masses that exit the Labrador Sea, the Lagrangian analysis presented in this study allows us to quantify the transports associated with those two pathways. The depth change of the particles between the inflow and outflow reveals that the total volume transport between 1500 - 3000 m increases by 1.3 Sv for the *withinBC* particles and by 2.0 Sv for the *interiorShort* particles (Figure 3.5). In density space (which in this idealized model is represented by temperature only), the Lagrangian trajectories also show a substantial transport change between the inflow and outflow through the 3.5 ^{o}C isotherm which amounts to 2.2 Sv and 3.2 Sv for the *withinBC* and *interiorShort* particles, respectively (Figure 3.6). The maximum overturning derived from the Eulerian quantities amounts to -3.8 Sv at 1000 m (depth space, Figure 3.7b) and -3.4 Sv at 3.5 ^{o}C (density space, Figure 3.7d). The Lagrangian particles capture the net Eulerian overturning observed in this model both in depth and density space well (Figure 3.7), considering the fact that not all the particle trajectories cover the entire path between in- and outflow. The relative importance of the different pathways on the overturning becomes apparent in density space; 60% of the maximum overturning is related to the transport carried by the *interiorShort* particles and only 40% by the *withinBC* particles (Figure 3.7c-d). However, there is also a significant signal in the overturning in lighter layers, which is only related to the relatively slow moving fraction of the *withinBC* particles. In short, the volume transport of the densest water masses is primarily carried by particles that have resided in the interior (i.e. *interiorShort* and *interiorLong* particles), while the particles that follow the fast route (i.e. *withinBC*) mainly transform in lighter water masses.

The characteristics of water mass transformation also differ for the fast and slow pathways. The *withinBC* particles mainly subduct on the southwest side of the Labrador Sea (Figure 3.8a). This location is downstream of the region where strong surface heat loss has reduced the stratification of the boundary current, allowing the water masses to be transformed into denser water masses. In contrast, the *interiorShort* particles generally enter the interior at the Greenland side (Figure 3.10a), experience water mass transformation in the interior at the convection region (Figure 3.8b and Figure 3.10b), before re-entering the boundary current (Figure 3.10). The latter occurs predominantly on the Greenland side and to a lesser extent on the Labrador side (Figure 3.10a), depending on the location where the particle last leaves the mixed layer (Figure 3.11). This two-way exchange (first and last crossings) at the western coast of Greenland has been also identified in the recent study of Pennelly et al. (2019). However, our study highlights that the export of the water masses that have been transformed into denser water masses in the interior occurs laterally, as they are advected towards the region of high EKE on the Greenland side by eddy stirring.

The exchange between the boundary current and the interior has a direct impact on the timescales of the export of the water masses (Figure 3.13): 90% of the volume transport carried by the *withinBC* particles exits the basin within one year, while only 30% of the transport associated with the *interiorShort* particles exits within that time frame. In observations (Bower et al., 2009) and models (Brandt et al., 2007; Feucher et al., 2019) the newly formed LSW is exported within one year. Our Lagrangian analysis supports the idea of previous observational studies that the quickly exported LSW is likely formed within or close to the boundary current (Pickart et al., 2002; Cuny et al., 2005). Most of the *interiorLong* particles also re-enter the boundary current at the region of high EKE (Figure 3.10c). However, due to topographic constraints the lateral, along isopycnal transport towards the boundary current at the high EKE region cannot as easily take place for the denser *interiorLong* as for the lighter *interiorShort* particles. This results in a longer residence of the *interiorLong* particles within the interior. Essentially, the fact that the densest water masses, which are represented by the *interiorLong* particles, take more than six years to fully pass through the Labrador Sea, confirms that cold signals that are exported from the Labrador Sea do not need to correspond to recent convective events, as suggested by Cuny et al. (2005). Thus, our results suggest that the observed year-to-year correspondence between the properties of the water masses found in the interior of the Labrador Sea and in the Labrador Current (e.g., Rhein et al., 2015; Yashayaev and Loder, 2017; Holte and Straneo, 2017; Le Bras et al., 2017) reflect variations of the fast export route of LSW formed close to or within the boundary current.

Our Lagrangian results clearly extend the tracer analysis performed in chapter 2 and Brüggemann and Katsman (2019), as these studies mostly provided a qualitative description of the connection between strong eddy activity and convection areas. The Lagrangian analysis using particles instead of a passive tracer allows for conditional analysis (see van Sebille et al., 2018) and provides a quantification of the relative importance of each pathway to water mass transformation and to the overturning in depth and density space.

In our study, the limited model domain does not allow the investigation of the export route towards the Irminger Sea discussed in section 3.1 (e.g., Lavender et al., 2000; Pickart et al., 2003). Therefore, our results may overestimate the transport of the LSW towards the West Greenland coast. Another aspect that can not be covered in our idealized model simulation but deserves attention is the suggestion by Lozier et al. (2013) that the overflow waters entering the subpolar gyre from the Nordic Seas also follow interior pathways that substantially lead to their equatorward export through the Labrador Sea. We expect a minimal transformation of the overflow waters within the Labrador Sea since they fill the deeper layers of the basin. However, the presence of the overflow waters may affect the LSW pathways. Nevertheless, the conclusion that an eddy driven transport of dense water towards the boundary exists and that it affects the export timescales of LSW is expected to hold. Analyses with a more realistic high-resolution model are needed to explore this in more detail.

One of the main findings of this chapter is that there is a fast, direct route for relatively lighter water masses compared to the slower, indirect route that the denser water masses follow to exit the Labrador Sea. In this model, both routes carry roughly the same transport, but the indirect route is steered by the eddy activity near the Greenland coast. That is, a preferable region for lateral spreading of LSW and entrainment in the boundary current is identified. Therefore, the view of a homogeneous lateral spreading and entrainment of the LSW into the boundary current is not valid in our model, and this is consistent with the studies of Bower et al. (2009, 2011) and Gary et al. (2012). Importantly, the fact that the densest water masses found in this study take more than six years to exit the Labrador Sea might obscure the link between the LSW formation and AMOC variability in observations such as the OSNAP array (Holliday et al., 2018; Lozier et al., 2019).

The result that the interior-boundary current exchange is important for the LSW export and hence contributes to the AMOC variability, suggests that additional observations aimed at capturing these mechanisms are needed. It also raises the question how well LSW export processes, their variability and their relation to AMOC variability are represented in climate models, which lack the resolution to resolve the mesoscale features required to capture this interior-boundary current exchange.

Chapter 4

Direct and indirect pathways of convected water masses and their impacts on the overturning dynamics of the Labrador Sea

The dense waters formed by wintertime convection in the Labrador Sea play a key role in setting the properties of the deep Atlantic Ocean. To understand how variability in their production might affect the Atlantic Meridional Overturning Circulation (AMOC) variability, it is essential to determine pathways and associated timescales of their export. In this study, we analyze the trajectories of Argo floats and of Lagrangian particles launched at 53^o N in the boundary current and traced backwards in time in a high-resolution model, to identify and quantify the importance of upstream pathways. We find that 85% of the transport carried by the particles at 53^o N originates from Cape Farewell, and it is split between a direct route that follows the boundary current and an indirect route involving boundary-interior exchanges. Although both routes contribute roughly equally to the maximum overturning, the indirect route governs its signal in denser layers. This indirect route has two branches: part of the convected water is exported rapidly on the Labrador side of the basin, and part follows a longer route towards Greenland and is then carried with the boundary current. Export timescales of these two branches typically differ by 2.5 years. This study thus shows that boundary-interior exchanges are important for the pathways and the properties of water masses arriving at 53^o N. It reveals a complex three-dimensional view of the convected water export, with implications for the arrival time of signals of variability therein at 53^o N and thus for our understanding of the AMOC.

This chapter has been published in *Journal of Geophysical Research: Oceans* (2021).

4.1. Introduction

The subpolar North Atlantic (SPNA) is a region of high importance for the global climate (e.g., Schott and Brandt, 2007; Buckley and Marshall, 2016; Lozier et al., 2019) and in particular for the Atlantic Meridional Overturning Circulation (AMOC). There, the conversion of the relatively warm and salty waters flowing northward in the North Atlantic Current (NAC, upper AMOC limb) to cold and slightly fresher North Atlantic Deep Water (NADW, lower AMOC limb) takes place. The NADW is a combination of the Labrador Sea Water (LSW) and the dense overflow waters originating from the Nordic Seas (Talley et al., 2011). During wintertime, the heat loss from the ocean to the atmosphere together with the weak stratification below the mixed layer facilitates the process of convection at certain locations in the SPNA. Traditionally, the LSW was considered the product of deep convection that takes place in the central Labrador Sea (Talley and McCartney, 1982; Marshall and Schott, 1999). However, more recent studies revealed that deep convection also occurs in the southern Irminger Sea and that this results in a water mass with similar properties to LSW (Pickart et al., 2003; Våge et al., 2008; de Jong et al., 2012; Piron et al., 2016; Le Bras et al., 2020).

Previous numerical model studies suggested a strong connection between LSW production and AMOC variability (e.g., Kuhlbrodt et al., 2007; Biastoch et al., 2008; Rahmstorf et al., 2015). However, recent observational studies have cast doubts on the importance of LSW production for the AMOC and pointed out a stronger connection with water mass transformation in the eastern part of the SPNA instead (Li and Lozier, 2018; Lozier et al., 2019; Zou et al., 2020). Consequently, the connection between the LSW production and the variability of the AMOC is under renewed debate.

One of the key elements in understanding a potential connection between LSW formation and the AMOC is to clarify the relative importance of all possible export pathways of LSW and the associated timescales. Although the processes that govern the conversion of lighter to denser water masses and the locations where this occurs have been extensively researched in numerical and observational studies (e.g., Marshall and Schott, 1999; Spall and Pickart, 2001; Pickart and Spall, 2007; Våge et al., 2008), the processes that govern the export routes of dense water masses are less well understood.

LSW pathways are the subject of numerous observational and numerical studies (e.g., Talley and McCartney, 1982; Straneo et al., 2003; Palter et al., 2008; Bower et al., 2009; Brandt et al., 2007; Rhein et al., 2017) and the fact that multiple pathways have been identified illustrates the complex nature of the LSW spreading. The LSW mainly follows the Deep Western Boundary Current (DWBC) and spreads equatorward along the western boundary of the North Atlantic (Talley and McCartney, 1982; Stramma et al., 2004; Le Bras et al., 2017; Handmann et al., 2018). In the Newfoundland Basin, the presence of significant exchange between the DWBC and the interior causes the DWBC to bifurcate from its equatorward flow, thus resulting in interior pathways of LSW in the SPNA (e.g., Bower et al., 2009; Spence et al., 2012; Solodoch et al., 2020). The main pathways that newly-formed LSW follows prior to entering the DWBC have also been identified. Within the Labrador Sea itself, LSW may be rapidly exported by spreading laterally near the Labrador coast, directly formed in the boundary current as a result of convection within the boundary current itself (e.g., Brandt et al., 2007), or first travel from the interior towards the west coast of Greenland and then follow the boundary current (e.g., Palter et al., 2008; Georgiou et al., 2020). Moreover, the LSW may travel northeastward towards the Irminger Sea (e.g., Pickart et al., 2003; Bower et al., 2009), possibly carried by mid-depth recirculation cells (e.g., Lavender et al., 2000).

However, the processes that govern the transport along these various export routes of dense water masses formed in the Labrador Sea have yet to be clarified; in particular, quantification of the magnitude of the transports, the typical water mass properties and travel times associated with each pathway is still lacking. It is expected that the arrival of a LSW signal at the locations of the OSNAP array (north of 52^oN; Lozier et al., 2019) and RAPID-MOCHA array (at 26.5^oN; Smeed et al., 2018) will differ depending on the pathway that LSW follows. The idealized study presented in chapter 3 indicates that this is indeed the case, but the idealizations did not allow for a reliable quantification of timescales. This complexity clearly makes it difficult to capture a potential link between formation rates of dense waters and AMOC variability further downstream.

In this study, we analyze the upstream pathways of all water masses exiting the Labrador Sea at 53^oN revealed by Lagrangian particle tracking, using the model output from a state-of-the-art global ocean-sea ice model. Our approach and analyses strongly build on the highly idealized model study presented in chapter 3 in which qualitative insights were gained. The use of output from a realistic simulation introduces among others more realistic atmospheric forcing, more realistic bathymetry, the effects of salinity, potential connections between the sub-basins of the SPNA and the presence of overflow waters and allows us to characterize the transports and water mass transformation along pathways quantitatively. In addition, we analyze the trajectories of available Argo floats to identify pathways and associated time scales of deeper water masses within the Labrador Sea from observations.

The Argo float data, the global ocean-sea ice model simulation and the Lagrangian particle tracking approach are introduced in section 4.2. The upstream pathways of the water masses found at 53^oN from the Argo float trajectories and the trajectories from the high-resolution model are analyzed in section 4.3. The subduction location of the particles, the properties they consequently acquire and the pathways that follow after being subducted are explored in section 4.4. In section 4.4, we also investigate the relative importance of each pathway on the overturning in the Labrador Sea. Furthermore, the travel times of particles along the various pathways are addressed in section 4.5. Finally, a discussion on the three dimensional view of the export of convected waters is provided in section 4.6, followed by the summary and conclusions of our results (section 4.7).

4.2. Data and Methods

To establish the possible upstream pathways for LSW within the subpolar gyre we first use the trajectories derived from available Argo floats (section 4.2.1). The limited number and lifetime of the Argo floats prohibits the quantification of transports along each of these pathways. In addition, their isobaric drift does not allow the investigation of the water mass transformation occurring along the various pathways or the vertical displacement of the water masses. Therefore, a Lagrangian study using the output of a realistic global ocean model is performed. The model data and the Lagrangian approach are introduced in section 4.2.2 and section 4.2.3.

4.2.1. Argo float data

The data used in this study are obtained from the International Argo Program (downloaded on May 15, 2020 from https://coriolis.eu.org, Argo, 2020). The floats are designed to drift at approximate pressures of 1000 db, 1500 db or 2000 db for 10 days. Then, each float descends to 2000 db and then collects profiles of the water column as it rises to the surface where it remains only shortly to communicate with the Argos satellite system (Roemmich et al., 2009). Once the float has transmitted its data it descends again to its designated drifting depth. The Argo float then repeats this cycle, usually with a 10-day period. We select only those floats that at some moment are found in the subpolar gyre and exit the Labrador Sea via the boundary current at 53^{o}N and onshore of the 3000 m isobath. This procedures selects 97 floats; all trajectories are mapped in Figure 4.1 and are analyzed further in section 4.3.1.

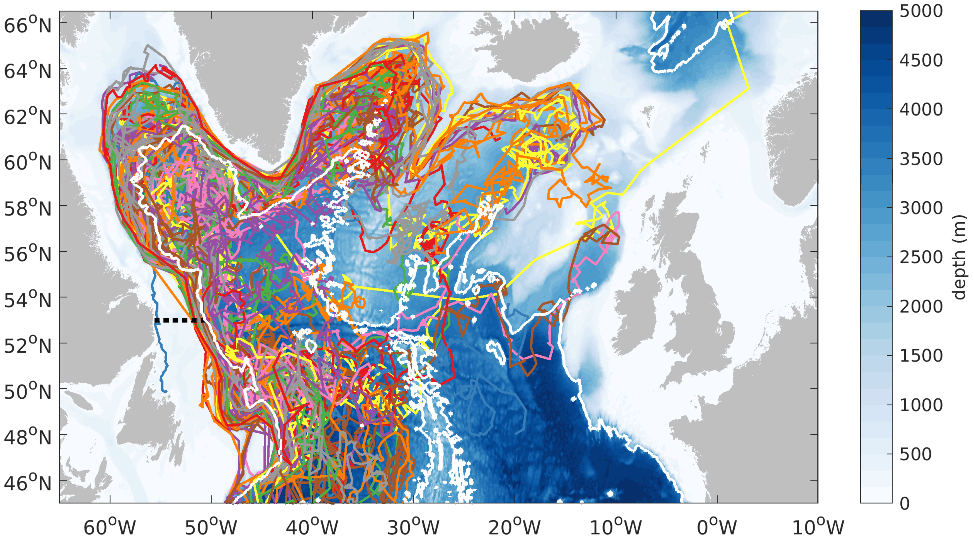

Figure 4.1: Trajectories of 97 Argo floats that drift in the subpolar gyre and exit the Labrador Sea via the boundary current (onshore of the 3000 m isobath at 53^{o}N, black dotted line). The 3000 m isobath is highlighted (white contour, bathymetry data from ETOPO1(Amante and Eakins, 2009)).

4.2.2. Ocean circulation model: MOM

We use the output data from the Modular Ocean Model global ocean-sea ice model (MOM), to advect the Lagrangian particles. For a more detailed description of its configuration we refer to Spence et al. (2017). MOM uses a tripolar B-grid with a horizontal resolution of 0.1^o (which corresponds to ~ 5.5 km at 60^{o}N) and 50 vertical layers with a resolution of 5 m at the surface up to 200 m near the bottom. The model is forced with 6-hourly COREv2-NYF (Griffies et al., 2009; Large and Yeager, 2009) atmospheric forcing and the associated bulk formulations, in particular the Normal Year Forcing derived from the interannual varying atmospheric state from 1958 to 2000. Moreover, the model is coupled to the GFDL Sea Ice Simulator model, which allows the sea ice to freely evolve. In addition, a restoring condition with a timescale of 60 days is applied to the surface salinity.

Vertical mixing (and in particular the process of convection) is parameterized by the KPP parameterization (Large et al., 1994), while biharmonic viscosity and diffusion are applied in the horizontal. The ratio of the baroclinic radius of deformation to a model's grid spacing is commonly used as a measure for the ability of the model to resolve the mesoscale activity (Hallberg, 2013). Within the subpolar North Atlantic the Rossby radius is ~ 10 km (Smith et al., 2000; Funk et al., 2009), thus the horizontal resolution of MOM is only partly eddy-resolving in this region.

Ypma et al. (2019) found that this MOM simulation generally shows a good agreement with the observed hydrography in the Nordic Seas. Here, we shortly discuss the hydrography, the mixed layer depth and eddy kinetic energy in the subpolar North Atlantic Ocean derived from the annual mean 3D velocity, potential temperature and salinity fields. The analysis is performed on model data obtained following a 70-year-long control state simulation in this high resolution.

Following Talley and McCartney (1982), we define LSW as the water mass for which the potential vorticity (PV) is PV<4 x10^{-12} m^{-1} s^{-1}, which in this MOM simulation corresponds to the density range σ=27.75- 27.83 kg m^{-3}. The overflow water is defined as σ >27.83 kg m^{-3} (Figure 4.2b-c). The densities of LSW and overflow waters thus display a small positive bias compared to densities typically assigned to LSW (σ=27.70- 27.80 kg m^{-3}) and overflow water (σ >27.80 kg m^{-3}) in observational studies (e.g., Holliday et al., 2018). Such small biases in the simulated hydrography of the Labrador Sea in the MOM simulation are comparable to what is seen in other high-resolution model studies (e.g., Zou and Lozier, 2016). In the presented analysis, we identify LSW based on this model-based density range deduced from the model.

To characterize the main currents in the SPNA we first calculate the depth-integrated transports, and next assess the cumulative transport from the Labrador coast towards Scotland. We use the local minima and maxima of this cumulative transport to define the horizontal extent of each current (marked by orange vertical lines in Figure 4.2d). The corresponding transport for each major current obtained in this way (Table 4.1) compares well to the observed values (Holliday et al., 2018). Moreover, we calculated the overturning in density space as from the MOM data along the approximate OSNAP section, following the methodology described in Zou et al. (2020) (Figure 4.2e). The modelled overturning strength compares well to the observed values, both over the full section and along the OSNAP-WEST and OSNAP-EAST sections (Table 4.2).

The location and depth of convection is analyzed from the winter (January-March, JFM) mean mixed layer depth (MLD_{JFM}), defined from a density difference criterion: an increase of $\Delta\sigma$=0.01 kg m^{-3} with respect to the surface value (Brandt et al., 2007; Paquin et al., 2016; MacGilchrist et al., 2020). In MOM, convection reaches a depth of 1400 m in the central Labrador Sea (Figure 4.3a). The largest values are found in the southwest, away from the locations where the heat loss (black contour in Figure 4.3a) and mesoscale eddy activity (shading in Figure 4.3b) peak. Overall, the location and the depth of the

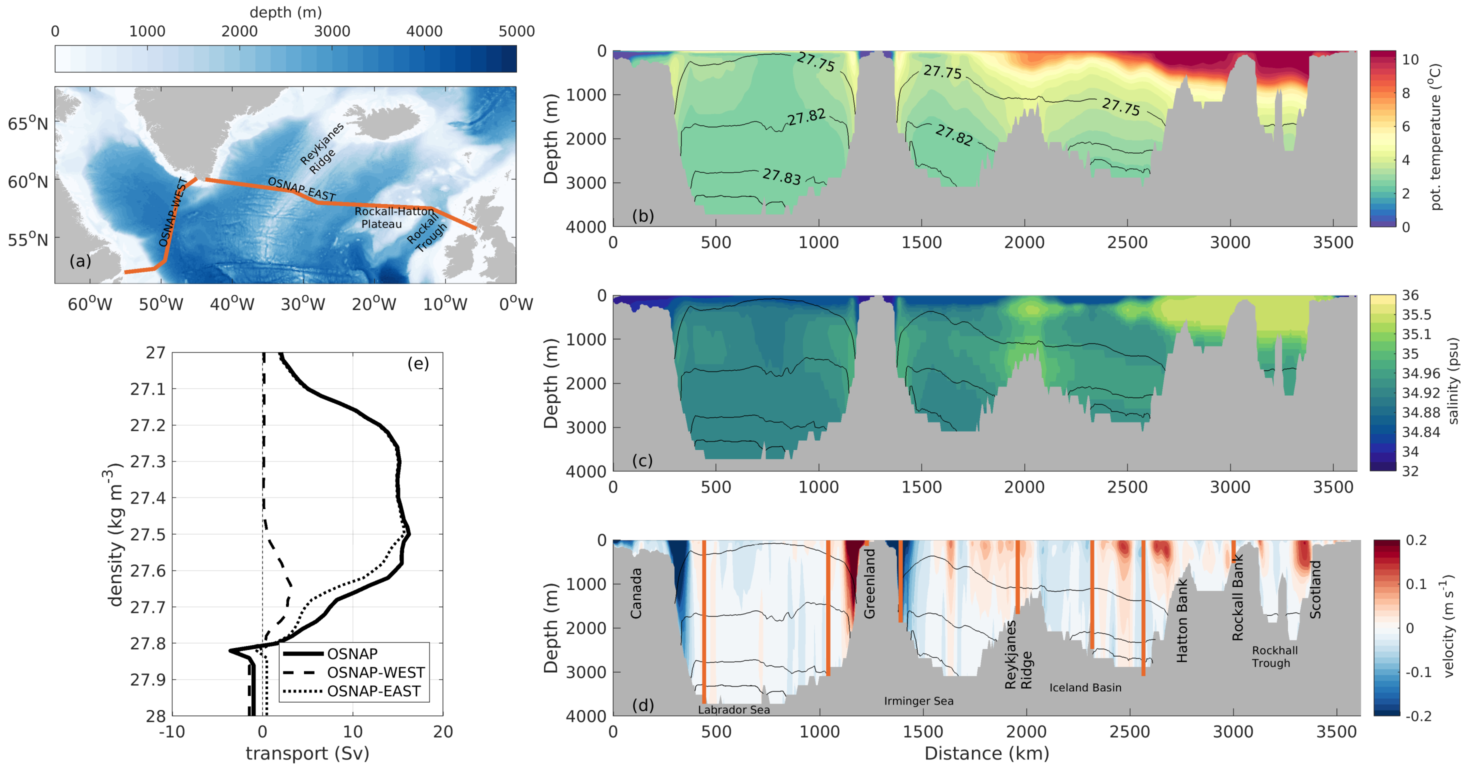

Figure 4.2: (a) Bathymetry and the location of the OSNAP array as defined in MOM, which consists of the OSNAP-WEST and OSNAP-EAST sections. Annual mean (b) potential temperature (in ^{o}C), (c) salinity and (d) velocity orthogonal to the OSNAP array, which is marked by the orange line in (a). The separation of the main currents in the SPNA is obtained by the local minima and maxima of the cumulative depth-integrated transport from west to east and it is marked by the vertical orange lines. Black contours in (b-d) indicate the annual mean potential densities (in kg m^{-3}). (e) Annual mean overturning in density space across the full OSNAP section (solid lines), OSNAP-WEST (dashed line) and OSNAP-EAST (dotted line) as derived from MOM following the method described in Zou et al. (2020).

Table 4.1: Mean transport (in Sv) along the OSNAP array (orange line in Figure 4.2a) estimated from the data obtained in June-July 2014/ May-August 2016 Holliday et al. (2018) and MOM at each section defined by the vertical lines in Figure 4.2d. All values are in Sv (1 Sv = 10^6 m^3 s^{-1}).

section	observations	MOM
Labrador Current	-41.8/-30.8	-31.0
Labrador Sea interior	1.9/5.7	0.8
West Greenland Current	38.4/23.5	21.2
East Greenland Current	-27.0/-23.5	-31.3
Irminger Current	13.6/12.0	23.2
West Iceland Basin	-16.0/-10.8	-7.3
Central Iceland Basin	12.7/17.8	8.1
East Iceland Basin	8.7/8.1	12.1
Rockall Trough	8.7/-2.8	6.0

Table 4.2: Maximum of the annual mean overturning in density space across the full OSNAP section, OSNAP-WEST and OSNAP-EAST (in Sv) and potential density values at which this occurs. Values reported from observations along the OSNAP array from Lozier et al. (2019) are provided for comparison.

section	MOM		observations	
	(Sv)	(kg m^{-3})	(Sv)	(kg m^{-3})
OSNAP array	16.2	27.50	14.9	27.66
OSNAP-EAST	15.7	27.50	15.6	27.53
OSNAP-WEST	3.2	27.66	3.3	27.70

convection region in the Labrador Sea agree well with observations (Pickart et al., 2002; Våge et al., 2009). The surface eddy kinetic energy (EKE, Figure 4.3b) displays maximum values near the West Greenland continental slope and reduces offshore in a tongue-like pattern similarly to studies that derive EKE from altimetry (e.g., Prater, 2002; Lilly et al., 2003).

To summarize, the hydrography and currents simulated in MOM represent the observations well, which makes it a suitable tool for our study. In particular, the representation of the deep convection, the properties of the water masses and the key features of the eddy field are in good agreement with observations.

4.2.3. Lagrangian particle tracking

To investigate the possible upstream pathways and the origins of the water masses that exit the Labrador Sea via the western boundary current, numerical particles are released along a zonal transect at 53^oN extending from the coast until the 3000 m isobath (dotted line in Figure 4.5) and advected backwards in time using the Connectivity Modeling System (CMS, Paris et al., 2013). We selected to release the Lagrangian particles at 53^oN because it is a location that is commonly thought of as the exit of the Labrador Sea, but also because it is a region where continuous measurements of the DWBC take place (e.g., Fischer et al., 2010). In addition, releasing particles south of 53^oN (around Flemish Cap) would need a longer simulation time to account for the interior pathways discussed in

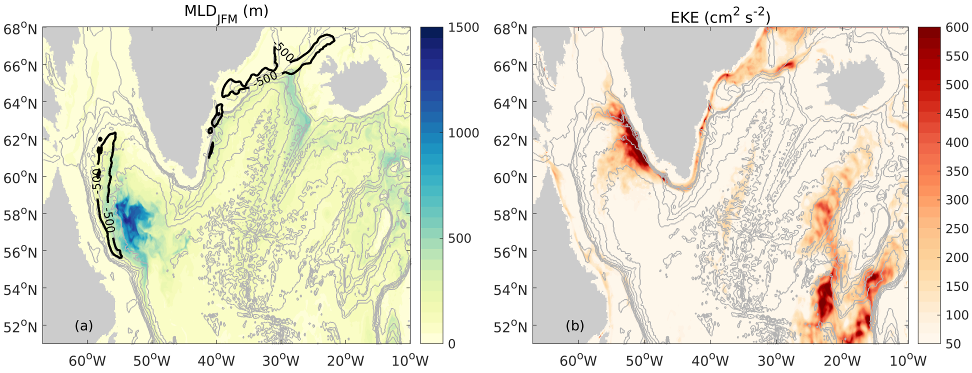

Figure 4.3: (a) Mean winter mixed layer depth (shading) superimposed on the contour of the -500 W m^{-2} mean heat flux and (b) mean eddy kinetic energy (EKE, cm^2 s^{-2}) in the subpolar North Atlantic. Grey contours outline the bathymetry, the contour interval is 500 m starting from the isobath of 500 m.

section 4.1 (Bower et al., 2009; Spence et al., 2012; Solodoch et al., 2020). The particles are advected for six years using the 5-day mean 3D velocity field of MOM. Since a normal year-forcing is applied to MOM, year-to-year variability in velocities is expected to be small. Therefore, we use only one year of model data that is representative of its Eulerian mean state and repeat this as input for CMS for simplicity.

The particles are released at a resolution of 0.1^o in longitude and 50 m in the vertical, only when the meridional velocity is southward at these locations. A volume transport is assigned to each particle, defined by multiplying the meridional velocity in the grid box in which the particle is released by the area of the grid box (Döös, 1995). The transport carried by each particle remains constant throughout its trajectory (van Sebille et al., 2018). Particles are released daily, for a period of one year. All transport calculations are done by adding the volume transport carried by all particles divided by the number of release days. In total, 839002 particles are launched, representing a total annual mean transport of 25.3 Sv.

The particles are advected with a timestep of 1 hour within the 3D velocity field of MOM. CMS uses a tricubic interpolation and a 4th order Runge Kutta stepping scheme to calculate the new position of each particle in space and time respectively. The vertical movements associated with the process of convection are parameterized in CMS: when particles are in the mixed layer a random contribution is added to the vertical velocity with a maximum speed of $|w|$=10 cm s^{-1} (van Sebille et al., 2013; Ypma et al., 2019) to mimic the strong non-hydrostatic vertical motions associated with small-scale convective plumes (Marshall and Schott, 1999).

4.3. Pathways upstream of 53^{o}N

We first analyze the pathways of water masses found in the boundary current at 53^{o}N, both from the float data (section 4.3.1) and from the Lagrangian analysis (section 4.3.2).

4.3.1. Pathways from Argo float data

The float trajectories clearly reveal pathways involving exchanges between the boundary current and the interior of the Labrador Sea (Figure 4.1). To distinguish if a float is in the interior or in the boundary current, we use the 3000 m isobath. To filter out possible short excursions of floats into the interior, we require that a float is found in the interior for more than 10 subsequent cycles (see section 4.2.1) to be labelled as being in the interior. We find 32 floats that continuously drift within the boundary current (ARGO-BC, Figure 4.4a) and 65 floats that are in the interior at some time before they exit the Labrador Sea with a southward direction at 53^oN (ARGO-interior, Figure 4.4b). It appears that some of these ARGO-interior floats travel directly from the interior to the Labrador Current on the western side of the basin while others follow more complex pathways: they first travel towards the West Greenland coast and then follow the boundary current to exit the basin. To be able to separate the floats based on these two types of pathways, we define a boundary in the northeast of the basin (black line in Figure 4.4c), placed such that it crosses the region of enhanced EKE known from altimetry data (e.g., Lilly et al., 2003). ARGO-interior floats that reach a position north of this line, i.e. those floats that approach the West Greenland coast after residing in the Labrador Sea interior, are categorized as ARGO-WG (purple trajectories in Figure 4.4c); the others, which head for the Labrador Current, are labelled ARGO-LC (yellow trajectories in Figure 4.4c). Based on this definition, the 65 ARGO-interior floats can be separated in 16 ARGO-LC floats and 49 ARGO-WG floats. Example trajectories of five ARGO-LC and ARGO-WG floats are shown in Figure 4.4(d-e).

The behavior of the ARGO-WG floats supports the view presented in chapter 3 that substantial exchange exists between the boundary current and the interior, and in particular in the eddy-rich region adjacent to the West Greenland coast. In chapter 3, it was shown that the water masses that have been transformed in the interior of the Labrador Sea are transported towards the region of high EKE on the Greenland side by eddy stirring and are then entrained in the boundary current, thus following an indirect route to leave the basin. Although the trajectories of the Argo floats may be affected by the surface currents during the brief period they spend at the surface, it is striking to see that many floats move from the interior towards the boundary along this same indirect route. If their trajectory is mainly governed by flows at their parking depths, which coincides with a depth typical for LSW in the interior (e.g., Bower et al., 2019), this suggests that this indirect LSW export route exists in reality. Moreover, the irregularity of the trajectories in Figure 4.4c corroborates the view that the presence of the local eddy field steers the pathway of LSW towards the West Greenland coast (Brüggemann and Katsman, 2019; Georgiou et al., 2019, 2020).

4.3.2. Pathways in MOM

Tracing the Lagrangian particles backwards in time allows us to identify the origin of the water masses found in the boundary current at 53^oN from the model perspective, and to investigate the main pathways they follow prior to reaching that latitude. A map of the particle probability (Figure 4.5a) reveals these preferred routes. To construct such a map, following Ypma et al. (2019), we first regrid every particle's positions on a regular

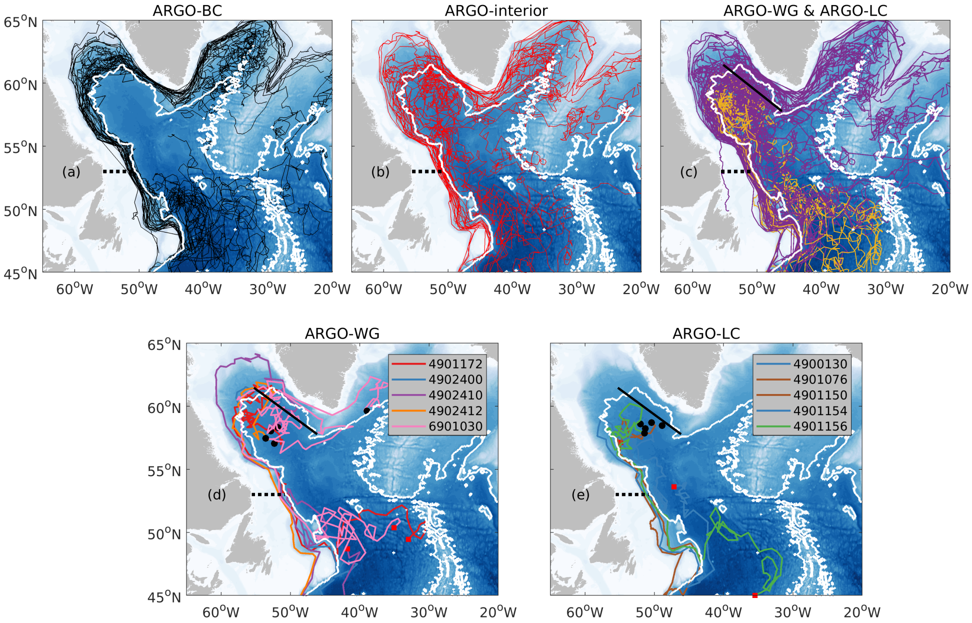

Figure 4.4: Example trajectories of floats that (a) drift within the boundary current (ARGO-BC, always onshore of the 3000 m isobath, 32 floats), (b) enter the interior of the Labrador Sea (ARGO-interior, 65 floats). (c) Subset of the float trajectories in (b), distinguishing between floats that are laterally advected directly from the interior to exit the Labrador Sea (ARGO-LC, trajectories in yellow, 16 floats) or reveal an exchange between the interior and the boundary current near the West Greenland coast (ARGO-WG, trajectories in purple, 49 floats). Example trajectories of five (d) ARGO-LC and (e) ARGO-WG floats. Each float number is indicated in the legend. Black (red) marker indicates the starting (ending) location of each float. The line used to separate the ARGO-WG and ARGO-LC floats is shown in black in (c-e). The 3000 m isobath is highlighted (white contour, bathymetry data from ETOPO1(Amante and Eakins, 2009)).

0.1^ox0.1^o grid and sum the transport carried through each of these grid boxes, by the particles. Next, this accumulated transport per grid box is divided by the total transport carried by all particles combined (in this case 25.3 Sv, see section 4.2.3).

Figure 4.5a shows that particles seeded at 53^oN follow pathways within the boundary current system in the SPNA but also follow pathways through the central Labrador Sea. Moreover, the enhanced particle probability in the vicinity of the west coast of Greenland where the EKE peaks (black contours in Figure 4.5a) suggests that the local eddy activity plays an important role for directing these pathways between the boundary current and the central Labrador Sea (hereinafter, central-LS), which is in agreement with the idealized model study presented in chapter 3.

To assess whether similar processes are acting in a realistic model and to quantify the relative importance of the pathways along the perimeter and through the basin interior, we follow a similar approach as in section 3.3 and separate particle pathways by determining if they remain in the boundary current or enter the central-LS.

Within the 6 year advection time, 85% of the particles seeded at 53^oN (i.e. 727066 particles) are traced backward in time to 44^oW near Cape Farewell (CF, dotted black line in Figure 4.5). We subdivide these particles further depending on whether they enter the central-LS between these two sections or not. We define a particle as in the central-LS when it is at least 50 km offshore of the smoothed 3000 m isobath (dark grey contour in Figure 4.5b) for more than 20 days, to filter out possible short and fast excursions of particles into the central-LS and back. This results in the definition of three categories (now considering forward in time): particles that enter the Labrador Sea at 44^oW offshore of the 3000 m isobath (hereinafter, *subpolar* particles, green trajectory in Figure 4.5b), and particles that enter the Labrador Sea at 44^oW onshore of the 3000 m isobath and either cross this isobath into the central-LS at some location (*interiorShort* particles, red example trajectory) or never leave the boundary current (*withinBC* particles, black example trajectory).

Not all the particles launched at 53^oN reach 44^oW when traced backwards in time. It appears that 10% of the particles do enter the central-LS but remain west of CF during the entire 6 year simulation. These particles are referred to as *interiorLong* particles (blue example trajectory in Figure 4.5b). The remaining 5% of the particles originate north of 65^oN (Davis Strait) and are referred to as *Davis* particles (magenta example trajectory in Figure 4.5b). The transport carried by the *subpolar*, *interiorShort*, *withinBC*, *interiorLong* and *Davis* particles amounts to 1.9 Sv, 11.2 Sv, 10.4 Sv, 0.9 Sv and 0.9 Sv, respectively.

Clearly, the *withinBC* and *interiorShort* particles represent the dominant upstream pathways since together they account for 85% of the total transport arriving at 53^oN (22.6 Sv) and this transport is divided roughly equally over these two pathways. We therefore focus on these two particle categories in the remainder of the paper, where we study the transformation of the water masses along these two pathways and their importance for the overturning in the Labrador Sea.

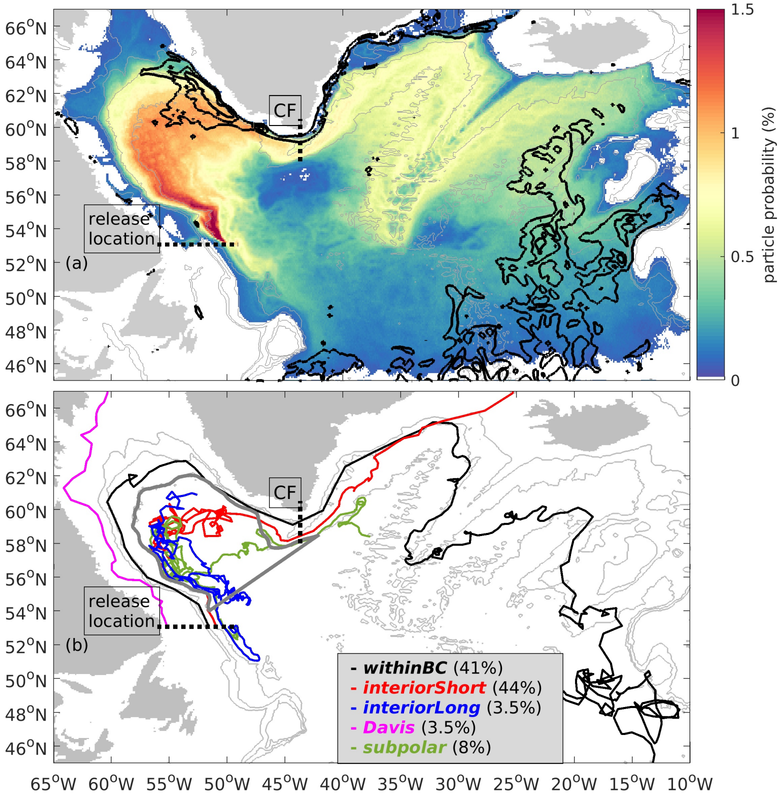

Figure 4.5: (a) Particle probability map (shading) highlighting the main pathways of waters upstream of the release location (dotted black line at 53^{o}N). Black contours indicate the annual mean EKE (contour interval is 200 cm^2 s^{-2}, starting from the contour line of 200 cm^2 s^{-2}). (b) Five example trajectories of particles categorized and color-coded depending on their pathways; *subpolar* particle (green trajectory), *interiorShort* particle (red trajectory), *withinBC* particle (black trajectory), *interiorLong* particle (blue trajectory) and *Davis* particle (magenta trajectory). The section at 44^{o}W (Cape Farewell, CF) and the 3000m isobath (dark grey contour) are used to separate the particles (see text for details on the procedure). Numbers in the legend indicate the percentage of the total transport carried by each pathway.

4.4. Water mass transformation in the Labrador Sea

To investigate where in the Labrador Sea the water masses traced by the *withinBC* and *interiorShort* particles change their thermohaline properties, we identify where these particles subduct from the mixed layer, and compare their T-S properties. Moreover, we investigate the overturning resulting from the water mass transformation occurring along these two pathways (section 4.4.1). Furthermore, we track the pathways that the *interiorShort* particles follow after subduction and explore their final properties at 53^{o}N (section 4.4.2).

4.4.1. Subduction of water masses and resulting overturning

We calculate the local subduction velocity as the sum of the transports of all particles that subduct within a certain grid box divided by its area, again using a regular 0.1^ox0.1^o grid (Brandt et al., 2007; Georgiou et al., 2020). The subduction velocity for the *withinBC* particles (Figure 4.6a) peaks in the western part of the Labrador Sea. This subduction region was also identified in Brandt et al. (2007), Palter et al. (2008), Georgiou et al. (2020) and MacGilchrist et al. (2020) and reflects convection that takes place in the boundary current itself. In addition, enhanced subduction velocities are found in a narrow strip along Cape Farewell. The total subduction rate of the *withinBC* particles in the Labrador Sea amounts to 2.4 Sv. For the *interiorShort* particles, high subduction velocities are found mainly in the central-LS and in the southwest of the basin (Figure 4.6b). The total subduction of the *interiorShort* particles amounts to 6.4 Sv of which 4.8 Sv occurs in the central-LS (i.e., offshore of the grey contour line in Figure 4.6b) and 1.6 Sv in the boundary current. Thus, in our analysis, 46% of the total subduction in the Labrador Sea occurs along the boundary current and 54% in the interior of the basin. In a recent study, MacGilchrist et al. (2020) performed a Lagrangian analysis of the subduction of NADW only, by tracking its pathways backwards from the deep North Atlantic. They also note a prominent role for subduction in the boundary current. According to this study, 60% of the total NADW ventilation results from subduction within the boundary current and about 25% from subduction in the interior of the Labrador Sea. It is yet unclear how to interpret this difference, as the applied model, the particle seeding strategy and water masses analyzed all differ from our analysis. The fact that most of the *interiorShort* particles subduct in the central-LS and then re-enter the boundary current prior to exiting the basin corroborates the importance of exchanges between the boundary current and the central-LS in regulating the properties of the water masses arriving at 53^oN.

Figure 4.6c-d, T-S diagrams of particle probability showing the temperature and salinity for the *withinBC* and *interiorShort* particles, show that the subduction location of the particles and their final properties at 53^oN are linked. The thermohaline properties of the *withinBC* and *interiorShort* particles that subduct in the Labrador Sea clearly differ; *withinBC* particles are relatively light, with densities σ_{53^oN}=27.55- 27.79 kg m^{-3} (Figure 4.6c), while *interiorShort* particles are denser with σ_{53^oN}=27.62- 27.83 kg m^{-3} (Figure 4.6d). Notably, *withinBC* particles that subduct near Cape Farewell (delineated by the dashed contour in Figure 4.6c) are lighter (σ=27.55- 27.63 kg m^{-3}) than particles that subduct elsewhere in the boundary current (σ= 27.63- 27.79 kg m^{-3}). This is in agreement with the idealized studies by Spall (2004), Straneo (2006c) and Brüggemann and Katsman (2019) that all showed that the boundary current gets denser in downstream direction due to buoyancy loss that it experiences.

For the *interiorShort* particles, two clear peaks can be distinguished in the T-S diagram. Particles that subduct within the boundary current in the southwest (encompassed by the dashed contour in Figure 4.6d) are lighter than particles that subduct in the central-LS (solid contour in Figure 4.6d), with densities σ_{53^oN}=27.60-27.80 kg m^{-3} and σ_{53^oN}=27.73-27.83 kg m^{-3}, respectively. This is a result of the stronger buoyancy loss over the central-LS, yielding a denser product of convection.

Both the subducted *withinBC* and *interiorShort* consist of water masses with densities within the density range of the LSW in this model (thick black lines in Figure 4.6c-d).

However, we found that less than 5% of the total subduction of the *withinBC* particles is associated with the LSW density range compared to 43% of the total subduction of the *interiorShort* particles. That is, our results indicate that the transformation of the *withinBC* particles, which only follow the boundary current, results into relatively lighter water masses than the transformation of the *interiorShort* particles. Note that the subduction of the *interiorShort* particles may occur both in the central-LS and in the boundary current.

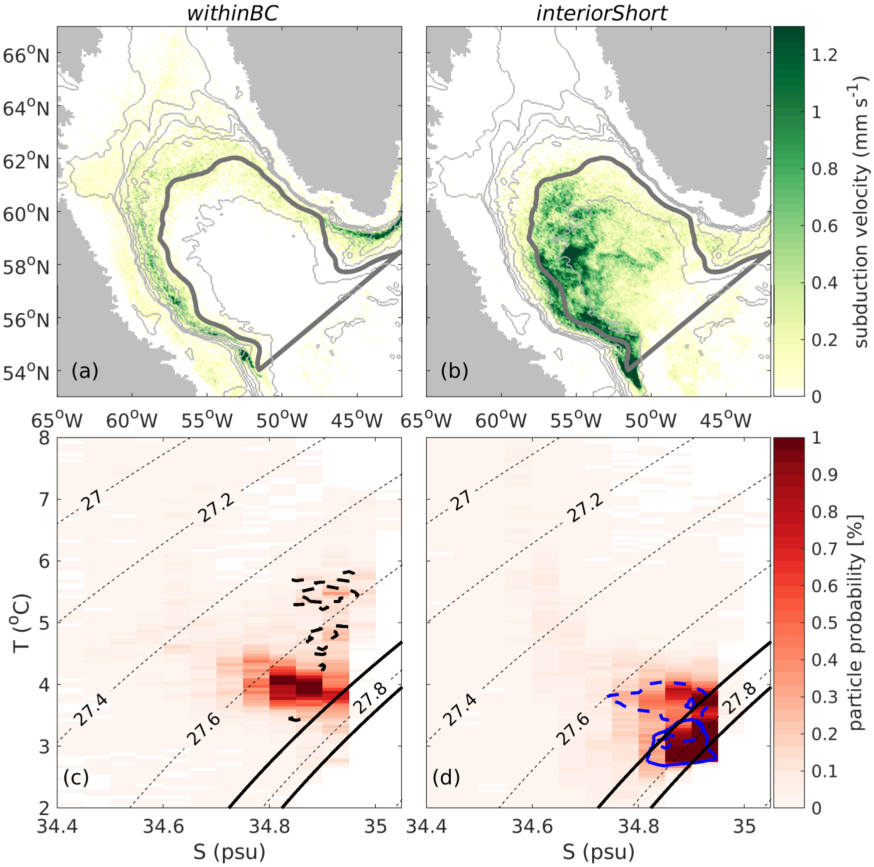

Figure 4.6: (a-b) Mean subduction velocity for (a) *withinBC* and (b) *interiorShort* particles. The 3000 m isobath used to distinguish the boundary current from the central-LS is indicated by the dark grey contour line. (c-d) T-S diagram of the thermohaline properties of the (c) *withinBC* and (d) *interiorShort* particles at 53^{o}N in terms of particle probability. The latter is calculated as the sum of the transports associated with all particles in a certain ΔT -ΔS bin divided by the total transport carried by the associated pathway (Ypma et al., 2019). The black dotted lines outline the isopycnals (in kg m^{-3}); thick black lines indicate the LSW density range in MOM. The black dashed contour in (c) encompasses 70% of the *withinBC* particles that subduct south of Greenland; the blue dashed (solid) contour in (d) encompasses 70% of the *interiorShort* particles that subduct in the boundary current (central-LS).

To investigate the relative importance of the regions where the particles are transformed for the overturning in the Labrador Sea, we evaluated the overturning in the

Labrador Sea resulting from this water mass transformation solely based on the transports carried by the *withinBC* and *interiorShort* particles. We assess the overturning between the cross-sections at 53^{o}N and 44^{o}W (particle release location and CF section; dotted lines in Figure 4.5a). The Eulerian overturning (green line in Figure 4.7) is calculated by first taking the difference in annual mean transport and then take the running integral over the vertical, in potential density anomaly (hereinafter, density), temperature and salinity bins. The Lagrangian overturning is calculated similarly, only now we take the differences between the summed volume transport carried by the *withinBC* (black lines in Figure 4.7) and *interiorShort* particles (red lines), respectively. We also add an estimate for the total Lagrangian overturning (purple lines in Figure 4.7), which is simply based on the summed transports carried by the *withinBC* and *interiorShort* particles. This is not expected to match the Eulerian overturning, as contributions from the *subpolar*, *interiorLong* and *Davis* particles cannot be computed. The overturning based on these two classes of particles peaks at σ=27.60 kg m^{-3} and amounts to 4.3 Sv (purple line in Figure 4.7a). In temperature and salinity space we find a maximum overturning of 9.1 Sv and 9.7 Sv at 4.2 ^{o}C and 34.94 psu, respectively (Figure 4.7b-c and Table 4.3), indicating that substantial density compensation occurs (Zou et al., 2020).

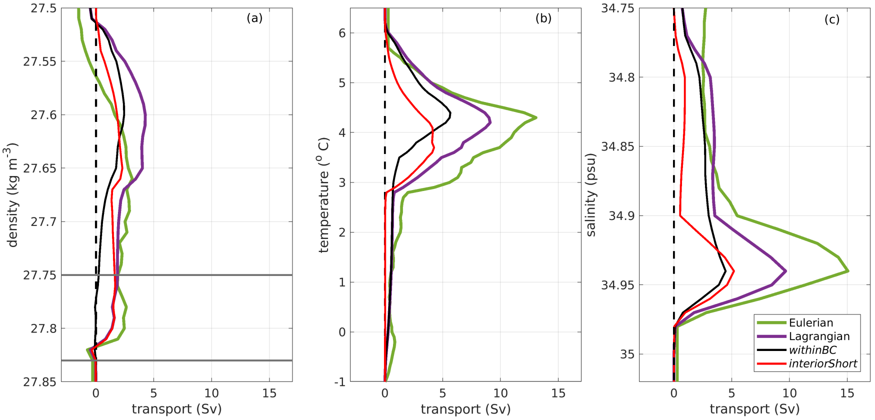

Figure 4.7: Absolute accumulated change of the volume transport (in Sv) between the sections at 53^{o}N and 44^{o}W (release location and CF section, dotted lines in Figure 4.5a) binned every (a) 0.01 kg m^{-3} in density, (b) 0.1 ^{o}C in temperature and (c) 0.01 psu in salinity space for the annual mean Eulerian values (green line, mean over the particle release year), for the *withinBC* (black line) and *interiorShort* (red) particles and for their sum (Lagrangian mean, purple). Grey horizontal lines in (a) indicate the LSW density range in MOM.

The *withinBC* and *interiorShort* pathways contribute roughly equally to the net Lagrangian overturning in the Labrador Sea. The maximum overturning resulting from the *withinBC* particles (black lines in Figure 4.7) occurs at a lighter density (higher temperature) than the overturning resulting from the *interiorShort* particles (red lines) at σ=27.60 kg m^{-3} and σ= 27.65 kg m^{-3} (4.4 and 3.7 ^{o}C), respectively. Interestingly, the overturning associated with the *interiorShort* particles shows significant contributions in the density range σ=27.75-27.82 kg m^{-3}, which is within the signature of the LSW in this model (section 4.2.2); the overturning associated with the *withinBC* particles is negligible at this density range. This once more confirms that the denser water masses are formed

Table 4.3: Maximum overturning transport in the Labrador Sea (in Sv) and property values at which this occurs, in density, temperature and salinity space. Values obtained in this study are given based on the Eulerian and Lagrangian analysis, the latter split by the two main pathways (i.e., *withinBC* and *interiorShort*). Values reported from observations in Zou et al. (2020) are provided for comparison.

	density space		temperature space		salinity space	
	(Sv)	(kg m^{-3})	(Sv)	(^{o}C)	(Sv)	(psu)
Eulerian	3.1	27.66	13.1	4.3	15.1	34.94
Lagrangian	4.3	27.60	9.1	4.2	9.7	34.94
withinBC	2.3	27.60	5.7	4.4	4.5	34.94
interiorShort	2.3	27.65	4.2	3.7	5.2	34.94
Zou et al. (2020)	3.3	27.70	13.9	3.7	11.4	34.90

in the central-LS, whereas convection along the boundary current results in lighter water masses. The fact that the signal of the various direct and indirect pathways of water masses is evident in the overturning signal within different density classes emphasizes the complex nature of processes regulating the overturning in the Labrador Sea.

4.4.2. Pathways and final properties of convected water masses

The T-S diagrams in Figure 4.6c-d reveal that the densest water masses that exit the Labrador Sea at 53^{o}N are associated with the *interiorShort* particles that subduct in the central-LS. So, we now further investigate the pathways and properties of this subset of *interiorShort* particles, which represent 4.8 Sv (75%) of the 6.4 Sv of subduction that takes place in the Labrador Sea. Visual inspection of their trajectories reveal two preferred routes from their subduction location to 53^{o}N: particles tend to either travel towards the west coast of Greenland or towards the Labrador side of the basin before re-entering the boundary current. This is in agreement with the idealized study of Brüggemann and Katsman (2019) and the results discussed in chapter 2 that both showed by using passive tracers that the densest water masses formed in the interior of the basin are steered towards the topographic narrowing aided by the velocity shear induced by the presence of the eddy field. In particular, Brüggemann and Katsman (2019) showed that convected waters formed in the basin interior move along isopycnals from the convection region towards the boundary current in the east, and mainly towards the topographic narrowing. This process can be thought of as a stochastic path of particles influenced by the eddies: in regions where a lot of eddies are present, the particles are steered in all directions. When a particle then enters a region of low eddy activity, it will move much slower and might be considered 'stuck' in such a relatively quiet region. However, if a particle remains in the region of high EKE, the eddies can advect them further, in any direction. Following these arguments, the particles will be distributed everywhere within the high EKE region and will eventually also reach the West Greenland coast. That is, the limited extent of the EKE field yields a particle pathway mimicking a random walk with a preferred direction.

Therefore, we further separate the subset of *interiorShort* particles based on their proximity to the high EKE region near Greenland (Figure 4.8a-b). Analogous to the analysis of the Argo floats presented in section 4.3.1, we define a boundary in the northeast (black line in Figure 4.8a-b), placed such that EKE<200 $\mathrm{cm}^2\ \mathrm{s}^{-2}$ southwest of it. Particles that at some time cross this line from southwest to northeast are classified as following the West Greenland (WG) path; all other particles are considered to follow the LC-path. It appears that most newly-formed dense water leaves the central-LS following the direct Labrador Current (LC) path (3.0 Sv; 60% of the total transport of this subset of particles), but that the indirect WG-path also contributes significantly (1.8 Sv; 40%).

Example trajectories for these two pathways are shown in Figure 4.8a-b, traveling from their subduction location (magenta dots) to 53^oN. To better visualize preferred routes Figure 4.8c-d shows maps of the particle probability for these two pathways (maps are constructed as in Figure 4.5a). For the WG-path (Figure 4.8c), the particle probability is significantly high at the west coast of Greenland and is co-located with the region of enhanced EKE (black contours), indicating that the WG-path is regulated by the local eddy activity since eddies are needed to steer the dense waters into the boundary current (Brüggemann and Katsman, 2019). Particles that follow the WG-path are steered towards Greenland and then flow cyclonically around the basin to 53^oN, yielding a peak in particle probability at the Labrador side (Figure 4.8c). The particle probability for the LC-path (Figure 4.8d) outlines the direct export route of newly-formed water masses from the central-LS to the boundary current at the Labrador side (Brandt et al., 2007; Palter et al., 2008; Georgiou et al., 2020).

To investigate the water mass properties of this subset of the *interiorShort* particles that subduct in the central-LS when exiting the Labrador Sea, we analyze their transport per density bin at 53^oN (Figure 4.9a-b). For the WG- and LC-paths, the maximum transport at 53^oN is found at a density range of σ=27.81- 27.82 kg m^{-3}, which corresponds to the denser limit of the LSW density range in this model (see section 4.2.2). Interestingly, 30% of the transport carried by the WG-path particles is found within this LSW density range compared to 15% of the transport carried by the LC-path particles. Clearly, relatively light waters are carried mostly along the LC-path. This corroborates that the denser water masses formed in the central-LS most likely follow the indirect route described by the WG-path. The vertical distribution of the particle transport when they reach 53^oN (Figure 4.9c) also reflects that the WG-path carries the denser water masses, since these particles are found deeper in the water column than the particles that follow the LC-path (Figure 4.9c).

In summary, we have shown in this section that water mass transformation occurs along each of the main pathways (i.e. *withinBC* and *interiorShort*), resulting in water masses with different thermohaline properties. As the pathways that waters follow after subduction are linked to different density classes, clearly this regulates the overturning in the Labrador Sea. Moreover, an export pathway of LSW exists, that approaches the West Greenland coast, like the pathway found in chapter 3 (Figure 3.11). The transport carried via this WG-path is about half of that carried along the LC-path, thus implying that the presence of eddies plays a crucial role in shaping the pathways of the convected water (Brüggemann and Katsman, 2019).

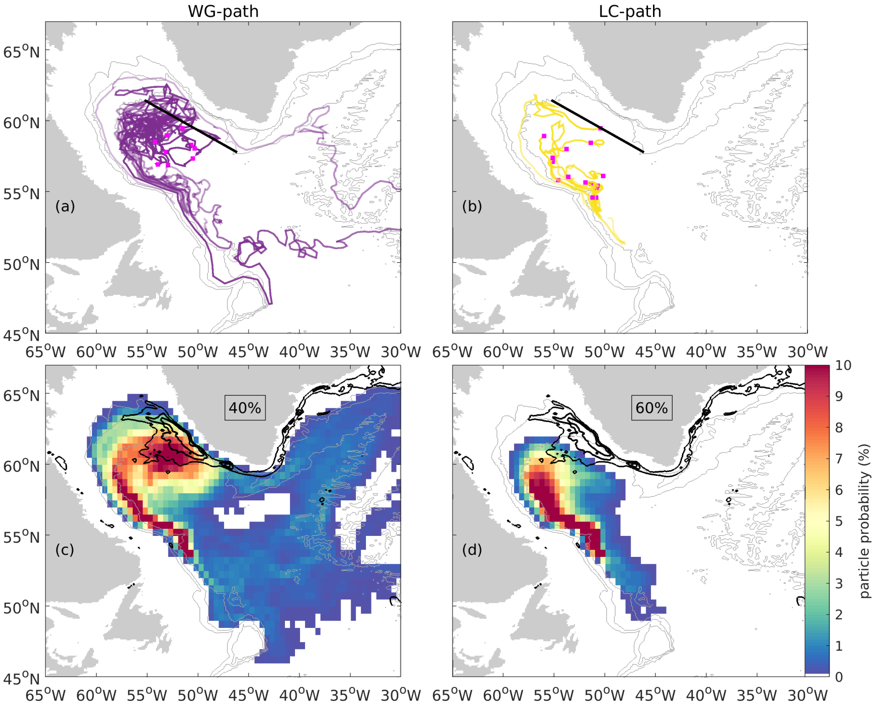

Figure 4.8: (a-b) Example trajectories for the subset of *interiorShort* particles that subduct in the central-LS, from their subduction location (magenta dots) to 53^{o}N and (c-d) associated particle probability map. The set of particles is split by evaluating if they (a,c) travel towards the west coast of Greenland (WG-path) by crossing the black line in (a-b) or (b,d) travel towards the Labrador coast (LC-path). Northeast of the black line in (a-b) the EKE is higher than 200 cm^2 s^{-2}; black contours in (c-d) indicate the annual mean EKE (contour interval is 200 cm^2 s^{-2}, starting from the contour line of 200 cm^2 s^{-2}). Also shown in (c-d) is the percentage of the volume transport carried by the WG-LC paths with respect to the total carried by this subset of the *interiorShort* particles.

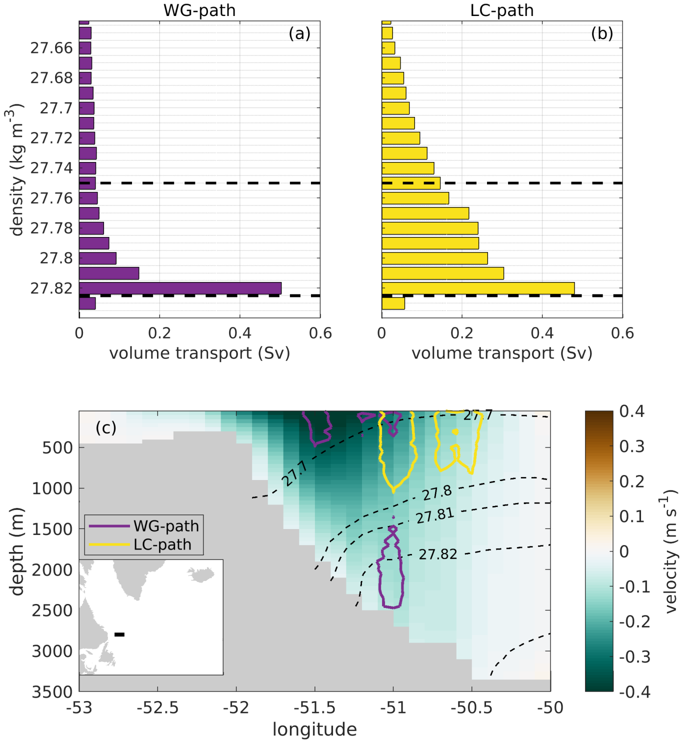

Figure 4.9: (a-b) Volume transport at 53^{o}N carried by the particles that subducted in the central-LS and then travel towards (a) the vicinity of the west coast of Greenland (WG-path) and (b) the Labrador side (LC-path) binned by 0.01 kg m^{-3} in density space. Black dashed horizontal lines in (a-b) indicate the LSW density range in MOM. (c) Cross section of the vertical distribution of the volume transport associated with the two pathways at 53^{o}N (black line in the inset): WG-path (purple contours) and LC-path (yellow contours) together with the annual mean velocity of the simulation (shading). Purple (yellow) contours encompass 60% of the WG-path (LC-path) particles. The dashed contours outline the isopycnals (in kg m^{-3}).

4.5. Timescales associated with the pathways

It is expected that the various pathways that particles follow prior to exiting the Labrador Sea at 53^oN affect the associated timescales: the residence time of water masses in the Labrador Sea and the time from subduction to arrival at 53^oN.

First, we focus on their residence time in the Labrador Sea: the time it takes for a particle to travel from Cape Farewell (CF, dotted line in Figure 4.5b) to 53^oN, and how this depends on a particle's density at 53^oN which in turn reflects the water mass transformation it experienced in the basin (section 4.4).

The *withinBC* particles are characterized by a short residence time (Figure 4.10a); almost all particles reach 53^oN in less than two years. From these particles, the ones that represent lighter water masses (density range of σ_{53^oN}= 27.60-27.70 kg m^{-3}) arrive 53^oN within 5-8 months; their transport amounts to 3.9 Sv. The *withinBC* particles with $\sigma_{53^oN} > 27.75$ kg m^{-3}, which represent a smaller transport (2.1 Sv), display longer residence times between 6 months and 2 years. The *interiorShort* particles associated with relatively light water masses (i.e. density range σ_{53^oN}=27.65-27.75 kg m^{-3}) are relatively fast, with a residence time of less than a year (Figure 4.10b) and their transport amounts to 3.2 Sv. However, the majority of the *interiorShort* particles (7.3 Sv) have longer residence times, up to the 6 years maximum advection time (Figure 4.10b). They are associated with the LSW density range in MOM (i.e., σ=27.75-27.83 kg m^{-3}). This confirms the findings from the idealized study presented in chapter 3, that the densest water masses formed in the interior of the Labrador Sea stay in the basin longer.

We also estimate the residence time of the Argo floats (section 4.2.1 and section 4.3.1) for comparison. Since their starting locations differ, we now define the residence time as the time it takes to travel from the location where they are first found in the Labrador Sea until they reach 53^oN. As for the particles, we distinguish the floats that travel in the boundary current the entire time (ARGO-BC floats, n=32, see Figure 4.4a) from those that at some moment are located in the central-LS (ARGO-interior floats, n=65). It is clear from Figure 4.10c that the ARGO-BC floats (dashed black line) reach 53^oN faster than the ARGO-interior floats (dashed red line): 90% of the ARGO-BC floats arrives within 1 year; for the ARGO-interior floats this takes 3.5 years. The estimated residence times for the floats correspond well to the results obtained from the Lagrangian particles: 90% of the transport carried by the *withinBC* and *interiorShort* particles reaches 53^oN within 1.5 and 3 years, respectively (black and red solid lines in Figure 4.10c). The results are in agreement with the timescales reported in observational (Palter et al., 2008) and modelling (Brandt et al., 2007) studies.

Next, we investigate the impacts of the pathways (and hence of the boundary-interior exchange) for the export timescales of the particles that subduct in the central-LS, distinguishing the WG- and LC-paths as in section 4.4. The export timescale is defined as the time it takes a particle to travel from its final subduction location to 53^oN. It is found that the water masses that follow the LC-path (i.e. towards the Labrador side) are rapidly exported from the Labrador Sea; 90% of the transport carried by the LC-path is exported within 15 months (not shown). This is in agreement with previous studies that showed that the newly formed LSW is rapidly exported from the interior of the basin by being entrained in the boundary current (e.g., Brandt et al., 2007; Georgiou et al., 2020). Not

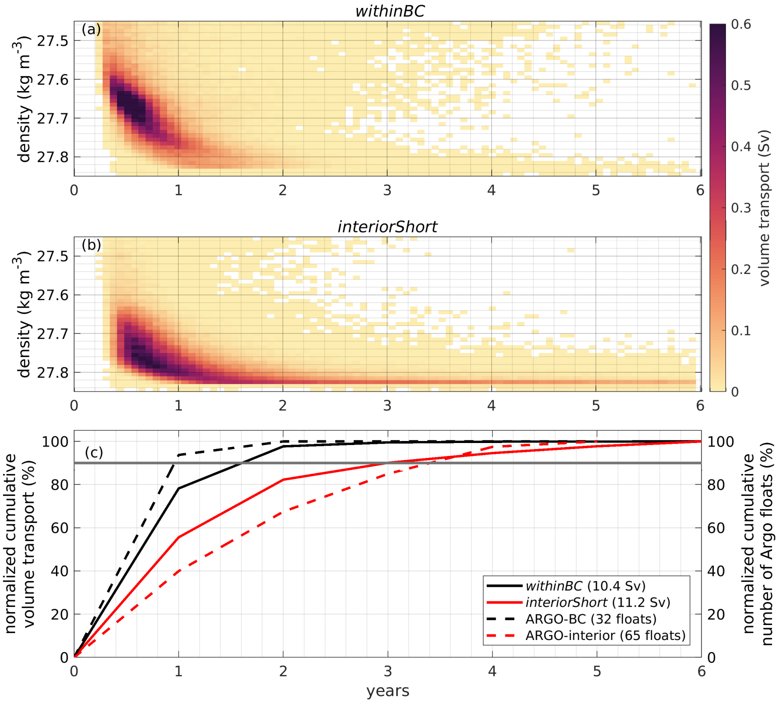

Figure 4.10: Volume transport carried by the particles as a function of residence time and density at 53^{o}N (σ_{53^oN} in kg m^{-3}) for the (a) *withinBC* and (b) *interiorShort* particles. The volume transport is binned in $\Delta\sigma$= 0.01 kg m^{-3} and Δt = 25 day intervals. (c) Normalized cumulative volume transport of the *withinBC* (black line) and *interiorShort* (red line) particles and normalized cumulative number of Argo floats that either travel within the boundary current (ARGO-BC, black dashed line) or are found in the central-LS at some moment (ARGO-interior, red dashed line), as a function of residence time. Grey horizontal line in (c) indicates the 90% limit. Float trajectories for ARGO-BC and ARGO-interior are shown in Figure 4.4a and b, respectively.

surprisingly, the export timescales of water masses that follow the indirect WG-path are much longer; 90% of the transport carried by the WG-path is exported within 4 years (not shown).

The finding that the transport of convected water from the interior towards the west coast of Greenland takes almost 2.5 years longer than the direct transport on the Labrador side, combined with the fact that different water masses are formed along these pathways, has important implications for the variability in transport of these water masses to be expected downstream in response to variations in LSW formation rates.

4.6. A three-dimensional view on the export of convected waters

In this study, we showed that the different pathways that water masses in the Labrador Sea follow prior to reaching at 53^{o}N (Figure 4.5b) have a direct impact on the water mass properties with which they arrive there and on their residence time in the basin, and hence on the Labrador Sea overturning dynamics.

The analysis of the pathways of the water masses that are transformed in the central-LS (i.e. the WG-LC- paths, section section 4.4.2), clearly shows that the local eddy activity regulates their fate in the Labrador Sea (Figure 4.8 and Figure 4.9). The denser water masses formed in the central-LS tend to follow either a direct route towards the Labrador side (LC-path) or a more complex pathway that seems to be steered by the eddy activity near the west coast of Greenland (WG-path). In the idealized model simulation of Brüggemann and Katsman (2019), the dense water masses that have been formed by convection in the interior are laterally transported towards the boundary current along isopycnals. To investigate if this is also the case in this realistic model, we analyze the re-entry of the particles in the boundary current after subduction in the central-LS. To this end, we investigate where the particles cross the 3000 m isobath for the last time (our definition of re-entry of the boundary current) and with what density (σ_{crossing}), and compare this to the local annual mean density of the boundary current, $\bar{\sigma}_{3000m}$ (Figure 4.11).

It appears that most WG-path particles re-enter the boundary current at a distance between 800-1100 km downstream from 44^{o}W (purple shading in Figure 4.11a), which coincides with the region of enhanced EKE. This entrainment occurs between 2100-2800 m depth where the annual mean density of the boundary current is $\bar{\sigma}_{3000m}$ >27.82 kg m^{-3} (contours). In contrast, the majority of the LC-path particles re-enter the boundary current at 2000-2150 km downstream from 44^{o}W (Figure 4.11c) and at shallower depths (500-2000 m). At this depth and location, the boundary current has a mean density $\bar{\sigma}_{3000m}$ = 27.70- 27.82 kg m^{-3}.

The density of the particles that re-enter the boundary current by crossing the 3000 m isobath (σ_{crossing}) is highly correlated to the mean density of the boundary current ($\bar{\sigma}_{3000m}$) at the location of the crossing (Figure 4.11b,d). This supports the view that the entrainment of convected waters in the boundary current occurs along isopycnals (Brüggemann and Katsman, 2019). It also implies that this entrainment can only take place where the density and depth of the convected water mass match the local properties of the boundary current, which adds a potentially strong constraint on this process. This view is in agreement with the result that convected water of varying density is entrained in the boundary current at the Labrador side (LC-path, Figure 4.9b), while only the densest convected waters re-enter the boundary current along the WG-path (Figure 4.9a). Near the Greenland coast, the stronger stratification resulting from the advection of buoyant water from the boundary current by the eddies effectively blocks the re-entry of lighter convected waters ($\sigma \simeq$ 27.70-27.75 kg m^{-3}) there. At the topographic narrowing, the isopycnals are strongly tilted downward in the direction of the coast. This induces an along-isopycnal transport of the densest water masses from the interior towards the boundary current in deeper layers (Brüggemann and Katsman, 2019). As a consequence, at 53^{o}N, the denser water masses that follow the WG-path are found deeper in the water column than those that follow the LC-path (Figure 4.9c) since they follow different isopycnals in the boundary current (Figure 4.11a).

To visualize this difference between this lateral, along isopycnal transport for the direct and indirect pathways schematically, we use two particles that follow the LC-path and the WG-path (Figure 4.12). Both particles are subducted in the central-LS (magenta

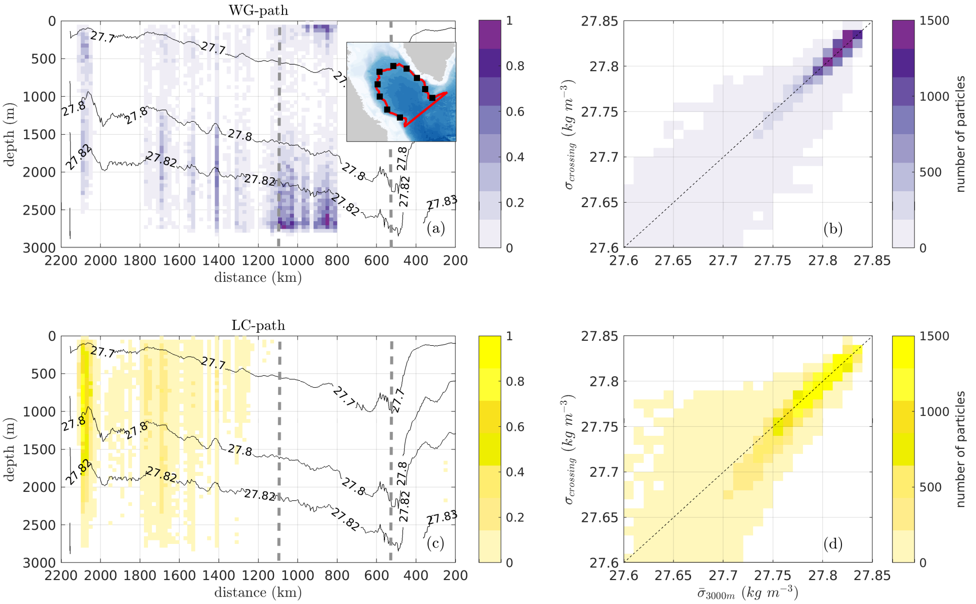

Figure 4.11: (a,c) Normalized number of particles that cross the 3000 m isobath and re-enter the boundary current as a function of distance downstream of Cape Farewell and depth, for (a) the WG-path (purple shading) and (c) the LC-path (yellow shading). Particles are binned over segments of 30 m in depth and 50 km in alongshore direction, starting from 44^{o}W (see inset in (a), black squares mark distances of 200 km). Note that the horizontal axis is flipped. The black contours outline the annual mean density of the boundary current as a function ($\bar{\sigma}_{3000m}$, in kg m^{-3}) of the alongshore coordinate. Grey dashed contours denote the region near the West Greenland coast where EKE>200 cm^2 s^{-2}. (b,d) Scatter plot of the density of particles when they cross the 3000 m isobath (σ_{crossing}, in kg m^{-3}) versus the annual mean density of the boundary current $\bar{\sigma}_{3000m}$ at this location, for particles that follow (b) the WG-path and (d) the LC-path in terms of number of particle. The latter is calculated as the sum of particles in a certain $\Delta\sigma$-$\Delta\sigma$ bin ($\Delta\sigma$ = 0.01 kg m^{-3}).

markers in Figure 4.12). It is clear that the particle that follows the LC-path (yellow line in Figure 4.12) is directly entrained in the boundary current at the Labrador side at a depth of 1620 m, and follows the boundary current to 53^{o}N. Along this part of its trajectory, it rises to a depth of 1300 m. In contrast, the particle the follows the WG-path (purple line in Figure 4.12) moves towards the west coast of Greenland, right underneath the region of enhanced EKE (red shading) and is entrained in the boundary current at a depth of 2050 m. Once in the boundary current (dotted purple line), the particle is carried to 53^{o}N at a depth of 2000 m.

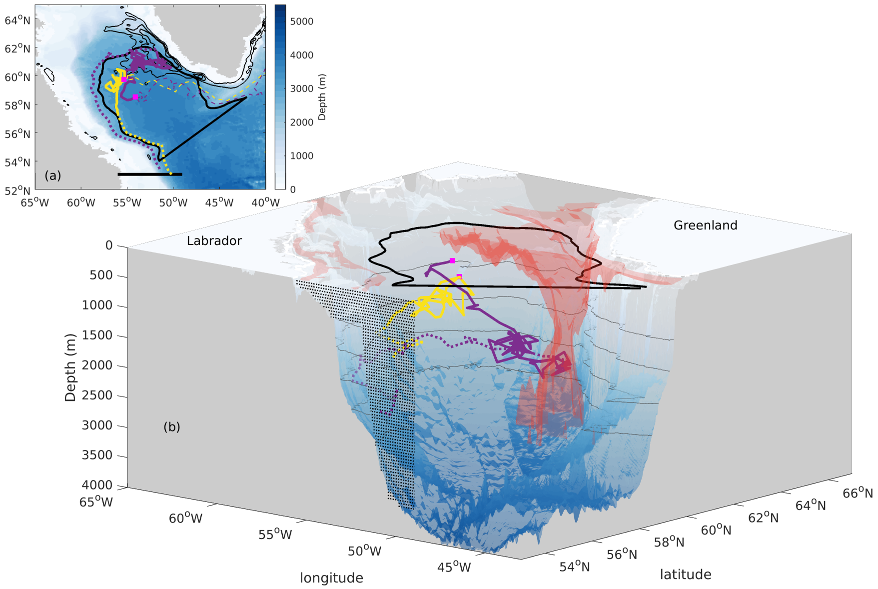

Figure 4.12: Example of two particles that after their subduction location (magenta markers) follow either the LC-path (yellow line) or the WG-path (purple line) to reach 53^{o}N in (a) plane and (b) 3-D view. Dashed lines in (a) show the trajectories of the particles before they subduct. Dotted lines in (a-b) show the trajectories once these particles re-enter the boundary current. The release location at 53^{o}N is indicated in the black line in (a) and shaded area in (b). The central-LS as defined in this study is highlighted by the thick black line in the interior of the Labrador Sea. Enhanced values of the annual mean EKE are shown in (a) at the surface (black contours, contour interval is 200 cm^2 s^{-2}, starting from the contour line of 200 cm^2 s^{-2}) and in (b) over the vertical (red shading). Bathymetry data are obtained from ETOPO1 Amante and Eakins (2009).

4.7. Summary and conclusions

In this study, we use Lagrangian particles launched at 53^{o}N and traced backwards in time using the output of an ocean eddy-permitting model (MOM) to investigate the upstream pathways of the water masses that exit the Labrador Sea. The motivation of this study stems from the need to improve our understanding on the export routes of the water masses that constitute the lower limb of the AMOC. In particular, building on the insights gained from the idealized Lagrangian study presented in chapter 3, we explore the relative importance of the different pathways that water masses follow prior to exiting the Labrador Sea at 53^{o}N by investigating the water mass transformation along these pathways, the impact on the overturning in the basin, and the residence and export timescales associated with the pathways in this more realistic ocean model.

We show that in this model simulation, 85% of the total transport carried by the launched particles follow either the boundary current (*withinBC* particles) or a more complex route that involves boundary current-interior exchanges (*interiorShort* particles) from Cape Farewell (southern tip of Greenland) to 53^{o}N within a 6 year period (Figure 4.5). The transformation of the water masses differs along these routes, which leads to differences in their final properties; lighter water masses are formed within the boundary current (*withinBC* particles), while denser water masses are formed in the central-LS (*interiorShort* particles). This is reflected in the relative importance of these pathways for the overturning in density space; the overturning found at densities higher than 27.66 kg m^{-3} is mainly attributed to the *interiorShort* particles (Figure 4.7a). Only in lighter layers the impact of the transformation of the *withinBC* particles is important. Thus, we conclude that the indirect route which is regulated by boundary current-interior exchanges is important for the representation of the overturning in denser layers.

With regard to volume transport, our results indicate that the contribution of boundary current subduction is as important as that of subduction in the interior of the Labrador Sea (section 4.4.1). This is in line with other studies who found that the boundary current subduction plays a key role (Brandt et al., 2007; MacGilchrist et al., 2020) for the ventilation of the water masses in the Labrador Sea. However, our Lagrangian analysis shows that *interiorShort* particles which are subducted close to or within the boundary current can still take a long route through the interior of the Labrador Sea before they finally exit. Thus, care needs to be taken whether particles which are subducted close or within the boundary current are really confined to the boundary current until they exit the Labrador Sea. Moreover, the water masses transformed in the interior are usually denser than those transformed over the boundary current (Figure 4.6c-d). Thus, the densest water masses formed in the Labrador Sea typically take a longer and more complex route compared to the water masses transformed in the boundary current.

Our investigation of the residence time of the major pathways (i.e. *withinBC* and *interiorShort* particles) shows that lighter water masses formed close to or within the boundary current are exported faster than the denser water masses formed in the central-LS (Figure 4.10), in line with the more qualitative results obtained from the idealized studies of Brüggemann and Katsman (2019) and chapter 3: 90% of the volume transport carried by the *withinBC* and *interiorShort* particles reaches 53^oN within 1.5 and 3 years, respectively (Figure 4.10c). In particular, we show that the denser water masses formed in the central-LS first follow an eddy-driven path towards the West Greenland coast (WG-path, Figure 4.8a) and re-enter in the boundary current there before reaching 53^oN. Therefore, these water masses travel longer distances than the ones that formed within the boundary current itself (*withinBC* particles) or the lighter water masses that formed in the central-LS and are rapidly exported at the Labrador side (LC-path). Last, we showed that the entrainment of convected water mass can only take place where its density and depth match the local properties of the boundary current, which adds a potentially strong constraint on this process (Figure 4.11 and Figure 4.12).

One of the limitations of the Lagrangian analysis in the idealized study presented in chapter 3 was the lack of a possible connection between the Labrador and the Irminger Sea, as the model domain was limited to the Labrador Sea only. Interestingly, in this study an indication of a connection between the two basins appears; Figure 4.8(a,c) shows that some particles that follow the WG-path move towards Greenland and travel farther east than 44^oW before they reach 53^oN. This would be in agreement with a pathway along the mid-depth recirculation cells found in the SPNA (e.g., Lavender et al., 2000; Bower et al., 2009; Lozier, 2012; Rhein et al., 2015), where newly-formed LSW flows towards the eastern SPNA (Figure 4.8c). In our Lagrangian set-up, the transport carried by these particles only amounts to 0.2 Sv. From this low number one cannot conclude that this potential pathway between the Labrador and Irminger Seas is not relevant, as the strategy we chose for seeding the Lagrangian particles is not suited to address this question. To investigate this pathway explicitly, a different strategy for the deployment of the particles is required.

Furthermore, we find in agreement with recent studies (Lozier et al., 2019; Zou et al., 2020) that the overturning in density space is stronger in the eastern part of the North Atlantic compared to the Labrador Sea (see Figure 4.2e). It is important to note that the main findings in these observational studies, namely a weak overturning in density space in the Labrador Sea due to the near-compensation of the overturning in temperature and salinity space, only document the net result of the events that take place in the region. Our study reveals the richness of processes and pathways that give rise to this observed net overturning, characterized by a complex interplay between the convective interior, the boundary current and the eddy field. Using a model forced by Normal Year Forcing simplifies the analysis of the Lagrangian particles but prevents us from analyzing any impacts of the known large interannual variability in the surface forcing (Moore et al., 2012). Therefore, it is by no means clear yet how sensitive the water mass transformation processes and pathways are to, for example, changes in the surface forcing, and at what timescales a potential response to such changes would become apparent as a signal in the net overturning strength. Hence, an obvious next step is to investigate the response of pathways and water mass transformation to anomalies in forcing conditions, by carefully initializing and tracing Lagrangian particles released in different years, using interannually varying velocity fields rather than looping over a one-year dataset as is done here.

The relatively long time it takes for *interiorShort* particles to complete the indirect route to 53^oN compared to the direct route followed by the *withinBC* particles, and the outcome that for *interiorShort* particles the export timescales depend on pathway and location of re-entry of the boundary current (Figure 4.10) indicates that care should be taken when attempting to directly relate variability in LSW production to LSW propagation to the subtropics and thus to AMOC variability. This study reveals a complex three-dimensional view of the LSW export and shows that the interior-boundary current exchanges are crucial for the LSW pathways and export timescales. Better understanding of the processes that control the transports along these various pathways and the variability therein is needed to fully understand the connections between the processes occurring in the Labrador Sea and AMOC variability. According to our study, these pathways are strongly governed by the combination of the density and depth of LSW in the interior and the density structure of the boundary current system along the basin's perimeter.

Chapter 5

Sensitivity of the upstream pathways of the waters exiting the Labrador Sea to changes in the surface heat flux

The sensitivity of the upstream pathways and the transformation of the water masses exiting the Labrador Sea to changes in the surface heat fluxes are investigated in an idealized model. We performed Lagrangian analyses by using the output of two sensitivity simulations (scenarios) where the winter surface heat loss is increased or decreased by 50% from the one applied to the reference simulation. For the sensitivity to surface heat fluxes, we find that, in a colder (warmer) regime the product of convection is denser (lighter) and this has a direct impact on the density where the maximum overturning is found in the Labrador Sea in each scenario. Moreover, the overturning is reduced by 40% (15%) with respect to the reference simulation under the scenario of weaker (stronger) winter surface heat loss. The analysis of the eddy-driven transport of convected waters from the interior towards the boundary current on the west coast of Greenland, shows that in a colder (warmer) regime this transport is stronger (weaker). This indicates that the densest waters formed in the interior of the Labrador Sea tend to follow a longer route towards Greenland before exiting the basin, which has potential implications for the arrival time of signals of variability therein farther downstream. The results presented in this chapter highlight that in a changing climate, the division of the preferred pathways is affected since these pathways are related to the density of the product of convection and the strength of the boundary-interior exchange in the Labrador Sea. Thus, it is important to advance our knowledge on the mechanism behind the boundary-interior exchange to fully understand the link between the production of dense water in the Labrador Sea and the variations in the local overturning.

5.1. Introduction

The product of deep convection, Labrador Sea Water (LSW), is the upper component of the North Atlantic Deep Water (NADW), which in turn constitutes the lower limb of the Atlantic Meridional Overturning Circulation (AMOC, e.g., Rhein et al., 2015). Historically, studies on climate variability suggested a strong dependence between this overturning strength and changes in deep water formation in the Labrador Sea (Biastoch et al., 2008; Zhang, 2010; Yeager and Danabasoglu, 2014). Recent studies revisited the relative importance of the Labrador Sea for the variability of the AMOC. Observational studies indicate that the water mass transformation in the Nordic Seas and northeastern subpolar gyre display a dominant role for the AMOC variability (Lozier et al., 2019; Chafik and Rossby, 2019; Zou et al., 2020). However, MacGilchrist et al. (2020) performed a Lagrangian analysis of the subduction of NADW in an eddy-permitting numerical simulation and indicated a dominant role of the Labrador Sea for the ventilation of this water mass. The results discussed in chapter 3 and chapter 4 also highlight a complicated connection between the deep water formation and the overturning in the Labrador Sea. One of the main findings in these chapters was that the densest water masses take more than six years to exit the Labrador Sea, and that this may obscure a strong link between the LSW formation and AMOC variability in observations. The complex relation between the variability of the LSW formation and the AMOC variability might result from the complex nature of the spreading of LSW from its formation location.

Possible export routes of LSW have been reported (e.g., Palter et al., 2008; Bower et al., 2019), but their relative importance for its export timescales and for the AMOC variability is still unclear. Moreover, it is shown in this thesis that the routes that the newly formed LSW follows can either be direct or indirect (chapter 3). The direct export route of newly-formed LSW is associated with the lateral advection of LSW from the interior of the basin towards the Labrador side where it can be entrained in the Deep Western Boundary Current (DWBC, path 1 in Figure 5.1) and rapidly flow southwards (e.g., Talley and McCartney, 1982; Brandt et al., 2007; Feucher et al., 2019). Another direct export route (path 2 in Figure 5.1) is related to the formation of the LSW within the boundary current itself (Cuny et al., 2005; Brandt et al., 2007, chapter 3 and chapter 4). Moreover, an indirect route of LSW that involves boundary current-interior exchanges is reported in several studies (Straneo et al., 2003; Palter et al., 2008; Brüggemann and Katsman, 2019, chapter 2). These studies have shown that convected water is transported from the interior towards the west coast of Greenland, in particular in the region where the eddy activity peaks, and is then entrained in the boundary current (path 3 in Figure 5.1). Last, within the subpolar gyre, the mid-depth recirculation of the LSW indicates an indirect export route (path 4 in Figure 5.1) of this water mass towards the Irminger Sea (e.g., Lavender et al., 2000; Pickart et al., 2003; Stramma et al., 2004; Bower et al., 2009; Holliday et al., 2009; Lozier et al., 2013).

The Lagrangian analysis performed in chapter 3 by using the output of an idealized model indicated that an eddy-driven transport of dense water towards the boundary exists and that its presence affects the export timescales of LSW (Figure 3.2b, Figure 3.13). This was confirmed in the Lagrangian analysis performed in an eddy-permitting global ocean model in chapter 4 (Figure 4.5b, Figure 4.10). The results presented in these chap-

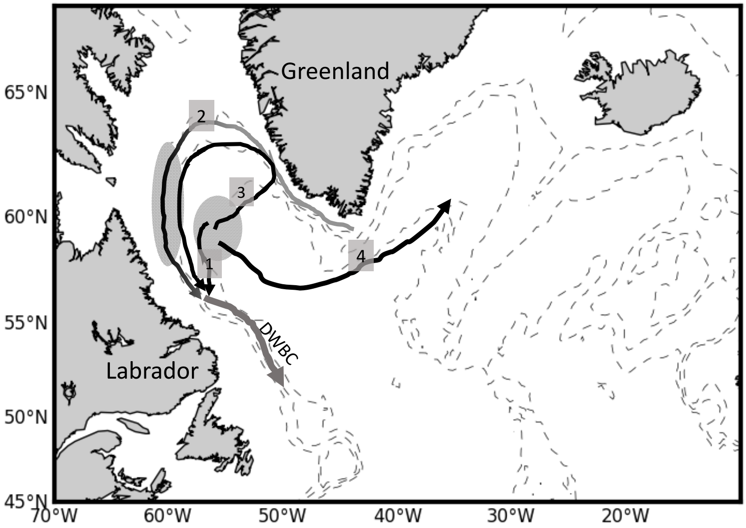

Figure 5.1: Schematic of the pathways of the LSW (based on Palter et al., 2008; Rhein et al., 2017; Georgiou et al., 2020): (1) direct entrainment of the LSW in the boundary current, (2) LSW formation within the boundary current itself, (3) eddy-driven LSW transport from the interior towards the west coast of Greenland and (4) mid-depth recirculation of the LSW towards the Irminger Sea. Shaded areas indicate the location of convection regions in the Labrador Sea. Dashed grey contours outline the bathymetry (contour interval is 1000 m starting from the isobath of 1000 m). Bathymetry data from ETOPO1 (Amante and Eakins, 2009).

ters suggest that the link between the LSW formation and AMOC variability might be difficult to capture in short-term observations such as the OSNAP array (Holliday et al., 2018; Lozier et al., 2019) since the densest water masses tend to follow the indirect route (path 3 in Figure 5.1), resulting in longer timescales to exit the Labrador Sea (section 3.7 and section 4.5). The latter suggests that the boundary current system, its stability, and most importantly the boundary-interior exchanges play an important role for the Labrador Sea dynamics.

The boundary current system encircling the Labrador Sea carries buoyant waters in its upper layer while at depth denser waters and overflow waters from the Nordic Seas are found (e.g., Holliday et al., 2007). The Labrador Current and West Greenland Current carry fresh waters from the Artic and runoff from the Greenland ice shelf flowing along the shelf and shelf break (Clarke and Gascard, 1983; Dickson et al., 2007; Yashayaev and Clarke, 2008). Moreover, the warm and salty Irminger Water flows cyclonically at mid-depths along the continental slope (Cuny et al., 2002; Myers et al., 2007). A topographic narrowing at the west coast of Greenland makes the boundary current unstable and large, warm anticyclonic eddies known as Irminger Rings (IRs) are shed (e.g., Lilly et al., 2003; Katsman et al., 2004, Figure 2.1c). These eddies are known to advect buoyant water from the boundary into the interior (Figure 2.5), playing an important role in restratifying the water column in the interior of the Labrador Sea after convection events during winter (Gelderloos et al., 2011; de Jong et al., 2016). It is the lateral exchange between the boundary current and the interior together with the surface fluxes that sustain a balance of the heat and salt budget in the Labrador Sea (section 2.2.3, Lilly et al., 2003; de Jong et al., 2016).

Under a scenario of global warming it is important to understand how the ocean circulation will respond. The response of the Labrador Sea to changes in climate has been investigated in many studies (e.g., Böning et al., 2016; Jones et al., 2018; Garcia-Quintana et al., 2019). For instance, a decrease of the winter heat loss from the ocean to the atmosphere in the Labrador Sea could lead to a stronger stratification in the interior, which in turn would make conditions less favorable for deep convection to occur (Marshall and Schott, 1999). This is a qualitative view on the implications of a changing climate, taking into account the complex relation between the intra-basin processes and the AMOC variability. The results presented in chapter 3 and chapter 4 reveal a complex three-dimensional view of the LSW export from the interior, rather than a homogeneous lateral spreading and entrainment of the LSW into the boundary current (Khatiwala and Visbeck, 2000; Bower et al., 2009, 2011; Gary et al., 2012). In particular, it was shown that the latter is strongly governed by the combination of the LSW density and depth that it acquires after its formation in the interior, and also on the boundary current stratification along the basin's perimeter (Figure 4.11). In a changing climate, it remains unclear to which degree these scenarios might alter the properties of the LSW, its export routes and the associated timescales, and therefore the AMOC strength.

The aim of this study is to assess the response of the pathways that the water masses follow prior to exiting the Labrador Sea to changes in the surface heat flux. Towards this goal, two sensitivity Lagrangian simulations are performed in an idealized model for the Labrador Sea. The use of an idealized configuration of a high-resolution regional model helps to isolate specific processes and provides helpful insights in to the nature of the changes in each of the sensitivity simulations. In particular, we use two sensitivity simulations reflecting a milder and colder winter climate state (chapter 2). In the course of this chapter, we investigate the response of the pathways found in chapter 3 and chapter 4, the water mass transformation, the net overturning and the boundary-interior exchange to changing forcing conditions.

This chapter is organized as follows: the sensitivity simulations and a description of the Lagrangian approach are introduced in section 5.2. The resulting convection and eddy field in the sensitivity simulations is then compared to the one found in the reference simulation (section 5.3). Next, we explore the response of the pathways (section 5.4), the water mass transformation (section 5.5), the net overturning (section 5.6) and the boundary-interior exchange (section 5.7) to changes in the winter surface heat loss. Last, section 5.8 covers the discussion and conclusions.

5.2. Data and Methods

The model configuration used in this chapter is the same as described in section 2.2; an idealized configuration of the MITgcm (Marshall et al., 1997) for the Labrador Sea. To investigate the sensitivity of the pathways found in the idealized model in chapter 3 (Figure 3.2b), which were confirmed to exist also in the Lagrangian analysis using the output data from a realistic ocean model (MOM, chapter 4), we now perform a Lagrangian analysis using the output data also from the two sensitivity simulations described in section 2.2.2. In particular, we use the data of the COLD and WARM simulations in which the winter surface heat loss is increased and decreased by 50% respectively with respect to the one applied in REF (Figure 5.2). Note that in these simulations the effects of salinity are not incorporated and that a linear equation of state is used taking into account only temperature variations for simplicity.

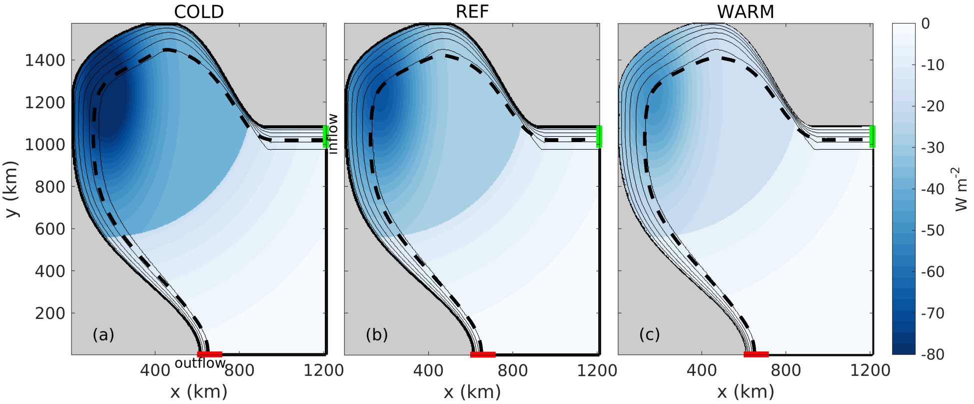

Figure 5.2: Annual mean surface heat flux applied to the model in (a) COLD, (b) REF and (c) WARM simulation (see section 2.2.2 for details on the simulations). Q< 0 indicates cooling of the sea surface (Q in W m^{-2}). Thin black contours outline the bathymetry, the contour interval is 500 m starting from the isobath of 500 m. The thick black dashed line shows the 18 Sv barotropic streamfunction (Ψ_b) in each simulation which is used to distinguish the boundary current and the interior of the basin (see also section 3.2.1 and section 3.3).

The offline Lagrangian tool Connectivity Modeling System (CMS, Paris et al., 2013) is used to trace the pathways of the water masses by means of Lagrangian particles. In particular, we use the three dimensional velocity field from the last six years of the sensitivity simulations (i.e. model years 15-20) to track the Lagrangian particles. The release procedure of the particles is the same as in REF (section 3.2.2). Particles are released at the outflow (red lines in Figure 5.2) with a particle resolution of 1 km in the zonal direction and 50 m in the vertical direction. The particles are released every 2 days over a period of one year and are traced backwards in time for 6 years only when the meridional velocity at the outflow is negative (southward). Upon release, a volume transport is assigned to each particle by multiplying the meridional velocity by the area of the grid cell in which the particle is released (Döös, 1995; Ypma et al., 2019). This transport is conserved along the trajectory (van Sebille et al., 2018).

5.3. Response of Labrador Sea dynamics

Before analyzing the trajectories of the particles, we revisit the resulting properties of convection and eddy field in the simulations where the surface heat flux is changed (i.e. COLD and WARM) as investigated in section 2.4. Furthermore, we investigate whether these changes affect the thermohaline properties of the product of convection and also the strength of the boundary current.

As shown in section 2.4, both the convection and the eddy field are affected by the changes in the surface forcing (Figure 2.9). However, the response of the MLD is not proportional to changes in the heat flux as shown in chapter 2. Although the applied surface forcing has been changed in COLD and WARM by the same percentage (by ±50% with respect to the reference simulation), it results in changes of +25% (Figure 2.9a,c) and -45% (Figure 2.9b,d) in the maximum depth of the winter mixed layer. This asymmetry can be partly attributed to the stratification, which increases at larger depths, and partly to the changes in the baroclinicity of the boundary current and the associated lateral eddy heat fluxes. As shown in section 2.4, the increase (decrease) in the eddy heat advection into the interior are not simply proportional to the increase (decrease) in the applied heat loss in COLD (WARM) either. It is the combination of surface heat fluxes and lateral eddy fluxes that regulates the properties of the convection.

Under the scenario of a stronger (weaker) surface winter heat loss, the winter mixed layer deepens (shallows) and the convection region becomes wider (narrower), while the density gradient between the interior and the boundary current increases (decreases). The increase (decrease) in the horizontal density gradient in COLD (WARM) results in a faster (slower) boundary current than in REF (Figure 5.3). In this idealized model, the mean alongshore speed of the boundary current increases by 20% in COLD and decreases by 10% in WARM with respect to REF.

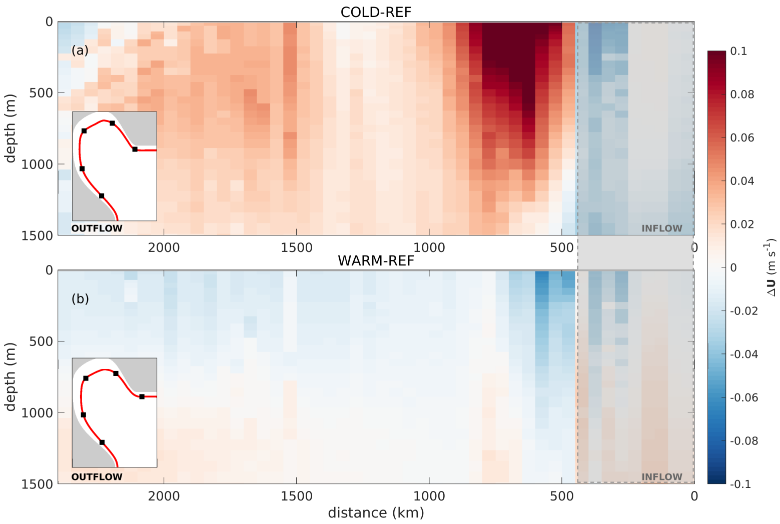

Figure 5.3: Anomaly from REF simulation of the 5-year mean speed ($\Delta\mathbf{U}$, in m s^{-1}) of the boundary current for (a) COLD and (b) WARM as a function of distance from the inflow and depth. Black squares in the inset figures mark distances every 500 km. Values are horizontally averaged over the width of the boundary current (onshore of Ψ_b=18 Sv, see red line in insets). Note that within the first 500 km (grey shaded area) the boundary current might experiences some spurious changes due to the open boundary conditions.

To identify the properties of the convected water (characterized as being weakly stratified in the vertical) in each simulation, we use the threshold of small potential vorticity (PV) following Talley and McCartney (1982). The potential vorticity is defined as PV= $-(f/\rho)(\partial\rho/\partial z)$; where f is the Coriolis parameter and ρ the density, where in our simulations density is associated with temperature variations only. In particular, we define the isopycnals that bound the convected water as those with PV<$4{\cdot}10^{-12}$ $(\mathrm{m\,s})^{-1}$. A mean hydrographic section across the model domain in late spring (May, Figure 5.4b) shows that in the REF simulation the convected water is found between the isopycnals of $\sigma=\rho$-1000= 28.32–28.40 kg m^{-3}. In COLD the product of convection resulting from the stronger surface winter heat loss is denser than in REF and is found between σ= 28.36–28.42 kg m^{-3} (Figure 5.4a). As expected, the opposite holds for the WARM simulation since the weaker winter heat loss yields a lighter product of convection with σ= 28.30–28.38 kg m^{-3} (Figure 5.4c).

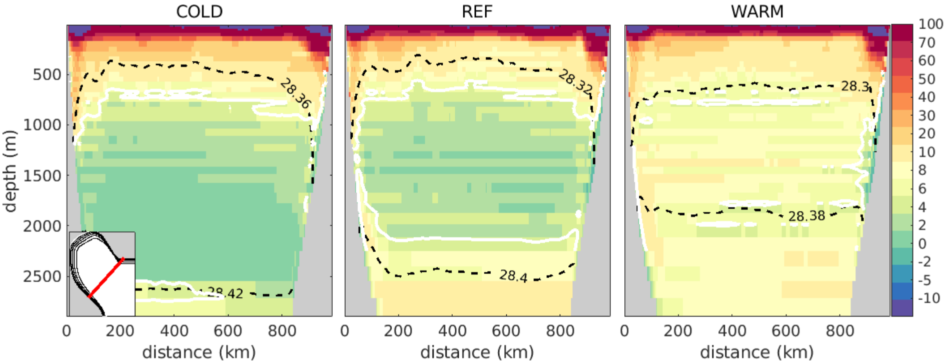

Figure 5.4: Late spring (May) mean PV (shading, in (m s)$^{-1}$) over a section indicated by the red line in the inset figure in (a), for (a) COLD, (b) REF and (c) WARM. White lines denote the $4{\cdot}10^{-12}$ (m s)$^{-1}$ contour of the PV. Black dashed contours denote the density range of the convected water ($\sigma=\rho$-1000, in kg m^{-3}). Values are averaged over years 16-20. The section is plotted against the distance from the west coast (km).

In chapter 3 and chapter 4 it was shown that there is an eddy-driven transport of the convected water towards the boundary and that its entrainment strongly depends on the local properties of the boundary current and of the convected waters themselves. Therefore, it is likely that the above-mentioned changes in the eddy field, thus the lateral eddy fluxes (Figure 2.10), the properties of the boundary current (Figure 5.3) as well as the properties of convection (Figure 5.4) will affect the pathways that the water masses follow prior to exiting the domain; the more and more eddies detach from the boundary current the more transport of convected water is expected towards the boundary current. However, this is only valid when the properties of the convected water match that of the boundary current at the location of entrainment.

5.4. Response of the upstream pathways of the water masses

Next we investigate how changes in the applied surface heat flux affect the pathways of the water masses prior to exiting the model domain. To do so, Lagrangian analyses are performed by using the output data from the COLD and WARM simulations (section 5.2) and are compared to the findings of the Lagrangian analysis in REF (chapter 3).

Particle density maps highlight the preferred paths of the particles in each simulation (Figure 5.5). These maps are constructed by, for each grid cell, summing the volume transport assigned to each particle that passes through this grid cell along its trajectory, and dividing this by the total transport carried by the particles (Ypma et al., 2019). In all the simulations, the highest particle density occurs along the boundary current (dark shading in Figure 5.5), which indicates that most of the particles are found somewhere within the boundary current during their lifetime. Enhanced values of the particle density are found also in the interior at the northwestern side of the basin, along the west coast of Greenland, in all the simulations. This reveals that the boundary current-interior exchange highlighted in chapter 3 for the REF simulation, is also present in COLD and WARM simulations (Figure 5.5). However, the density plot for the COLD simulation (Figure 5.5a) suggests that in this case this exchange is weaker than in the rest of the simulations. This is surprising at first glance since one would expect the deflection of more particles from the boundary current towards the interior as a result of the increase of the EKE in COLD along the Greenland coast compared to REF (Figure 2.9c). A possible explanation of this discrepancy is that in COLD the resulting lateral eddy heat flux peaks farther north than in REF (Figure 2.10a-b) suggesting that the eddies move towards the interior slightly differently in these two simulations.

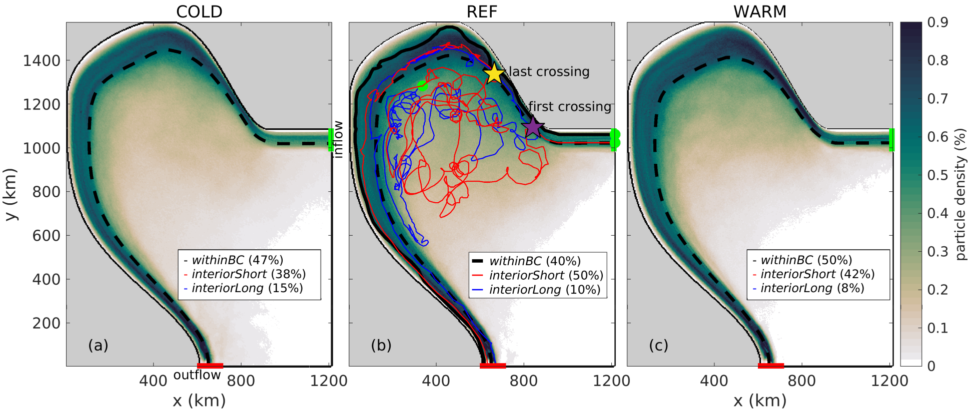

Figure 5.5: Particle density map of particles released at the outflow (at y= 3.75 km, red line) and traced backwards in time for (a) COLD, (b) REF and (c) WARM. The black dashed line shows the 18 Sv barotropic streamfunction (Ψ_b) which is used to distinguish the boundary current from the interior for each simulation. Also shown in (b) are example trajectories of a particle following the boundary current (*withinBC*, black line), a particle crossing into the interior (*interiorShort*, red line) and a particle that does not leave the basin during the 6-year simulation (*interiorLong*, blue line). The purple (yellow) star indicates the location where the example *interiorShort* particle crosses the 18 Sv barotropic streamfunction (dashed line) for the first (last) time. Green circles indicate the location of the particles at the end of the backward advection time (i.e. at t = 6 years). The percentage of the total volume transport carried by each pathway is given in the legend of each panel.

The classification of the particles advected in the Lagrangian analysis for each simulation is done by following the procedure discussed in section 3.3; we define a particle as being in the interior when it is offshore of the 18 Sv contour line of the 5-year mean barotropic streamfunction in each simulation (Ψ_b, black dashed line in Figure 5.5). Note that in each simulation the location of this contour line of Ψ_b differs as the speed of the boundary current changes (Figure 5.3). As in section 3.3, the *wholeLoop* particles (i.e., particles that within 6 years of backwards advection reach the inflow) are subdivided in two categories: particles that cross the contour line of Ψ_b into the interior at some location (hereinafter, *interiorShort* particles, red trajectory in Figure 5.5b) and particles that never cross this contour line and thus never leave the boundary current (hereinafter, *withinBC* particles, black trajectory in Figure 5.5b). Recall that the particles that are still in the domain at the end of the 6 year simulation are referred to as *interiorLong* particles (blue trajectory in Figure 5.5b).

It appears that the division of particles over these three categories does not display a linear response to changes in the wintertime heat loss over the Labrador Sea (see legend in Figure 5.5). In both COLD and WARM the volume transport carried by the *withinBC* particles increases by ~10% compared to REF, while the volume transport associated with the *interiorShort* particles reduces by 10%. This indicates that the boundary-interior exchange is less prominent in both COLD and WARM than in REF. The reduction of the number of *interiorShort* particles, and thus of the boundary-interior exchange in WARM was expected since the EKE is also weaker (Figure 2.9d). In COLD, both the EKE and the lateral eddy heat fluxes increase in comparison to REF (Figure 2.9c and Figure 2.10a) and hence one would also expect an increase in the fraction of *interiorShort* particles compared to REF. As previously discussed, it is possible that the combined effect of a faster current (Figure 5.3a) and a more northward propagation of the eddies in COLD (Figure 2.10a) compared to REF, creates a constraint for the particles to leave the boundary current.

Furthermore, the volume transport associated with the *interiorLong* particles increases by 5% in COLD and decreases by 2% in WARM compared to REF. That means that under the scenario of a stronger surface winter heat loss in COLD, more particles are 'trapped' in the interior of the basin within 6 years of advection period and the opposite holds in WARM.

5.5. Response of the water mass transformation

In section 3.5 we identified the locations where the water masses last change their properties by means of the local subduction rate. Here, we investigate the response of the subduction rate and of the pathways that the particles follow after their subduction to changes in the surface heat flux and how their properties are affected.

The results discussed in section 3.5 for the REF simulation already revealed that the subduction of waters exiting the domain along the *withinBC* route mainly occurs in the western part of the Labrador Sea (Figure 5.6b), while large subduction velocities of the particles following the *interiorShort* route are found in the west, close to the edge of the boundary current (Figure 5.6d). For the REF simulation, the total subduction amounts to 1.9 Sv and 3.7 Sv for the *withinBC* and *interiorShort* particles, respectively, highlighting the importance of water mass transformation in the interior (Figure 5.7b). Qualitatively, the same view emerges from the two sensitivity simulations (COLD and WARM, Figure 5.6 and Figure 5.7a,c).

Similarly to REF, the subduction of the *withinBC* particles in the COLD and WARM simulations occurs in the western part of the Labrador Sea (Figure 5.6b-c). Figure 5.6(d,f), shows that the subduction velocities of the *interiorShort* particles are higher closer to the region where the heat loss is maximum in the interior and also in the boundary region on the Labrador side (Figure 5.6d-f).

Marshall et al. (1993) suggested that changes in the mixed layer depths and surface buoyancy fluxes directly affect the subduction rate. Based on the changes in the surface forcing only, one would expect that the subduction rate will increase (decrease) in COLD (WARM). Indeed, in WARM the total subduction of *withinBC* and *interiorShort* particles is reduced by ~20% compared to the REF in response to the weaker winter surface heat loss applied in this simulation (Figure 5.7b-c). However, also in COLD the total subduction of *withinBC* and *interiorShort* particles is 20% and 14% lower than in REF, respectively (Figure 5.7a-b). The reduction in the subduction rate associated to the *withinBC* particles can be attributed to the fact that the boundary current in COLD is faster than in REF (Figure 5.3a). Therefore, the residence time of these particles in the mean flow is shorter and any water mass transformation due to direct surface heat loss might be less (Ypma et al., 2020a). A possible explanation for the reduction in the subduction rate associated to the *interiorShort* particles in COLD could be that the amount of *interiorShort* particles is less than in REF. Thus, a one-to-one comparison of the subduction rate in the three simulations is not straightforward. However, it is clear that the subduction rate does not simply scale with the changes to the applied heat flux.

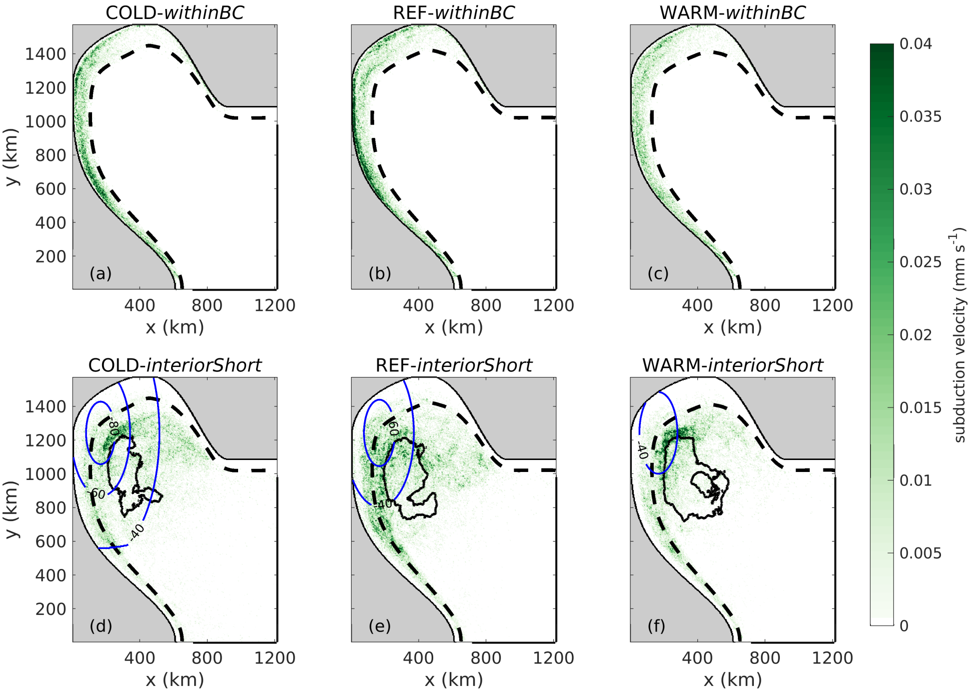

Figure 5.6: Subduction velocity for *withinBC* (upper panels) and *interiorShort* particles (lower panels) in (a,d) COLD, (b,e) REF and (c,f) WARM. The black dashed line shows the 18 Sv barotropic streamfunction that is used to separate the particle pathways in each simulation. Blue contours in the lower panels indicate the annual mean surface heat flux in each simulation (in W m^{-2}, the contour interval is 20 W m^{-2} starting from -40 W m^{-2}); negative values indicate cooling of the sea surface. Black contours encompass 60% of the maximum winter MLD.

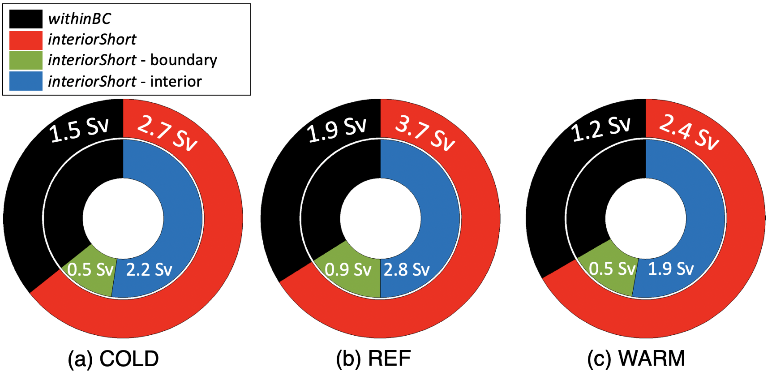

Figure 5.7: Subduction rate (in Sv) as obtained from the *withinBC* (black) and *interiorShort* (red) particles in (a) COLD, (b) REF and (c) WARM simulation. Note that the subduction rate for the *interiorShort* particles is split in the subduction rate for the particles that subduct within the boundary (green, onshore of $\Psi_b = 18$ Sv) and in the interior of the basin (blue, offshore of $\Psi_b = 18$ Sv).

It was also shown in the Lagrangian analysis in the realistic MOM model (section 4.4.2) that after subduction particles tend to either travel towards the west coast of Greenland or towards the Labrador side of the basin before re-entering the boundary current (i.e., WG-path and LC-path, Figure 4.8). Here, we investigate how the changes in the surface forcing conditions affect these two pathways by following a similar procedure as in section 4.4; in each simulation we split the *interiorShort* particles that subduct in the interior of the basin based on their proximity to the high EKE region near Greenland. To this end, we define a boundary in the northeast (blue line in Figure 5.8a), placed such that EKE<200 $\text{cm}^2\ \text{s}^{-2}$ southwest of it. Particles that at some time after subduction cross this line from southwest to northeast are classified as following the WG-path; all other particles are considered to follow the LC-path.

To visualize the preferred routes, Figure 5.8a-b shows maps of the particle density of these two pathways for REF. The density maps for COLD and WARM display a similar pattern. Therefore only the particle density maps for the REF simulation are shown for simplicity. For the WG-path, the particle density is significantly higher at the west coast of Greenland and is co-located with the region of enhanced EKE (black contours in Figure 5.8a). This indicates that, as in the realistic MOM model (chapter 4), this path is regulated by the local eddy activity. Moreover, the LC-path (Figure 5.8b) confirms the existence of the direct export route of newly-formed water masses from the interior of the Labrador Sea to the boundary current at the Labrador side in the idealized model (see section 4.4). In REF, the volume transport of the *interiorShort* particles that subduct in the interior of the basin amounts to 2.8 Sv (blue in Figure 5.7b). It is found that 60% of the transport carried by these particles follows the indirect WG-path (1.7 Sv), while the remaining 40% (1.1 Sv) follows the direct LC-path to exit the domain (Figure 5.8c).

The distribution of transport over these two routes that the newly-formed waters follow to leave the interior of the basin differs in the sensitivity simulations (Figure 5.8c). In a colder regime (COLD simulation), 80% of the volume transport of the particles that subduct in the interior of the basin follow the WG-path and only 20% follow the direct

LC-path. As shown in chapter 2, the region where the eddies are shed is characterized by a strong shear in the velocity field around the eddies (Figure 2.5), which in turn steers the convected water towards the West Greenland coast (Figure 2.7). Since the eddy activity is stronger in COLD than in REF (Figure 2.9c) at this region, an enhanced offshore movement of eddies may foster more dense waters to entrain into the boundary current. Therefore, the particles in COLD tend to follow the WG-path rather than the direct LC-path after they subduct. In contrast, in a warmer regime (WARM simulation) the weakening of the EKE (Figure 2.9d) results in a reduction of the advection of the convected water towards the west coast of Greenland; in this simulation, 46% of the total transport of the *interiorShort* particles that subduct in the interior follows the indirect WG-path (0.9 Sv) and 54% (1.0 Sv) follows the direct LC-path (Figure 5.8c).

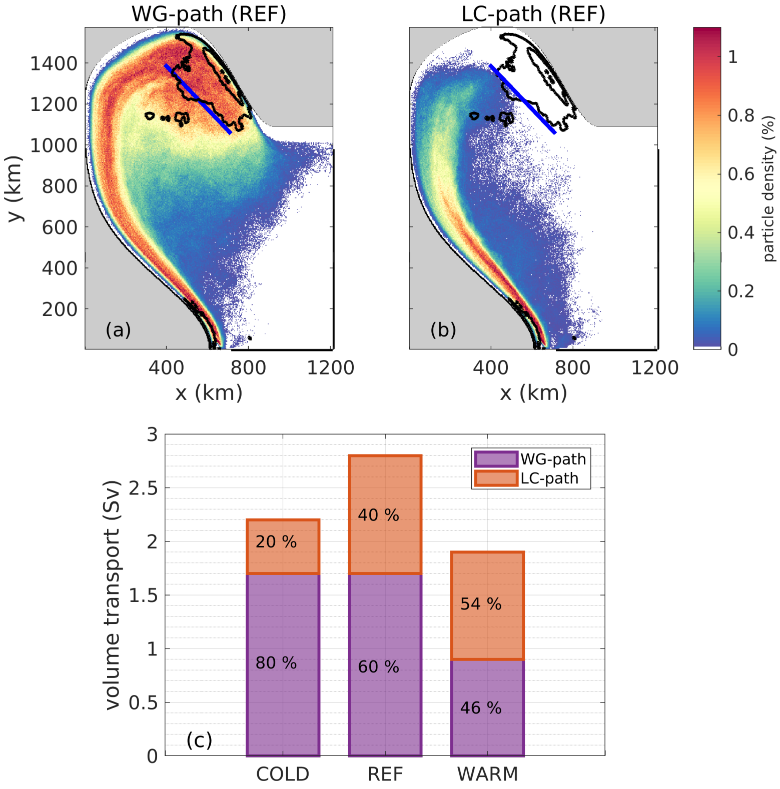

Figure 5.8: (a-b) Particle density map of particles that subduct in the interior of the basin from their subduction location to the outflow in the REF simulation. The set of particles is split by evaluating if they (a) travel towards the west coast of Greenland (WG-path) by crossing the blue line in (a) from southwest to northeast or (b) travel towards the Labrador coast (LC-path). Northeast of the blue line in (a) the EKE is higher than 200 cm^2 s^{-2}; black contours in (a) indicate the annual mean EKE (contour interval is 200 cm^2 s^{-2}, starting from the contour line of 200 cm^2 s^{-2}). (c) Volume transport carried by the particles following the WG-path (purple bars) and LC-path (orange bars) in COLD, REF and WARM.

It has been shown in chapter 4, by using a realistic model (i.e., MOM) that the subduction of the *withinBC* along the boundary current results in lighter waters than the subduction of the particles in the interior (Figure 4.6), and that the majority of densest waters formed in the interior follow the WG-path. Here, we firstly investigate whether this view also holds for the REF simulation in this idealized model and secondly whether it is affected by changes in the surface forcing. To do so, we analyze the volume transport at the outflow of the domain carried by the *withinBC* particles that subduct along the boundary current (Figure 5.9a) and by the *interiorShort* particles that subduct in the interior of the basin and then follow the WG-path (Figure 5.9b) or the LC-path (Figure 5.9c). The transports are binned by 0.02 kg m^{-3} in density space.

It is evident that the transformation of the *withinBC* particles that occurs within the boundary current mainly results in a lighter product (Figure 5.9a) than that of the particles that subduct in the interior of the basin (Figure 5.9b-c) for all three simulations. In REF the maximum of the volume transport carried by the subducted *withinBC* particles is found at a density of σ=28.20 kg m^{-3} (black bars in Figure 5.9a). The volume transport of the particles that subduct in the interior of the basin and then follow either the WG-path or the LC-path to leave the domain is found to peak at a density of σ=28.36 kg m^{-3} (black bars in Figure 5.9b) and of σ=28.34 kg m^{-3} (black bars in Figure 5.9c), respectively. Although the bulk of the particles that follow both the WG-path and LC-path is associated with dense waters (σ>28.28 kg m^{-3}) exiting the basin, the LC-path is the preferred route mainly for lighter waters (σ<28.38 kg m^{-3}) that are formed in the interior of the basin.

Under the scenario of a stronger (weaker) surface winter heat loss in COLD (WARM), the maximum of the volume transport carried by the subducted *withinBC* particles is found at a density of σ=28.26 kg m^{-3} (σ=28.18 kg m^{-3}, see blue and red bars in Figure 5.9a) which is at a denser (lighter) density class than in REF. Notably, the volume transport carried by this subset of particles in REF and COLD displays a secondary maximum at a higher density (i.e., σ=28.36 kg m^{-3} and σ=28.42 kg m^{-3}, respectively). The fact that there is no significant transport at higher densities in WARM, suggests that the applied surface forcing in this simulation does not favor the formation of denser waters within the boundary current. Particles that subduct in the interior and follow the WG-path or the LC-path display a similar behavior to the response of the *withinBC* particles to changes in the surface forcing. In a colder (warmer) regime the majority of the particles that follow these two paths is found at a denser (lighter) density class than in REF (see blue and red bars in Figure 5.9b-c). In particular the maximum volume transport carried by these particles is found at a density class of σ=28.40 kg m^{-3} and σ=28.32 kg m^{-3} in COLD and WARM, respectively.

From the above, we can conclude that the transformation both in the boundary current and in the interior is affected by the stronger winter heat loss, since it results in denser waters in COLD than in REF, whereas the opposite holds in WARM. This is in line with expectations, since as shown in section 5.3 a stronger (weaker) winter heat loss in COLD (WARM) results in enhanced (reduced) buoyancy loss over the basin which in turn leads to the production of denser (lighter) water masses in the Labrador Sea (Figure 5.4).

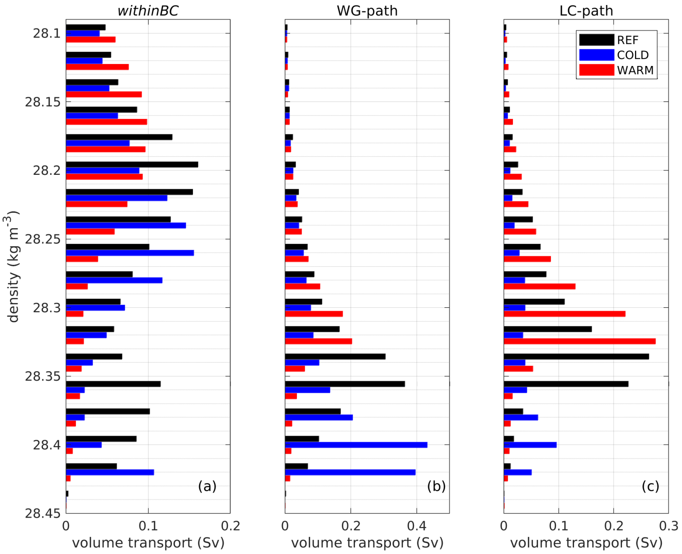

Figure 5.9: Volume transport at the outflow of the domain binned by 0.02 kg m^{-3} in density space split in transport carried by (a) the *withinBC* particles that subduct along the boundary current and (b-c) the *interiorShort* particles that subducted in the interior of the basin and then travel towards (b) the vicinity of the west coast of Greenland (WG-path) and (c) the Labrador side (LC-path) in the three simulations REF (black), COLD (blue) and WARM (red). Note the different scale for the volume transport on the horizontal axis of each panel.

5.6. Response of the local overturning

In section 3.4, it has been shown that the relative importance of the different pathways for the overturning becomes apparent in density space; in REF, 60% of the maximum overturning is related to the transport carried by the *interiorShort* particles and only 40% by the *withinBC* particles (Figure 3.7d). Building on this view, we investigate how the relative contribution of the different pathways to this net overturning is affected under the scenario of changes in the surface winter heat loss (COLD and WARM).

To this end, for each simulation, we calculate the Lagrangian overturning in density space for each pathway, by taking the difference between the summed volume transport carried by all particles in a certain density bin at the inflow and at the outflow. The cumulative transport as a function of density (from top to bottom) are shown in Figure 5.10a. Note that the outcomes for REF are already shown in Figure 3.7d and that in this section we repeat the procedure for COLD and WARM as well. As discussed in section 3.4, only the transports carried by the *withinBC* and *interiorShort* particles can be taken into account for the total mean Lagrangian overturning estimate.

For REF the maximum overturning in density space obtained in this way is found at σ =28.32 kg m^{-3} and amounts to 5.5 Sv (black line in Figure 5.10a). Moreover, a secondary peak of 4.1 Sv in the total Lagrangian overturning at σ = 28.16 kg m^{-3} is present, which, as shown in section 3.4, can be attributed to the transformation of the *withinBC* particles (see section 3.4.3). Under the scenario of a stronger or weaker surface winter heat loss in COLD and WARM respectively, the overturning signal is reduced by 15% and

40%, respectively from the calculation for REF and amounts to 4.8 Sv and 3.4 Sv, respectively (blue and red lines in Figure 5.10a). This reveals that the overturning in density space displays a non-linear response to the applied surface heat loss in contrast with the view which emerged from section 2.4.2 for the overturning in depth space (Figure 2.11a). However, the maximum of the overturning in COLD is found in denser layers than in REF (at a density of σ =28.36 kg m^{-3}), while in WARM it is found in lighter layers (at σ =28.26 kg m^{-3}). This is not surprising since the water mass transformation in COLD (WARM) results in denser (lighter) water masses than in REF (Figure 5.9a): with a stronger heat loss, the overturning in density space peaks in a heavier density class.

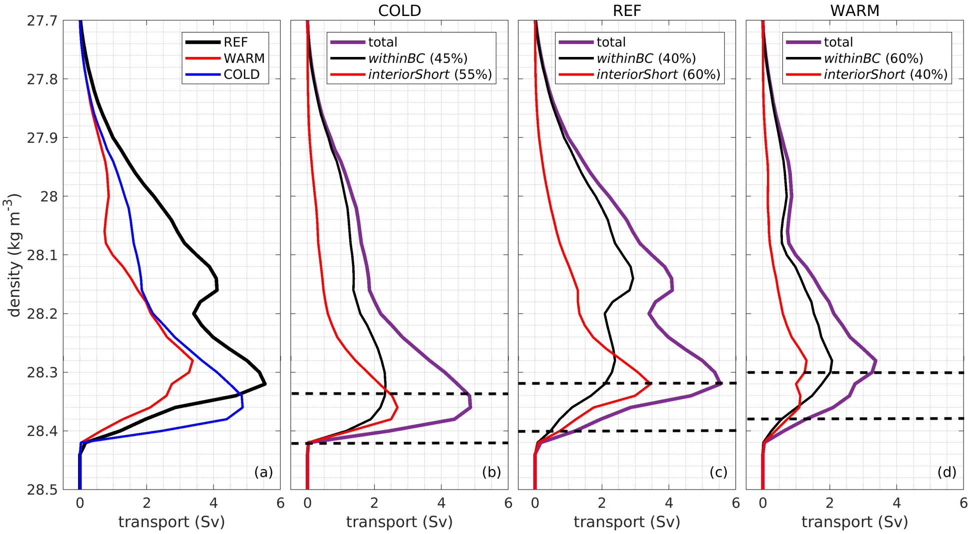

Figure 5.10: (a) Cumulative total overturning in density space for REF (black lines), COLD (blue lines) and WARM (red lines). Note that this is estimated from the particle transports and not the Eulerian velocity fields. (b-d) Overturning in density space for (b) COLD, (c) REF and (d) WARM split between the contributions from the *withinBC* (black lines), *interiorShort* (red lines) particles and their sum (Lagrangian mean, purple line). The percentage of the *withinBC* and *interiorShort* particles that describes the maximum total overturning estimate is indicated in the legend of each panel. Black dashed lines in (b-d) denote the density range of convected water for each simulation.

When the contribution of the transport carried by each pathway to the net overturning in density space is considered, it was shown in section 3.4 that in the REF simulation 60% of the maximum overturning (at σ = 28.32 kg m^{-3}) can be attributed to the *interiorShort* particles and 40% to the *withinBC* particles (Figure 5.10c). It appears that the changes in the surface forcing (COLD and WARM) affect the relative importance of the different pathways on the overturning. In COLD, the maximum overturning (at σ = 28.36 kg m^{-3}) is still by 55% associated with the *interiorShort* particles and by 45% with the *withinBC* particles (Figure 5.10b). It is evident that in a colder regime, the transformation of the *withinBC* results in denser water masses than in REF as the stratification along the boundary current is weaker due to the stronger heat loss, leading to a denser product during convection events (Figure 5.4b). Therefore, in COLD there is not a clear secondary peak in the total overturning at lighter density class (Figure 5.10b) as seen in REF. In WARM, the view is different; only 40% of the maximum overturning (at σ = 28.26 kg m^{-3}, Figure 5.10d) can be attributed to the *interiorShort* particles and 60% to the *withinBC* particles. Moreover, a secondary peak of 0.9 Sv in the total overturning at σ = 28.00 kg m^{-3} (Figure 5.10c) is again associated to the transformation of the *withinBC* particles.

Taken together, when a stronger (weaker) surface winter heat loss is applied over the basin, the maximum signal of the overturning occurs at a denser (lighter) layer than the one found in a normal winter state of the Labrador Sea (Figure 5.10a). However, the strength of the maximum signal of the overturning is weaker in both the COLD and WARM scenarios compared to REF. Essentially, in WARM the 50% reduction in the winter surface heat loss which limits the depth of convection (Figure 2.9b,d), also increases the restratification process after convection events. This process restricts the production of denser water mass during convection as in REF and COLD and in turn the contribution of the *interiorShort* particles to the net overturning is reduced compared to REF. In COLD, it is as yet unclear how to interpret the weakening of the overturning strength with respect to REF. As in WARM, the contribution of the *interiorShort* particles to the net overturning is also reduced in COLD compared to REF. A possible explanation for this change could be the response of the lateral boundary-interior exchange to changes in the surface forcing and this is discussed in the following section.

5.7. Response of the lateral boundary-interior exchange

To explore the response of the lateral exchange between the boundary current and the interior discussed in section 3.6 and section 4.6 to changes in surface heat flux, we next investigate the locations where the *interiorShort* particles enter and leave the interior of the domain and the properties of the particles at these locations. The first (last) crossing of a particle is defined as the location where it crosses the 18 Sv contour line of the barotropic streamfunction (Ψ_b) for the first (last) time after entering the domain (see purple and yellow stars in the example trajectory shown in Figure 5.5b) in the sensitivity simulations and we compare the results to the associated findings for REF (section 3.6).

In REF, the peak in first crossings (black dashed line in Figure 5.11a-b) that is found upstream of the peak in EKE along the boundary (black thin line Figure 5.11a-b) is associated with the eddy activity in this region (see more details in section 3.6). This also holds for COLD and WARM (compare dashed and thin lines in Figure 5.11a-b). However, the total number of first crossings in COLD and WARM is reduced by 50% and 35% respectively compared to REF. This shows that the lateral exchange between the boundary current and the interior is weaker in the colder and in the warmer regime (COLD and WARM, respectively). The reduction in the number of first crossings in COLD is possibly related to the fact that in the colder regime, the density gradient between the boundary current and the interior increases and this results in a faster boundary current (Figure 5.3a). Apparently, the particles tend to follow the fast mean flow within the boundary current rather than detach and enter into the interior. The reduction in the number of first crossings in WARM can be attributed to the weakening of EKE near the West Greenland coast (thin red line in Figure 5.11b) which is expected to limit the boundary-interior exchanges.

The location where most of the *interiorShort* particles in REF re-enter the boundary current (black solid line in Figure 5.11a-b) coincides with the region of enhanced EKE (thin black line in Figure 5.11a-b and Figure 3.10a). Similarly, the last crossings of the *interiorLong* particles are mostly found at the region of high EKE (Figure 3.10a). The view that both the *interiorShort* and *interiorLong* particles after their excursion in the interior re-enter the boundary current at the region of high EKE still holds in COLD (blue solid line in Figure 5.11a) and WARM (red solid line in Figure 5.11b). This suggests that the enhanced EKE facilitates exchanges from the interior towards the boundary current no matter the changes in the applied forcing in the model. In turn, this confirms that the spreading of dense waters formed in the interior towards the boundary coast near the west coast of Greenland is mainly driven by the eddy field that is present there (section 3.6 and section 4.6).

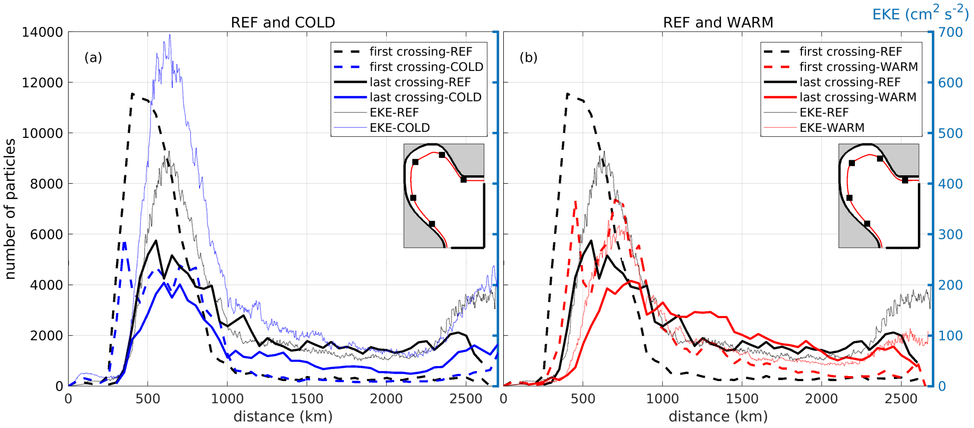

Figure 5.11: Number of particles at the first (dashed line) and last (solid lines) crossings for the *interiorShort* particles for (a) COLD (blue lines) and (b) WARM (red lines) together with the values for REF (black lines in each panel). Values are binned over segments of 50 km in alongshore direction (see inset, red circles mark distances every 500 km). Thin lines show the EKE as a function of distance from the inflow.

An interesting finding of the Lagrangian analysis in the realistic model (section 4.6) was that the entrainment of convected water can only take place where its density and depth match the local properties of the boundary current (Figure 4.11). Here, we explore if this is also evident in the idealized model. Furthermore, since the density of the convected waters changes with varying the surface heat flux and the density structure of the boundary current changes as well (Figure 5.4), we investigate how this affects the re-entry of these dense waters in the boundary current. To do so, we analyze the re-entry of the *interiorShort* particles in the boundary current after subduction in the interior of the basin (i.e. the WG-LC- paths). In particular, we investigate where (considering depth and alongshore direction) these particles cross the Ψ_b for the last time (our definition of re-entry of the boundary current) in the three idealized simulations.

It appears that in all three simulations (REF, COLD and WARM) most WG-path particles (purple shading in Figure 5.12a,c,e) re-enter the boundary current at the region of enhanced EKE (grey vertical lines in Figure 5.12a,c,e). In particular, for REF this entrain-

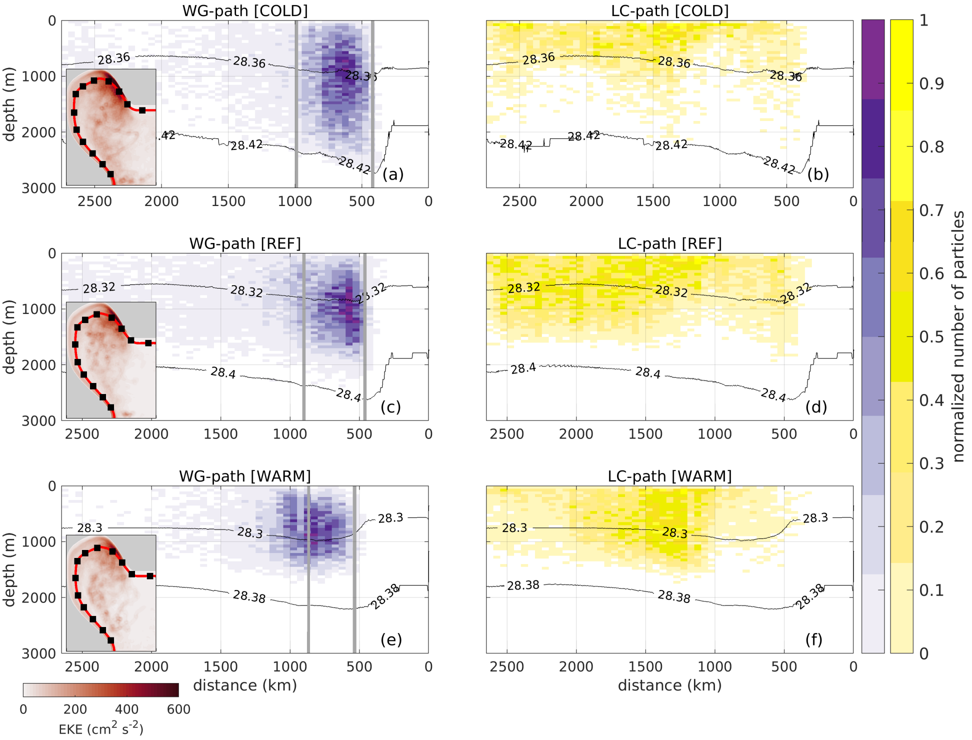

Figure 5.12: Normalized number of particles that cross the 18 Sv barotropic streamfunction and re-enter the boundary current as a function of distance downstream of the inflow and depth, for (left panels) the WG-path (purple shading) and (right panels) the LC-path (yellow shading) for (a-b) COLD, (c-d) REF and (e-f) WARM. Particles are binned over segments of 30 m in depth and 50 km in alongshore direction, starting from the inflow (see inset in (a, c and e), black squares mark distances of 200 km). Note that the horizontal axis is flipped. The black contours outline the 5-year mean density of the boundary current as a function ($\bar{\sigma}_{\Psi_b}$, in kg m^{-3}) of the alongshore coordinate. Grey vertical lines denote the region near the West Greenland coast where EKE>200 cm^2 s^{-2}. Inset in (a, c and e) shows the 5-year mean EKE in each simulation (shading, in cm^2 s^{-2}).

ment occurs between 800-1800 m depth where the annual mean density of the boundary current is $\bar{\sigma}_{\Psi_b}$ >28.30 kg m^{-3} (Figure 5.12c). Under a colder regime, this entrainment extends to deeper (800-2500 m) and denser ($\bar{\sigma}_{\Psi_b}$ >28.32 kg m^{-3}) layers (contours in Figure 5.12a) than in REF. The opposite holds for WARM, in which the entrainment peaks in shallower (500-1500 m) and lighter ($\bar{\sigma}_{\Psi_b}$ <28.32 kg m^{-3}) layers (Figure 5.12e) compared to REF. In contrast, Figure 5.12(b,d,f) shows that in all three simulations the majority of the LC-path particles re-enter the boundary current at a distance more than 1000 km downstream from the inflow (Figure 5.12b,d,f) and at shallower (z<1200 m), and thus lighter layers than the WG-path particles. Note that in all three simulations (REF, COLD and WARM) the particles that follow the LC-path re-enter the boundary current in a similar density layer (Figure 5.12(b,d,f)).

Interestingly, the density of the particles that re-enter the boundary current by crossing the 18 Sv barotropic streamfunction (σ_{crossing}) is highly correlated to the mean density of the boundary current ($\bar{\sigma}_{\Psi_b}$) at the location of the crossing in REF (shading in Figure 5.13). This is in line with the finding in section 4.6 that the entrainment of convected water may be established only when its density and depth match the local properties of the boundary current. Furthermore, in all three simulations, convected water with of varying density is entrained at the Labrador side (LC-path), while only the densest waters formed in the interior re-enter the boundary current by following the WG-path. Last, in line with expectations the convected waters that re-enter the boundary current at the West Greenland coast (WG-path) are denser (lighter) in COLD (WARM) compared to REF (compare contours in Figure 5.13).

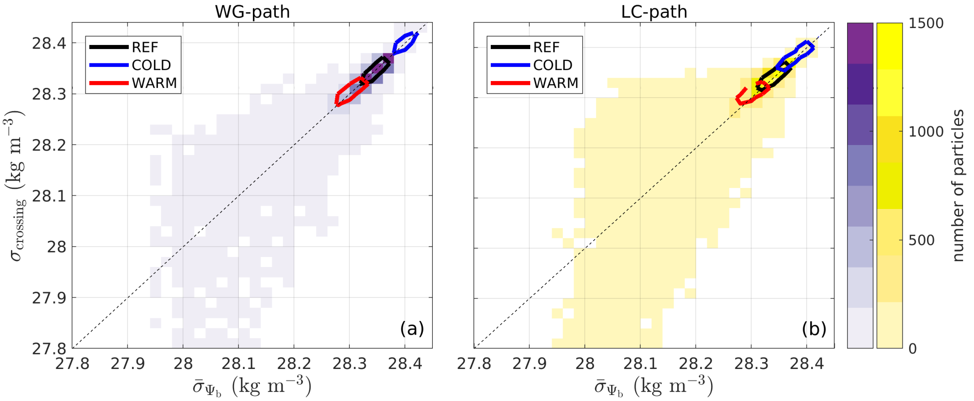

Figure 5.13: Scatter plot of the density of particles when they cross the 18 Sv barotropic streamfunction (σ_{crossing}, in kg m^{-3}) versus the 5-year mean density of the boundary current (i.e., $\bar{\sigma}_{\Psi_b}$) at this location, for particles that follow (a) the WG-path and (b) the LC-path in terms of number of particle. The latter is calculated as the sum of particles in a certain $\Delta\sigma$-$\Delta\sigma$ bin ($\Delta\sigma$ = 0.01 kg m^{-3}). Note that the shading corresponds to the values for REF and the contours encompass 40% of particles in REF (in black), COLD (in blue) and WARM (in red).

5.8. Discussion and conclusions

In this chapter, we have investigated the sensitivity of the upstream pathways of the water masses exiting the Labrador Sea to changes in the surface heat fluxes. In particular, we have explored the response of the pathways found in chapter 3, the water mass transformation, the net overturning and the boundary-interior exchange to changes in the surface winter heat loss. To this end, we performed Lagrangian analyses by using the output of the two sensitivity simulations (COLD and WARM) introduced in section 2.2.2. The results are compared to the REF simulation (chapter 3).

The direct impact of changes in the forcing conditions was evident in the properties of both the convection and the eddy field in the Labrador Sea (Figure 2.9). In a colder (warmer) regime the applied surface heat loss not only increases (decreases) the depth of convection, but also sharpens the horizontal density gradient between the boundary current and the interior. The latter, under the geostrophic assumption, results in faster (slower) rim current (Spall and Pickart, 2001) in the COLD (WARM) simulation (Figure 5.3) and also in the increase (decrease) of the EKE in the basin and in particular near the west coast of Greenland (Figure 2.9c-d). Moreover, the product of convection is denser (lighter) in COLD (WARM) than in REF (Figure 5.4). This is in agreement with observational studies that reported the formation of denser LSW during severe winters with stronger heat loss over the Labrador Sea (e.g., Yashayaev and Loder, 2009, 2017).

The Lagrangian analyses of the sensitivity simulations had shown that, similar to the REF simulation, the water masses follow either the direct route within the boundary current (*withinBC* particles) or the indirect route (*interiorShort* and *interiorLong* particles) from the inflow region south of Greenland to the outflow region on the Labrador side (Figure 5.5b). The particle density plots indicated that the boundary current-interior exchange is present in the sensitivity simulations (COLD and WARM) as in the REF simulation (Figure 5.5). This exchange was found to be weaker in the COLD simulation than in the other two simulations, suggesting that under a colder regime less particles leave the boundary current and make an excursion into the interior of the basin as deduced from the smaller fraction of the *interiorShort* particles in COLD (Figure 5.5a). However, the volume transport carried by the *interiorLong* particles, which represent the densest water masses in this model (Figure 3.6c), is increased by 5% in COLD with respect to REF. Apparently, in a colder regime the product of convection in the Labrador Sea is denser than the one formed during a normal winter (Figure 5.4) and it remains in the basin for longer time.

In the idealized study of Spall (2004) and the observational study of Pickart and Spall (2007) it has been shown that in the Labrador Sea a transport imbalance along a section across the basin yields an overturning in density space in the basin. Moreover, they indicated that water mass transformation occurs both in the interior and in the boundary current itself. A remaining question in these studies was to distinguish the contribution of the water that gets transformed in the boundary current versus the interior. It has been shown in chapter 3 that the water mass transformation mainly occurs in the interior of the basin. The results presented in this chapter highlight that the characteristics of water mass transformation in the sensitivity simulations (COLD and WARM) differ from the REF simulation (Figure 5.6). In particular, the volume transport of the *withinBC* particles that subduct within the boundary current and the *interiorShort* particles that subduct in the interior of the basin is reduced by ~20-40% in COLD and WARM with respect to the REF simulation (Figure 5.7). Further analysis of the pathways of the water masses that are transformed in the interior of the Labrador Sea (i.e., WG- and LC-paths) clearly shows that the increase (decrease) in the local eddy activity in COLD (WARM) results in a stronger (weaker) transport of the denser water masses towards the west coast of Greenland (WG-path, Figure 5.8c) compared to their direct export via the LC-path at the Labrador side. Moreover, it is evident that the water masses that follow the WG-path carry the densest product of convection events that occur in the interior of the basin (Figure 5.9) and that their density range is higher (lower) in COLD (WARM) than in REF. This confirms the results found in chapter 3 and chapter 4 that the water masses that have been transformed into denser water masses in the interior are steered by the eddies towards the boundary current along isopycnals at the high EKE region (Figure 5.12a,c,e and Figure 5.13a).

Interestingly, when the winter surface heat loss is by 50% increased (COLD) or reduced (WARM) the properties of convection in the interior are drastically affected and this in turn affects the net overturning in the basin in density space (Spall and Pickart, 2001; Straneo, 2006a). The overturning in density space is reduced by 15% and 40% with respect to the REF in COLD and WARM, respectively and also its maximum is found in higher and lower density Figure 5.10a). The latter can be explained by the fact that the product of convection is denser (lighter) in COLD (WARM) than in the REF simulation (Figure 5.4) and therefore the maximum overturning occurs in a different density class. This is in agreement with Holte and Straneo (2017) who suggested that the difference in the density where the maximum overturning estimate is found in the 1990s and 2000s reflects the density changes in the Labrador Sea due to changes in the surface heat fluxes. Moreover, Li and Lozier (2018) showed that the formation of LSW is strongly correlated to the magnitude of the surface heat fluxes over the Labrador Sea. However, it is yet unclear why the strength of the overturning in the basin is weaker in both the colder and warmer winter state scenario than in a normal winter state of the Labrador Sea. Note that the contribution of the *interiorLong* particles is not included in the overturning calculations (section 5.6) since they remain in the basin within the six years of the advection period. Thus, to answer this question explicitly, an advection period of the particles longer than the six years used here is required to reduce the number of the *interiorLong* particles and thus to obtain a complete estimate of the local overturning in the Labrador Sea.

Our results indicate that the changes in the surface heat flux applied in the model (COLD and WARM) also affect the relative importance of the different pathways on the overturning in density space. Under the scenario of a stronger (weaker) surface winter heat loss, the transformation of the *withinBC* results into denser (lighter) water masses than in REF, increasing (decreasing) their contribution to the overall overturning (Figure 5.10b,d). However, it is clear that similarly to the REF simulation the volume transport of the densest water masses is primarily carried by particles that have resided in the interior (i.e. *interiorShort* particles), while the particles that follow the fast route (i.e. *withinBC*) mainly transform into lighter water masses in both the sensitivity simulations.

The direct impact of the exchange between the boundary current and the interior on the residence time of the water masses in the Labrador Sea as seen in chapter 3 is also evident in both the sensitivity experiments (not shown). As found in REF, within one year 90% of the volume transport carried by the *withinBC* particles exits the basin, while only 30% of the transport associated with the *interiorShort* particles exits within that time frame in both COLD and WARM. That is, our analysis does not reveal strong evidence that the residence timescales associated with these two pathways are affected by the changes in the surface heat loss (not shown). However, when the basin experienced stronger (weaker) winter heat losses in the COLD (WARM) simulation the volume transport of the *interiorLong* particles increases (decreases). Note that these particles represent the densest water masses found in this model that take more than six years to exit the Labrador Sea. Thus, our results suggest that the replenishment of a lighter product of convection is faster than of a denser product during severe winters. This would yield a delayed arrival of the LSW at the sites where observational studies dedicated to studying the AMOC and its variability such as the OSNAP array (Holliday et al., 2018; Lozier et al., 2019) are focused on.

Although the sensitivity simulations presented in this chapter are idealized, our study can be considered as an oceanic paradigm in which the surface heat fluxes over the Labrador Sea adapt to a changing climate scenario. Overall, in this study we showed how the surface heat fluxes in the Labrador Sea impact the properties of convection and the eddy field in the basin. In turn, these changes affect the strength of the pathways that the water masses follow prior to exiting the basin and thus their transformation rates, which in turn alters the local overturning. Our sensitivity simulations underline the importance of the interior-boundary current exchange that regulates the LSW export and hence impacts to the AMOC variability. Therefore, this study suggests that a full understanding of the link between the LSW production and the AMOC variability requires longer oceanic observational data than the short period of OSNAP array (Holliday et al., 2018; Lozier et al., 2019). In this view, modelling efforts should be able to resolve the mesoscale features required to capture the interior-boundary current exchange.

Chapter 6

Conclusions and recommendations

This thesis has provided helpful insights on the physical processes involved in the formation, export and variability of the deep water in the Labrador Sea and thus in the dynamics of AMOC. Previous chapters highlighted the importance of the interactions between the boundary current and the interior of the Labrador Sea for these processes. Moreover, these processes were found to be sensitive to the atmospheric forcing. The methodology followed in this thesis involves analyzing data from an idealized regional model, a global ocean model, available observations and a Lagrangian tracking tool. The analysis based on the idealized regional model facilitated the investigation of certain physical processes and the acquisition of a qualitative view on the interior-boundary current exchange. The Lagrangian analyses applied in this thesis provided more quantitative understanding of this exchange, while the data from observations confirmed its existence. Consequently, the diversity of methods used throughout this thesis facilitates an efficient approach to delve deeper into the dynamics of the Labrador Sea. This final chapter provides a summary of the conclusions obtained through this thesis (section 6.1). Additionally recommendations for future research following from these results are also discussed (section 6.2).

6.1. Conclusions

The recent studies using data from the OSNAP array (Lozier et al., 2019; Zou et al., 2020) and mentioned in the previous chapters (chapter 3 and chapter 4), suggest that the deep water formation that occurs in the Labrador Sea and variability therein contributes minimally to the AMOC variability. The work presented in this thesis has shown that the overturning in the Labrador Sea is the result of a complex interplay between the convective interior, the boundary current and the eddy field. This interplay involves various export routes of the deep water formed in the interior, which are characterized by different timescales. The lack of information on these mechanisms in the observational efforts that only document the net result of the events that take place in the region (since they only capture changes that occur between the southern Labrador and the southwestern tip of Greenland) may obscure the actual role of the processes occurring in the Labrador Sea for the AMOC dynamics. This follows from the overall conclusions obtained from the combined work of this thesis which highlight the crucial role of the exchanges between the boundary current and the interior of the Labrador Sea:

1 - The properties of convection also affect the eddy field, which in turn regulates the downwelling strength. Chapter 2 has shown that the connection between the process of convection and the magnitude of downwelling within the Labrador Sea is not straightforward. It has been shown that the horizontal density gradients set by the convection in the interior of the basin affect the stability of the boundary current (section 2.4.1). In turn, this has a direct influence on the eddy field in the basin (Figure 2.9). Thus, it is expected that the offshore vorticity fluxes associated with the eddy field will change (Spall, 2010; Brüggemann et al., 2017). Eventually, it is this chain of events (Figure 2.13) that regulates the magnitude of the downwelling (Spall, 2004). These conclusions are based on the analysis of the output of an idealized model that is able to represent the key dynamics of the Labrador Sea and resolves the mesoscale activity of the basin (Figure 2.1, Figure 3.1). Undoubtedly, chapter 2 emphasizes that a good representation of the eddy field in numerical models is one of the key elements required for the correct representation of the interplay between the process of deep convection and the downwelling in marginal seas at high latitudes.

2 - The densest water masses formed in the interior follow an indirect, relatively slow route prior to exiting the Labrador Sea that involves boundary-interior exchange. Based on the Lagrangian analyses introduced in chapter 3 and chapter 4 it has been revealed that prior to exiting the Labrador Sea via the boundary current, the water masses follow a fast (i.e., export timescales less than 2 years), direct route or a slower (i.e., export timescales more than 3 years), indirect route (Figure 3.13, Figure 4.10). In line with other studies who found that the transformation along the boundary current plays a key role for the ventilation of the water masses in the Labrador Sea (Brandt et al., 2007; MacGilchrist et al., 2020), the results in section 3.5 and section 4.4.1 indicated that the contribution of boundary current subduction rate is as important as that of subduction rate in the interior of the Labrador Sea. However, it has been shown that the characteristics of water mass transformation differ for the direct and indirect pathways (section 3.4.2, section 4.4.1); the water masses transformed in the interior are typically denser than those transformed within the boundary current (Figure 4.6c-d).

Additionally, the analysis of the trajectories of Argo floats and numerical particles in both the idealized and realistic model presented in chapter 3 and chapter 4 reveals that the indirect route is regulated by the boundary current-interior exchanges, which occur more predominantly along the West Greenland coast. The lateral, along-isopycnal transport of convected water towards the boundary current in this region can only take place where its density and depth match the local properties of the boundary current. This adds a potentially strong constraint on this process (Figure 4.11 and Figure 4.12). Moreover, it has been shown that particularly the denser water masses formed in the interior of the basin first follow an eddy-driven path towards the West Greenland coast and re-enter the boundary current there before exiting the Labrador Sea at 53 ^{o}N (section 4.4.2). This circulation pattern implies longer travel distances and thus longer export timescales for the dense water masses in contrast to the rapid export of lighter water masses via the direct route. Hence, it is important that these boundary current-interior exchanges are considered when investigating possible connections between the processes occurring in the Labrador Sea and AMOC variability.

3 - The boundary-current interior exchange regulates the overturning in the Labrador Sea in denser layers. Based on the Lagrangian analysis performed by using the output of both the idealized (chapter 3) and realistic (chapter 4) model, the local overturning can be computed (Figure 3.7, Figure 4.7). These estimates compare well with the magnitude of the overturning that is found in both observational and numerical modelling studies (Table 4.3, Spall and Pickart, 2001; Lozier et al., 2019; Zou et al., 2020; MacGilchrist et al., 2020). The estimates of the overturning in density space in a Lagrangian view can shed light on the relative importance of the different pathways. It has been shown that 60% of the maximum overturning in density space can be attributed to the water mass transformation along the indirect route and 40% along the direct route (Figure 3.7d). Moreover, the results presented in chapter 3 and chapter 4 revealed that the signal of the overturning in lighter layers is mainly related to water masses that are formed along the boundary current, but more importantly, that the signal in denser layers is primarily controlled by the water masses that are formed in the interior of the basin and follow the indirect route to exit the basin (section 3.4.3, section 4.4.1). Hence, it is clear that the indirect route, which is regulated by boundary current-interior exchanges, is crucial for the representation of the overturning in denser layers.

Essentially, the importance of the indirect route for the overturning estimates together with the multi-year timescales that characterize this route, imply that a year-to-year correspondence between the properties of the denser water masses formed in the interior of the Labrador Sea (in line with Cuny et al., 2005) and in measurements of variations in the overturning strength at the southwestern part of the basin as collected by the OSNAP array (Lozier et al., 2017) is not to be expected.

4 - The response of the Labrador Sea dynamics to changes in surface forcing is characterized as a non-linear process. The sensitivity analyses discussed in chapter 2 and chapter 5 have shown that both the properties of the convection and the eddy field are influenced when the surface forcing changes. Chapter 2 has demonstrated that under a colder (warmer) regime the wintertime mixed layer becomes deeper (shallower, Figure 2.9a-b), but these changes are not proportional to the variation in the applied surface heat flux. The associated increase/decrease in the temperature gradient between the interior of the Labrador Sea and the adjacent boundary current leads to an enhanced (reduced) mesoscale activity in the basin (Figure 2.9c-d). However, the fact that the changes in the eddy heat advection into the interior are not simply proportional to the changes in the applied heat loss (Figure 2.10) emphasizes that the properties of the convection are regulated by the combined effect of the surface heat flux and lateral eddy flux.

Additionally, the Lagrangian analysis performed in chapter 5 has shown that both the transport carried by each pathway that the water masses follow prior to exiting the basin and their transformation rates are altered by the changes in the surface forcing (Figure 5.5, Figure 5.7). As a consequence, the overturning in the Labrador Sea and the relative importance of the different pathways are both affected (section 5.6); when a stronger (weaker) surface winter heat loss is introduced, the water mass transformation that takes place both in the interior of the basin and along the boundary current results in denser (lighter) water masses (Figure 5.9). As a direct impact, the maximum signal of the overturning occurs at a denser (lighter) layer than the one found in a normal winter state of the Labrador Sea (Figure 5.10a). Interestingly, in both colder and warmer winter state scenarios the strength of the overturning in the basin is weaker than in a normal winter state of the Labrador Sea (Figure 5.10a). Although, there is no clear explanation on why this happens, it highlights the complexity of the dynamics that are involved in determining the strength of the overturning in the Labrador Sea.

The along-isopycnal, lateral transport of the newly-formed waters from the interior towards the boundary current that occurs when the depth and density of these waters match the local properties of the boundary current (Figure 4.11 and Figure 4.12) is also affected by the changes in the surface forcing. It has been shown that under a colder regime, denser water masses are formed in the interior of the basin and that their entrainment in the boundary current, which is controlled by the combination of their density and the boundary current stratification, occurs in denser layers (Figure 5.12, Figure 5.13). Moreover, the transport carried by the particles that represent the densest water masses found in this model (i.e. *interiorLong* particles), which take more than six years to exit the Labrador Sea, is increased compared to the reference simulation (Figure 5.5), and the opposite holds under a warmer regime. These two findings suggest that the additional constraint for the entrainment of convected water in the boundary current results in a delayed arrival of the densest water masses at the sites where the AMOC variability is observed (such as the OSNAP array Holliday et al., 2018; Lozier et al., 2019) compared to the lighter water masses. In summary, this thesis highlighted that in a changing climate, the non-linear response of the Labrador Sea dynamics to changes in surface forcing is an additional factor of complexity in understanding the AMOC variability.

6.2. Recommendations

The current debate on the importance of the west and east North Atlantic Ocean for the AMOC introduced by the recent observations along the OSNAP array (Lozier et al., 2019; Zou et al., 2020) has uncovered that the underlying physical processes that determine the AMOC strength and variability are still not fully understood. It is clear from this thesis that the boundary current-interior exchange is a key process that deserves more attention when monitoring the AMOC variability. Moreover, the methodology and the results presented in this thesis suggest that the Lagrangian methods applied in an idealized and a realistic model are powerful tools to improve our understanding on the interplay between the interior and the boundary current system of a convective marginal sea. The following recommendations for future research are based on the thesis findings.

Additional sensitivity simulations using idealized models have the potential to drive in better directions towards the improvement of climate models. For instance, by modifying the idealized model introduced in chapter 2, future scenarios of increased input of freshwater fluxes in the Labrador Sea can be investigated. In this way, more insight can be gained on the role of the freshwater fluxes on the deep convection, downwelling and the boundary-interior exchange in the Labrador Sea and thus on the AMOC variability. The implementation of a higher resolution in climate models would be a step towards resolving important processes such as the boundary-interior exchange. Although such an implementation is currently not feasible due to the high computational cost that is required, the insights from idealized studies can be taken into account in order to yield more adequate parameterizations associated with the processes mentioned above (i.e. mixing and diffusion schemes).

At high latitudes, the buoyancy and wind forcing display a strong seasonality. Recent studies have shown that the overturning in the Labrador Sea also has a large seasonality (Holte and Straneo, 2017; Sayol et al., 2019). This suggests that observational studies aiming at estimating the mean local overturning require prolonged data time series to be able to accurately draw conclusions. However, it remains unclear whether the seasonality of the overturning results from the seasonality of the surface forcing or a seasonality that the boundary current-interior exchange might display. Thus, further investigation on the seasonal cycle of the latter exchange could help in explaining the seasonality in the overturning. A Lagrangian analysis using the output of a high-resolution ocean model with interannual varying atmospheric forcing could be a suitable strategy to assess this question.

The eddy-driven, along-isopycnal export of dense waters from the interior of the Labrador Sea that was discussed in this thesis (chapter 2-chapter 5) is also a possible mechanism for the export of the dense waters formed in other convective marginal seas such as the Irminger Sea (Le Bras et al., 2020) and the Nordic Seas (Ypma et al., 2020b). For instance, several studies have shown that deep convection also occurs in the Irminger Sea under favorable conditions (Pickart et al., 2003; de Jong, 2010; de Jong et al., 2012, 2018; Våge et al., 2011a). Limited literature on the eddy activity in the Irminger Sea suggests that the eddies found in that region originate from both sides of the basin and that although they have smaller size than in the Labrador Sea they are more abundant (Fan et al., 2013). Therefore, modelling studies similar to the one followed in chapter 4 would be suitable to investigate the role of the boundary current-interior exchange for the dynamics of other convective marginal seas.

As a final remark, it is worth mentioning that maintaining the current observational efforts in the North Atlantic is of crucial importance. Up-to-date data from the existing arrays (i.e., RAPID and OSNAP) have revealed new aspects of the processes involved in the AMOC and have challenged the numerical modelling community to evaluate and advance their methods by focusing on understanding the new insights gained by these observations. Undoubtedly, history has proven that even with a simple bucket, measurements of the water column can change and improve our understanding of the global ocean circulation (Lozier, 2015).

Acknowledgements

> Τόδε έργον αέξεται,
> ᾧ επιμίμνω.
> Οδύσσεια ξ′ 66,
> Όμηρος

I would like to express my sincere gratitude to all of those who helped to complete this dissertation.

First and foremost I would like to thank my supervisor, Caroline. I have thoroughly enjoyed working with you, and the knowledge I gained from you goes far beyond what is required to be an oceanographer. I am very thankful for the many opportunities you gave me, including participation in numerous conferences and the research cruise in the North Atlantic Ocean. Thank you for always being available, for all your patience and for being a great mentor!

I would like to thank my promotor, Julie, for your constant support, encouragement and guidance. Thank you for spending hours with me having scientific discussions at your office or in your house. Your questions and suggestions have played a major role in shaping this thesis and taught me to be more confident on my results. Thank you!

I have also received much help, advice and support from Caroline's group: Nils, Steffie, Carine and Juanma. It has been a pleasure to be part of this group, both in and out the office! I would not have done all of this work on my own. I am very grateful to have worked with such fine scientists and persons. Thank you!

I would like to thank the members of my defence committee. I appreciate your comments, interest, and availability. I am honored to be part of this journey.

Moreover, I have to mention how grateful I feel to my colleagues in the department for many interesting scientific discussions, laughs, support and of course for all the coffee breaks.

I warm-heartedly thank my new and old friends all over the world supporting me outside the PhD-sphere, getting my mind off the thesis.

Finally, the biggest thanks goes to my family since nothing would have been accomplished without their encouragement and support. To my best friend and "sister" Μαρία I owe a big thank-you for always believing in me and being part of my life even from far away. Jesús, thank you for entering and being in my life. You were always by my side regardless of the situation with my thesis and you helped me survive these stressful years of my life. I would like to thank my parents, Ανδρέα και Ειρήνη, my sister, Λουκία, and my brother, Χρήστο, for their continuous love and tireless support through all of these years and encouragement to not give up during the hard times. Last, but not least, I want to thank my two little tulips, Μαρία και Ειρήνη, for making me smile everyday. I am sorry that I am far away, but you know that I will always be there for you. Σας αγαπώ όλους πολύ.

List of Publications

Peer reviewed journal publications as first author

Georgiou, S., Ypma, S.L., Brüggemann, N., Sayol, J-M., van der Boog, C.G., Spence P., Pietrzak, J.D. and C.A., Katsman, Direct and indirect pathways of convected water masses and their impacts on the overturning dynamics of the Labrador Sea, *Journal of Geophysical Research: Oceans*, https://doi-org.tudelft.idm.oclc.org/10.1029/2020JC016654

Georgiou, S., Ypma, S.L., Brüggemann, N., Sayol, J-M., Pietrzak, J.D. and C.A., Katsman, 2020. Pathways of the water masses exiting the Labrador Sea: the importance of boundary - interior exchanges, *Ocean Modelling*, 150, https://doi.org/10.1016/j.ocemod.2020.101623

Georgiou, S., van der Boog, C.G, Brüggemann, N., Ypma, S.L., Pietrzak, J.D. and C.A., Katsman, 2019. On the interplay between downwelling, deep convection and mesoscale eddies in the Labrador Sea, *Ocean Modelling*, 135, 56-70, https://doi.org/10.1016/j.ocemod.2019.02.004

Georgiou S., Mantziafou A., Sofianos S., Gertman I., Özsoy E., Somot S. and Vervatis V., 2014. Climate Variability and Deep Water Mass Characteristics in the Aegean Sea, *Atmospheric Research*, https://doi.org/10.1016/j.atmosres.2014.07.023

Peer reviewed journal publications as co-author

Ypma, S.L., Georgiou, S., Dugstad, J. S., Pietrzak, J.D. and C.A., Katsman, 2020. Pathways and water mass transformation along and across the Mohn-Knipovich Ridge in the Nordic Seas, *Journal of Geophysical Research: Oceans*, 125, https://doi.org/10.1029/2020JC016075

Ypma, S. L., M. A. Spall, E. Lambert, S. Georgiou, J. D. Pietrzak, and C. A. Katsman, 2020. The Contrasting Dynamics of the Buoyancy-Forced Lofoten and Greenland Basins, *Journal of Physical Oceanography*, 50, 1227-1244, https://doi.org/10.1175/JPO-D-19-0280.1

Ypma, S.L., N. Brüggemann, S. Georgiou, P. Spence, H.A. Dijkstra, J.D. Pietrzak, C.A. Katsman, 2019. Pathways and watermass transformation of Atlantic Water entering the Nordic Seas through Denmark Strait in two high resolution ocean models, *Deep-Sea Research Part I*, 145, 59–72, https://doi.org/10.1016/j.dsr.2019.02.002

Sofianos, S., V. Vervatis, A. Mantziafou, M. Ravdas and S. Georgiou, 2015: Investigating deep-water formation variability in the Aegean Sea and its influence in the adjacent basins deep circulation, *Journal of the Black Sea/Mediterranean Environment*, Special Issue, (21), 74-77

Özsoy, E., Sofianos, S., Gertman, I., Mantziafou, A., Aydoğdu, A., Georgiou, S., Tutsak, E., Lascaratos, A., Hecht, A. and Latif, M. A., 2014. Deep-Water Variability and Interbasin Interactions in the Eastern Mediterranean Sea. *In The Mediterranean Sea: Temporal Variability and Spatial Patterns* (eds G. L. E. Borzelli, M. Gačić, P. Lionello and P. Malanotte-Rizzoli), John Wiley & Sons, Inc., Oxford. https://doi.org/10.1002/9781118847572.ch7

Curriculum Vitae

September 27, 1986	Born in Athens, Greece
2004	High-School Diploma Papagos high-school Athens, Greece
2004–2010	Bachelor of Science University of Athens, Greece Physics *Thesis:* Study of the upwelling of cold water in the southern coastal area of Cyprus, using satellite data
2010–2013	Master of Science University of Athens, Greece Environmental Physics and Meteorology *Thesis:* Climate variability of the deep water characteristics in the Eastern Mediterranean Sea
January–April 2014	Research Assistant University of Athens, Greece
2015–Present	PhD candidate Delft University of Technology, The Netherlands Environmental Fluidmechanics
June 2019–January 2020	Post Doctoral Researcher Delft University of Technology, The Netherlands Environmental Fluidmechanics
2020-Present	Post Doctoral Researcher Delft University of Technology, The Netherlands Geoscience and Remote Sensing

Bibliography

Amante, C., and B. Eakins (2009), ETOPO1 1 Arc-Minute Global Relief Model: Procedures, Data Sources and Analysis, *NOAA Technical Memorandum NESDIS NGDC-24. National Geophysical Data Center, NOAA*, doi: 10.7289/V5C8276M.

Argo (2020), Argo float data and metadata from Global Data Assembly Centre (Argo GDAC), *SEANOE*, doi: 10.17882/42182.

Belkin, I. M., S. Levitus, J. Antonov, and S.-A. Malmberg (1998), "Great Salinity Anomalies" in the North Atlantic, *Progress in Oceanography*, *41*(1), 1 – 68, doi: 10.1016/S0079-6611(98)00015-9.

Biastoch, A., C. W. Böning, J. Getzlaff, J.-M. Molines, and G. Madec (2008), Causes of Interannual–Decadal Variability in the Meridional Overturning Circulation of the Midlatitude North Atlantic Ocean, *Journal of Climate*, *21*(24), 6599–6615, doi: 10.1175/2008JCLI2404.1.

Böning, C. W., E. Behrens, A. Biastoch, K. Getzlaff, and J. L. Bamber (2016), Emerging impact of Greenland meltwater on deepwater formation in the North Atlantic Ocean, *Nature Geoscience*, *9*(7), 523–527, doi: 10.1038/ngeo2740.

Bower, A., M. S. Lozier, S. F. Gary, and C. W. Böning (2009), Interior pathways of the North Atlantic meridional overturning circulation, *Nature, 459*, 243–247, doi: 10.1038/nature07979.

Bower, A., S. Lozier, and S. Gary (2011), Export of Labrador Sea Water from the subpolar North Atlantic: A Lagrangian perspective, *Deep Sea Research Part II: Topical Studies in Oceanography*, *58*(17), 1798–1818, doi: https://doi.org/10.1016/j.dsr2.2010.10.060.

Bower, A., S. Lozier, A. Biastoch, K. Drouin, N. Foukal, H. Furey, M. Lankhorst, S. Rühs, and S. Zou (2019), Lagrangian Views of the Pathways of the Atlantic Meridional Overturning Circulation, *Journal of Geophysical Research: Oceans*, *124*(0), doi: 10.1029/2019JC015014.

Bracco, A., J. Pedlosky, and R. S. Pickart (2008), Eddy Formation near the West Coast of Greenland, *Journal of Physical Oceanography*, *38*(9), 1992–2002, doi: 10.1175/2008JPO3669.1.

Brandt, P., F. A. Schott, A. Funk, and C. S. Martins (2004), Seasonal to interannual variability of the eddy field in the Labrador Sea from satellite altimetry, *Journal of Geophysical Research*, *109*(C2), C02,028, doi: 10.1029/2002JC001551.

Brandt, P., A. Funk, L. Czeschel, C. Eden, and C. W. Böning (2007), Ventilation and Transformation of Labrador Sea Water and Its Rapid Export in the Deep Labrador Current, *Journal of Physical Oceanography*, *37*(4), 946–961, doi: 10.1175/JPO3044.1.

Brüggemann, N., and C. A. Katsman (2019), Dynamics of downwelling in an eddying marginal sea: contrasting the Eulerian and the isopycnal prespective, *Journal of Physical Oceanography*, doi: 10.1175/JPO-D-19-0090.1.

Brüggemann, N., C. A. Katsman, and H. A. Dijkstra (2017), On the vorticity dynamics of the downwelling branch of the AMOC, in *CLIVAR Exchanges Special Issue: CLIVAR Open Science Conference Award Winners*, vol. 71, pp. 10–12.

Buckley, M. W., and J. Marshall (2016), Observations, inferences, and mechanisms of the Atlantic Meridional Overturning Circulation: A review, *Reviews of Geophysics*, *54*(1), 5–63, doi: 10.1002/2015RG000493.

Cenedese, C. (2012), Downwelling in Basins Subject to Buoyancy Loss, *Journal of Physical Oceanography*, *42*(11), 1817–1833, doi: 10.1175/JPO-D-11-0114.1.

Chafik, L., and T. Rossby (2019), Volume, heat, and freshwater divergences in the subpolar north atlantic suggest the nordic seas as key to the state of the meridional overturning circulation, *Geophysical Research Letters, 46*(9), 4799–4808, doi: 10.1029/2019GL082110.

Chanut, J., B. Barnier, W. Large, L. Debreu, T. Penduff, J. M. Molines, and P. Mathiot (2008), Mesoscale Eddies in the Labrador Sea and Their Contribution to Convection and Restratification, *Journal of Physical Oceanography*, *38*(8), 1617–1643, doi: 10.1175/2008JPO3485.1.

Clarke, R. A., and J.-C. Gascard (1983), The Formation of the Labrador Sea Water. Part I: Large-Scale Processes, *Journal of Physical Oceanography*, *13*, 1764–1778, doi: 10.1175/1520-0485(1983)013<1764:TFOLSW>2.0.CO;2.

Collins, M., R. Knutti, J. Arblaster, J.-L. Dufresne, T. Fichefet, P. Friedlingstein, X. Gao, W. J. Gutowski, T. Johns, G. Krinner, M. Shongwe, C. Tebaldi, A. J. Weaver, and M. Wehner (2013), Long-term Climate Change: Projections, Commitments and Irreversibility Pages 1029 to 1076, in *Climate Change 2013 - The Physical Science Basis*, edited by Intergovernmental Panel on Climate Change, pp. 1029–1136, Cambridge University Press, doi: 10.1017/CBO9781107415324.024.

Courtois, P., X. Hu, C. Pennelly, P. Spence, and P. G. Myers (2017), Mixed layer depth calculation in deep convection regions in ocean numerical models, *Ocean Modelling*, *120*, 60 – 78, doi: 10.1016/j.ocemod.2017.10.007.

Cunningham, S. A., T. Kanzow, D. Rayner, M. O. Baringer, W. E. Johns, J. Marotzke, H. R. Longworth, E. M. Grant, J. J.-M. Hirschi, L. M. Beal, C. S. Meinen, and H. L. Bryden (2007), Temporal Variability of the Atlantic Meridional Overturning Circulation at 26.5 ° N, *Science*, *317*(5840), 935–938, doi: 10.1126/science.1141304.

Cuny, J., P. B. Rhines, P. P. Niiler, and S. Bacon (2002), Labrador Sea Boundary Currents and the Fate of the Irminger Sea Water, *Journal of Physical Oceanography*, *32*(2), 627–647,

Cuny, J., P. B. Rhines, F. Schott, and J. Lazier (2005), Convection above the Labrador Continental Slope, *Journal of Physical Oceanography*, *35*(4), 489–511, doi: 10.1175/JPO2700.1.

Curry, B., C. M. Lee, B. Petrie, R. E. Moritz, and R. Kwok (2014), Multiyear Volume, Liquid Freshwater, and Sea Ice Transports through Davis Strait, *Journal of Physical Oceanography*, *44*, 1244–1266, doi: 10.1175/JPO-D-13-0177.1.

Curry, R. G., M. S. McCartney, and T. M. Joyce (1998), Oceanic transport of subpolar climate signals to mid-depth subtropical waters, *Nature*, *391*(5), 575–577, doi: 10.1038/35356.

de Jong, M. F. (2010), Hydrographic variability in the Irminger Sea, Ph.D. thesis, Utrecht, Universiteit.

de Jong, M. F., and L. de Steur (2016b), Strong winter cooling over the Irminger Sea in winter 2014–2015, exceptional deep convection, and the emergence of anomalously low SST, *Geophysical Research Letters*, *43*(13), 7106–7113, doi: 10.1002/2016GL069596.

de Jong, M. F., H. M. Van Aken, K. Våge, and R. S. Pickart (2012), Convective mixing in the central Irminger Sea: 2002-2010, *Deep-Sea Research Part I: Oceanographic Research Papers*, *63*, 36–51, doi: 10.1016/j.dsr.2012.01.003.

de Jong, M. F., A. S. Bower, and H. H. Furey (2014), Two Years of Observations of Warm-Core Anticyclones in the Labrador Sea and Their Seasonal Cycle in Heat and Salt Stratification, *Journal of Physical Oceanography*, *44*(2), 427–444, doi: 10.1175/JPO-D-13-070.1.

de Jong, M. F., A. S. Bower, and H. H. Furey (2016), Seasonal and Interannual Variations of Irminger Ring Formation and Boundary-Interior Heat Exchange in FLAME, *Journal of Physical Oceanography*, *46*(6), 1717–1734, doi: 10.1175/jpo-d-15-0124.1.

de Jong, M. F., M. Oltmanns, J. Karstensen, and L. de Steur (2018), Deep Convection in the Irminger Sea Observed with a Dense Mooring Array, *Oceanography*, *31*(1), 50–59, doi: 10.5670/oceanog.2018.109.

Desbruyères, D. G., H. Mercier, G. Maze, and N. Daniault (2019), Surface predictor of overturning circulation and heat content change in the subpolar North Atlantic, *Ocean Science*, *15*(3), 809–817, doi: 10.5194/os-15-809-2019.

Dickson, R., J. Lazier, J. Meincke, P. Rhines, and J. Swift (1996), Long-term coordinated changes in the convective activity of the North Atlantic, *Progress in Oceanography*, *38*(3), 241–295, doi: 10.1016/S0079-6611(97)00002-5.

Dickson, R., B. Rudels, S. Dye, M. Karcher, J. Meincke, and I. Yashayaev (2007), Current estimates of freshwater flux through Arctic and subarctic seas, *Progress in Oceanography*, *73*(3), 210 – 230, doi: 10.1016/j.pocean.2006.12.003.

Dickson, R. R., J. Meincke, S.-A. Malmberg, and A. J. Lee (1988), The “great salinity anomaly” in the Northern North Atlantic 1968–1982, *Progress in Oceanography*, *20*(2), 103 – 151, doi: 10.1016/0079-6611(88)90049-3.

Döös, K. (1995), Interocean exchange of water masses, *Journal of Geophysical Research: Oceans*, *100*(C7), 13,499–13,514, doi: 10.1029/95JC00337.

Drijfhout, S., v. O. G. J., and C. A. (2012), Is a decline of amoc causing the warming hole above the north atlantic in observed and modeled warming patterns?, *J. Climate*, *25*, 8373–8379, doi: 10.1175/JCLI-D-12-00490.1.

Eden, C., and C. Böning (2002), Sources of Eddy Kinetic Energy in the Labrador Sea, *Journal of Physical Oceanography*, *32*(12), 3346–3363, doi: 10.1175/1520-0485(2002)032<3346:SOEKEI>2.0.CO;2.

Eden, C., and J. Willebrand (2001), Mechanism of interannual to decadal variability of the North Atlantic circulation, *Journal of Climate*, *14*(10), 2266–2280, doi: 10.1175/1520-0442(2001)014<2266:MOITDV>2.0.CO;2.

Eldevik, T., J. E. Ø. Nilsen, D. Iovino, K. A. Olsson, A. B. Sandø, and H. Drange (2009), Observed sources and variability of Nordic seas overflow, *Nature Geoscience*, *2*(6), 406–410, doi: 10.1038/ngeo518.

Fan, X., U. Send, P. Testor, J. Karstensen, and P. Lherminier (2013), Observations of Irminger Sea Anticyclonic Eddies, *Journal of Physical Oceanography*, *43*(4), 805–823, doi: 10.1175/JPO-D-11-0155.1.

Feucher, C., Y. Garcia-Quintana, I. Yashayaev, X. Hu, and P. G. Myers (2019), Labrador Sea Water formation rate and its impact on the local Meridional Overturning Circulation, *Journal of Geophysical Research: Oceans*, doi: 10.1029/2019JC015065.

Fischer, J., F. A. Schott, and M. Dengler (2004), Boundary Circulation at the Exit of the Labrador Sea, *Journal of Physical Oceanography*, *34*(7), 1548–1570, doi: 10.1175/1520-0485(2004)034<1548:BCATEO>2.0.CO;2.

Fischer, J., M. Visbeck, R. Zantopp, and N. Nunes (2010), Interannual to decadal variability of outflow from the Labrador Sea, *Geophysical Research Letters*, *37*(24), doi: 10.1029/2010GL045321.

Fontela, M., M. I. García-Ibáñez, D. A. Hansell, H. Mercier, and F. F. Pérez (2016), Dissolved Organic Carbon in the North Atlantic Meridional Overturning Circulation, *Scientific Reports*, *6*(1), 26,931, doi: 10.1038/srep26931.

Fratantoni, P. S., and R. S. Pickart (2007), The western north atlantic shelfbreak current system in summer, *Journal of Physical Oceanography*, *37*(10), 2509–2533, doi: 10.1175/JPO3123.1.

Funk, A., P. Brandt, and T. Fischer (2009), Eddy diffusivities estimated from observations in the labrador sea, *Journal of Geophysical Research: Oceans*, *114*(4), 1–11, doi: 10.1029/2008JC005098.

Garcia-Quintana, Y., P. Courtois, X. Hu, C. Pennelly, D. Kieke, and P. G. Myers (2019), Sensitivity of Labrador Sea Water Formation to Changes in Model Resolution, Atmospheric Forcing, and Freshwater Input, *Journal of Geophysical Research: Oceans*, *124*(3), 2126–2152, doi: 10.1029/2018JC014459.

Gary, S. F., M. S. Lozier, A. Biastoch, and C. W. Böning (2012), Reconciling tracer and float observations of the export pathways of Labrador Sea Water, *Geophysical Research Letters*, *39*(24), doi: 10.1029/2012GL053978.

Gascard, J.-C., and R. A. Clarke (1983), The Formation of Labrador Sea Water. Part 2: Mesoscale and Smaller-Scale Processes, *Journal of Physical Oceanography*, *13*, 1779–1797, doi: 10.1175/1520-0485(1983)013<1779:tfolsw>2.0.co;2.

Gelderloos, R., C. A. Katsman, and S. S. Drijfhout (2011), Assessing the Roles of Three Eddy Types in Restratifying the Labrador Sea after Deep Convection, *Journal of Physical Oceanography*, *41*(11), 2102–2119, doi: 10.1175/JPO-D-11-054.1.

Gelderloos, R., F. Straneo, and C. A. Katsman (2012), Mechanisms behind the Temporary Shutdown of Deep Convection in the Labrador Sea: Lessons from the Great Salinity Anomaly Years 1968–71, *Journal of Climate*, *25*(19), 6743–6755, doi: 10.1175/JCLI-D-11-00549.1.

Gelderloos, R., C. A. Katsman, and K. Våge (2013), Detecting Labrador Sea Water formation from space, *Journal of Geophysical Research: Oceans*, *118*(4), 2074–2086, doi: 10.1002/jgrc.20176.

Georgiou, S., C. G. van der Boog, N. Brüggemann, S. L. Ypma, J. D. Pietrzak, and C. A. Katsman (2019), On the interplay between downwelling, deep convection and mesoscale eddies in the Labrador Sea, *Ocean Modelling*, *135*, 56–70, doi: 10.1016/j.ocemod.2019.02.004.

Georgiou, S., S. L. Ypma, N. Brüggemann, J.-M. Sayol, J. D. Pietrzak, and C. A. Katsman (2020), Pathways of the water masses exiting the Labrador Sea: The importance of boundary–interior exchanges, *Ocean Modelling*, *150*, 101,623, doi: 10.1016/j.ocemod.2020.101623.

Griffies, S. M., A. Biastoch, C. Böning, F. Bryan, G. Danabasoglu, E. P. Chassignet, M. H. England, R. Gerdes, H. Haak, R. W. Hallberg, W. Hazeleger, J. Jungclaus, W. G. Large, G. Madec, A. Pirani, B. L. Samuels, M. Scheinert, A. S. Gupta, C. A. Severijns, H. L. Simmons, A. M. Treguier, M. Winton, S. Yeager, and J. Yin (2009), Coordinated Ocean-ice Reference Experiments (COREs), *Ocean Modelling*, *26*(1), 1 – 46, doi:

10.1016/j.ocemod.2008.08.007.

Hallberg, R. (2013), Using a resolution function to regulate parameterizations of oceanic mesoscale eddy effects, *Ocean Modelling*, *72*, 92 – 103, doi: 10.1016/j.ocemod.2013.08.007.

Handmann, P., J. Fischer, M. Visbeck, J. Karstensen, A. Biastoch, C. Böning, and L. Patara (2018), The deep western boundary current in the labrador sea from observations and a high-resolution model, *Journal of Geophysical Research: Oceans*, *123*(4), 2829–2850, doi: 10.1002/2017JC013702.

Hansen, B., K. M. Húsgarð Larsen, H. Hátún, and S. Østerhus (2016), A stable Faroe Bank Channel overflow 1995–2015, *Ocean Science*, *12*(6), 1205–1220, doi: 10.5194/os-12-1205-2016.

Hátún, H., C. C. Eriksen, and P. B. Rhines (2007), Buoyant Eddies Entering the Labrador Sea Observed with Gliders and Altimetry, *Journal of Physical Oceanography*, *37*(12), 2838–2854, doi: 10.1175/2007JPO3567.1.

Holliday, N. P., A. Meyer, S. Bacon, S. G. Alderson, and B. de Cuevas (2007), Retroflection of part of the east Greenland current at Cape Farewell, *Geophysical Research Letters*, *34*(7), L07,609, doi: 10.1029/2006GL029085.

Holliday, N. P., S. Bacon, J. Allen, and E. L. McDonagh (2009), Circulation and Transport in the Western Boundary Currents at Cape Farewell, Greenland, *Journal of Physical Oceanography*, *39*(8), 1854–1870, doi: 10.1175/2009JPO4160.1.

Holliday, N. P., S. Bacon, S. A. Cunningham, S. F. Gary, J. Karstensen, B. A. King, F. Li, and E. L. Mcdonagh (2018), Subpolar North Atlantic Overturning and Gyre-Scale Circulation in the Summers of 2014 and 2016, *Journal of Geophysical Research: Oceans*, *123*(7), 4538–4559, doi: 10.1029/2018JC013841.

Holte, J., and F. Straneo (2017), Seasonal Overturning of the Labrador Sea as Observed by Argo Floats, *Journal of Physical Oceanography*, *47*(10), 2531–2543, doi: 10.1175/JPO-D-17-0051.1.

IPCC (2014), *Climate Change 2014: Synthesis Report. Contribution of Working Groups I, II and III to the Fifth Assessment Report of the Intergovernmental Panel on Climate Change*, [Core Writing Team, R.K. Pachauri and L.A. Meyer (eds.)]. IPCC, Geneva, Switzerland, 151 pp.

Jackson, L. C., R. Kahana, T. Graham, M. A. Ringer, T. Woollings, J. V. Mecking, and R. A. Wood (2015), Global and european climate impacts of a slowdown of the amoc in a high resolution gcm, *Climate Dynamics*, *45*(11), 3299–3316, doi: 10.1007/s00382-015-2540-2.

Jochumsen, K., M. Moritz, N. Nunes, D. Quadfasel, K. M. H. Larsen, B. Hansen, H. Valdimarsson, and S. Jonsson (2017), Revised transport estimates of the Denmark Strait overflow, *Journal of Geophysical Research: Oceans*, *122*(4), 3434–3450, doi: 10.1002/2017JC012803.

Johns, W. E., M. O. Baringer, L. M. Beal, S. A. Cunningham, T. Kanzow, H. L. Bryden, J. J. M. Hirschi, J. Marotzke, C. S. Meinen, B. Shaw, and R. Curry (2011), Continuous, Array-Based Estimates of Atlantic Ocean Heat Transport at 26.5 °N, *Journal of Climate*, *24*(10), 2429–2449, doi: 10.1175/2010JCLI3997.1.

Johnson, H. L., P. Cessi, D. P. Marshall, F. Schloesser, and M. A. Spall (2019), Recent Contributions of Theory to Our Understanding of the Atlantic Meridional Overturning Circulation, *Journal of Geophysical Research: Oceans*, *124*(8), 5376–5399, doi: 10.1029/2019JC015330.

Jones, D. C., G. Forget, B. Sinha, S. A. Josey, E. J. D. Boland, A. J. S. Meijers, and E. Shuckburgh (2018), Local and Remote Influences on the Heat Content of the Labrador Sea: An Adjoint Sensitivity Study, *Journal of Geophysical Research: Oceans*, *123*(4), 2646–2667, doi: 10.1002/2018JC013774.

Jones, H., and J. Marshall (1997), Restratification after Deep Convection, *Journal of Physical Oceanography*, *27*(10), 2276–2287, doi: 10.1175/1520-0485(1997)027<2276:RADC>2.0.CO;2.

Kanzow, T., S. A. Cunningham, D. Rayner, J. J.-M. Hirschi, W. E. Johns, M. O. Baringer, H. L. Bryden, L. M. Beal, C. S. Meinen, and J. Marotzke (2007), Observed Flow Compensation Associated with the MOC at 26.5 °N in the Atlantic, *Science*, *317*(5840), 938–941, doi: 10.1126/science.1141293.

Katsman, C. A., M. A. Spall, and R. S. Pickart (2004), Boundary Current Eddies and Their Role in the Restratification of the Labrador Sea*, *Journal of Physical Oceanography*, *34*(9), 1967–1983, doi: 10.1175/1520-0485(2004)034<1967:BCEATR>2.0.CO;2.

Katsman, C. A., S. S. Drijfhout, H. A. Dijkstra, and M. A. Spall (2018), Sinking of Dense North Atlantic Waters in a Global Ocean Model: Location and Controls, *Journal of Geophysical Research: Oceans,*, *123*(5), 3563–3576, doi: 10.1029/2017JC013329.

Kawasaki, T., and H. Hasumi (2014), Effect of freshwater from the West Greenland Current on the winter deep convection in the Labrador Sea, *Ocean Modelling*, *75*, 51–64, doi: 10.1016/j.ocemod.2014.01.003.

Khatiwala, S., and M. Visbeck (2000), An estimate of the eddy-induced circulation in the Labrador Sea, *Geophysical Research Letters*, *27*(15), 2277–2280, doi: 10.1029/1999GL011073.

Kuhlbrodt, T., A. Griesel, M. Montoya, A. Levermann, M. Hofmann, and S. Rahmstorf (2007), On the driving processes of the atlantic meridional overturning circulation, *Reviews of Geophysics*, *45*(2), doi: 10.1029/2004RG000166.

Kulan, N., and P. G. Myers (2009), Comparing two climatologies of the Labrador Sea: Geopotential and isopycnal, *Atmosphere-Ocean*, *47*(1), 19–39, doi: 10.3137/OC281.2009.

Large, W., and S. Yeager (2009), The global climatology of an interannually varying air–sea flux data set, *Climate Dynamics*, *33*(2), 341–364, doi: 10.1007/s00382-008-0441-3.

Large, W., J. McWilliams, and S. Doney (1994), Oceanic vertical mixing: A review and a model with a nonlocal boundary layer parameterization, *Reviews of Geophysics*, *32*(4), 363–403, doi: 10.1029/94RG01872.

Lavender, K., R. Davis, and W. Owens (2000), Mid-depth recirculation observed in the interior Labrador and Irminger seas by direct velocity measurements, *Nature*, *407*(6800), 66–9, doi: 10.1038/35024048.

Lazier, J., R. Hendry, A. Clarke, I. Yashayaev, and P. Rhines (2002), Convection and restratification in the Labrador Sea, 1990-2000, *Deep-Sea Research Part I: Oceanographic Research Papers*, *49*(10), 1819–1835, doi: 10.1016/S0967-0637(02)00064-X.

Lazier, J. R. N., and D. G. Wright (1993), Annual Velocity Variations in the Labrador Current, *Journal of Physical Oceanography*, *23*, 659–678, doi: 10.1175/1520-0485(1993)023<0659:AVVITL>2.0.CO;2.

Le Bras, I. A., I. Yashayaev, and J. M. Toole (2017), Tracking Labrador Sea Water property signals along the Deep Western Boundary Current, *Journal of Geophysical Research: Oceans*, *122*(7), 5348–5366, doi: 10.1002/2017JC012921.

Le Bras, I. A., F. Straneo, J. Holte, M. F. de Jong, and N. P. Holliday (2020), Rapid export of waters formed by convection near the irminger sea's western boundary, *Geophysical Research Letters*, *47*(3), doi: 10.1029/2019GL085989.

Li, F., and M. S. Lozier (2018), On the Linkage between Labrador Sea Water Volume and Overturning Circulation in the Labrador Sea: A Case Study on Proxies, *Journal of Climate*, *31*(13), 5225–5241, doi: 10.1175/JCLI-D-17-0692.1.

Li, F., M. S. Lozier, and W. E. Johns (2017), Calculating the Meridional Volume, Heat, and Freshwater Transports from an Observing System in the Subpolar North Atlantic: Observing System Simulation Experiment, *Journal of Atmospheric and Oceanic Technology*, *34*(7), 1483–1500, doi: 10.1175/JTECH-D-16-0247.1.

Lilly, J. M., and P. B. Rhines (2002), Coherent Eddies in the Labrador Sea Observed from a Mooring, *Journal of Physical Oceanography*, *32*(2), 585–598, doi: 10.1175/1520-0485(2002)032<0585:CEITLS>2.0.CO;2.

Lilly, J. M., P. B. Rhines, M. Visbeck, R. Davis, J. R. N. Lazier, F. Schott, and D. Farmer (1999), Observing Deep Convection in the Labrador Sea during Winter 1994/95, *Journal of Physical Oceanography*, *29*(8), 2065–2098, doi: 10.1175/1520-0485(1999)029<2065:ODCITL>2.0.CO;2.

Lilly, J. M., P. B. Rhines, F. Schott, K. Lavender, J. Lazier, U. Send, and E. D'Asaro (2003), Observations of the Labrador Sea eddy field, *Progress in Oceanography*, *59*(1), 75–176, doi: 10.1016/j.pocean.2003.08.013.

Lozier, M. S. (2012), Overturning in the North Atlantic, *Annual Review of Marine Science*, *4*(1), 291–315, doi: 10.1146/annurev-marine-120710-100740.

Lozier, M. S. (2015), Overturning Assumptions: Past, Present, and Future Concerns about the Ocean's Circulation, *Oceanography*, *28*(2), 240 – 251, doi: 10.5670/oceanog.2015.50.

Lozier, M. S., S. F. Gary, and A. S. Bower (2013), Simulated pathways of the overflow waters in the North Atlantic: Subpolar to subtropical export, *Deep Sea Research Part II: Topical Studies in Oceanography*, *85*, 147 – 153, doi: 10.1016/j.dsr2.2012.07.037.

Lozier, M. S., S. Bacon, A. S. Bower, S. A. Cunningham, M. Femke de Jong, L. de Steur, B. deYoung, J. Fischer, S. F. Gary, B. J. W. Greenan, P. Heimbach, N. P. Holliday, L. Houpert, M. E. Inall, W. E. Johns, H. L. Johnson, J. Karstensen, F. Li, X. Lin, N. Mackay, D. P. Marshall, H. Mercier, P. G. Myers, R. S. Pickart, H. R. Pillar, F. Straneo, V. Thierry, R. A. Weller, R. G. Williams, C. Wilson, J. Yang, J. Zhao, and J. D. Zika (2017), Overturning in the Subpolar North Atlantic Program: A New International Ocean Observing System, *Bulletin of the American Meteorological Society*, *98*(4), 737–752, doi: 10.1175/BAMS-D-16-0057.1.

Lozier, M. S., F. Li, S. Bacon, F. Bahr, A. S. Bower, S. A. Cunningham, M. F. de Jong, L. de Steur, B. deYoung, J. Fischer, S. F. Gary, B. J. W. Greenan, N. P. Holliday, A. Houk, L. Houpert, M. E. Inall, W. E. Johns, H. L. Johnson, C. Johnson, J. Karstensen, G. Koman, I. A. Le Bras, X. Lin, N. Mackay, D. P. Marshall, H. Mercier, M. Oltmanns, R. S. Pickart, A. L. Ramsey, D. Rayner, F. Straneo, V. Thierry, D. J. Torres, R. G. Williams, C. Wilson, J. Yang, I. Yashayaev, and J. Zhao (2019), A sea change in our view of overturning in the subpolar North Atlantic, *Science*, *363*(6426), 516–521, doi: 10.1126/science.aau6592.

Luo, H., A. Bracco, and F. Zhang (2014), The seasonality of convective events in the Labrador Sea, *J. Climate*, *27*, 6456–6471, doi: 10.1175/JCLI-D-14-00009.1.

MacGilchrist, G. A., H. L. Johnson, D. P. Marshall, C. Lique, M. Thomas, L. C. Jackson, and R. A. Wood (2020), Locations and mechanisms of ocean ventilation in the high-latitude North Atlantic in an eddy-permitting ocean model, *Journal of Climate*, pp. 1–61, doi: 10.1175/JCLI-D-20-0191.1.

Marotzke, J. (2012), A grip on ice-age ocean circulation, *Nature*, *485*(7397), 180–181, doi: 10.1038/485180a.

Marshall, J., and F. Schott (1999), Open-ocean convection: Observations, theory, and models, *Reviews of Geophysics*, *37*(1), 1–64, doi: 10.1029/98RG02739.

Marshall, J., A. Adcroft, C. Hill, L. Perelman, and C. Heisey (1997), A finite-volume, incompressible Navier Stokes model for studies of the ocean on parallel computers, *Journal of Geophysical Research*, *102*(C3), 5753–5766, doi: 10.1029/96JC02775.

Marshall, J. C., R. G. Williams, and A. J. G. Nurser (1993), Inferring the subduction rate and period over the north atlantic, *J. Phys. Oceanogr.*, *23*, 1315–1329, doi: 10.1175/1520-0485(1993)023<1315:ITSRAP>2.0.CO;2.

McCarthy, G., D. Smeed, W. Johns, E. Frajka-Williams, B. Moat, D. Rayner, M. Baringer, C. Meinen, J. Collins, and H. Bryden (2015), Measuring the Atlantic Meridional Overturning Circulation at 26 °N, *Progress in Oceanography*, *130*, 91 – 111, doi: 10.1016/j.pocean.2014.10.006.

McCarthy, G. D., P. J. Brown, C. N. Flagg, G. Goni, L. Houpert, C. W. Hughes, R. Hummels, M. Inall, K. Jochumsen, K. M. H. Larsen, P. Lherminier, C. S. Meinen, B. I. Moat, D. Rayner, M. Rhein, A. Roessler, C. Schmid, and D. A. Smeed (2020), Sustainable Observations of the AMOC: Methodology and Technology, *Reviews of Geophysics*, *58*(1), doi: 10.1029/2019RG000654.

Mercier, H., P. Lherminier, A. Sarafanov, F. Gaillard, N. Daniault, D. Desbruyères, A. Falina, B. Ferron, C. Gourcuff, T. Huck, and V. Thierry (2015), Variability of the meridional overturning circulation at the Greenland – Portugal OVIDE section from 1993 to 2010, *Progress in Oceanography*, *132*, 250–261, doi: 10.1016/j.pocean.2013.11.001.

Moat, B. I., D. A. Smeed, E. Frajka-Williams, D. G. Desbruyères, C. Beaulieu, W. E. Johns, D. Rayner, A. Sanchez-Franks, M. O. Baringer, D. Volkov, L. C. Jackson, and H. L. Bryden (2020), Pending recovery in the strength of the meridional overturning circulation at 26^oN, *Ocean Science*, *16*(4), 863–874, doi: 10.5194/os-16-863-2020.

Moore, G. W. K., I. A. Renfrew, and R. S. Pickart (2012), Spatial distribution of air-sea heat fluxes over the subpolar North Atlantic Ocean, *Geophysical Research Letters*, *39*(18), doi: 10.1029/2012GL053097.

Myers, P. G., N. Kulan, and M. H. Ribergaard (2007), Irminger Water variability in the West Greenland Current, *Geophysical Research Letters*, *34*(17), doi: 10.1029/2007GL030419.

Orlanski, I. (1976), A simple boundary condition for unbounded hyperbolic flows, *Journal of Computational Physics*, *21*, 251–269, doi: 10.1016/0021-9991(76)90023-1.

Palter, J. B., M. S. Lozier, and K. L. Lavender (2008), How Does Labrador Sea Water Enter the Deep Western Boundary Current?, *Journal of Physical Oceanography*, *38*(5), 968–983, doi: 10.1175/2007JPO3807.1.

Paquin, J.-P., Y. Lu, S. Higginson, F. Dupont, and G. Garric (2016), Modelled Variations of Deep Convection in the Irminger Sea during 2003–10, *Journal of Physical Oceanography*, *46*(1), 179–196, doi: 10.1175/JPO-D-15-0078.1.

Paris, C. B., J. Helgers, E. van Sebille, and A. Srinivasan (2013), Connectivity Modeling System: A probabilistic modeling tool for the multi-scale tracking of biotic and abiotic variability in the ocean, *Environmental Modelling & Software*, *42*, 47–54, doi: 10.1016/j.envsoft.2012.12.006.

Pedlosky, J., and M. A. Spall (2005), Boundary Intensification of Vertical Velocity in a β -Plane Basin, *Journal of Physical Oceanography*, *35*(12), 2487–2500, doi: 10.1175/JPO2832.1.

Pennelly, C., X. Hu, and P. G. Myers (2019), Cross-Isobath Freshwater Exchange Within the North Atlantic Subpolar Gyre, *Journal of Geophysical Research: Oceans*, *124*(10), 6831–6853, doi: 10.1029/2019JC015144.

Pickart, R. S., and M. A. Spall (2007), Impact of Labrador Sea Convection on the North Atlantic Meridional Overturning Circulation, *Journal of Physical Oceanography*, *37*(9), 2207–2227, doi: 10.1175/JPO3178.1.

Pickart, R. S., D. J. Torres, and R. A. Clarke (2002), Hydrography of the Labrador Sea during Active Convection, *Journal of Physical Oceanography*, *32*(2), 428–457, doi: 10.1175/1520-0485(2002)032<0428:HOTLSD>2.0.CO;2.

Pickart, R. S., F. Straneo, and G. Moore (2003), Is Labrador Sea Water formed in the Irminger basin?, *Deep Sea Research Part I: Oceanographic Research Papers*, *50*(1), 23 – 52, doi: 10.1016/S0967-0637(02)00134-6.

Pickart, R. S., D. J. Torres, and P. S. Fratantoni (2005), The East Greenland Spill Jet*, *Journal of Physical Oceanography*, *35*(6), 1037–1053, doi: 10.1175/JPO2734.1.

Piron, A., V. Thierry, H. Mercier, and G. Caniaux (2016), Argo float observations of basin-scale deep convection in the irminger sea during winter 2011–2012, *Deep Sea Research Part I: Oceanographic Research Papers*, *109*, 76 – 90, doi: 10.1016/j.dsr.2015.12.012.

Piron, A., V. Thierry, H. Mercier, and G. Caniaux (2017), Gyre-scale deep convection in the subpolar North Atlantic Ocean during winter 2014–2015, *Geophysical Research Letters*, *44*(3), 1439–1447, doi: 10.1002/2016GL071895.

Prater, M. D. (2002), Eddies in the Labrador Sea as Observed by Profiling RAFOS Floats and Remote Sensing, *Journal of Physical Oceanography*, *32*(2), 411–427, doi: 10.1175/1520-0485(2002)032<0411:EITLSA>2.0.CO;2.

Rahmstorf, S., M. Crucifix, A. Ganopolski, H. Goosse, I. Kamenkovich, R. Knutti, G. Lohmann, R. Marsh, L. A. Mysak, Z. Wang, and A. J. Weaver (2005), Thermohaline circulation hysteresis: A model intercomparison, *Geophysical Research Letters*, *32*(23), L23,605, doi: 10.1029/2005GL023655.

Rahmstorf, S., J. E. Box, G. Feulner, M. E. Mann, A. Robinson, S. Rutherford, and E. J. Schaffernicht (2015), Exceptional twentieth-century slowdown in atlantic ocean overturning circulation, *Nature Climate Change*, *5*(5), 475–480, doi: 10.1038/nclimate2554.

Randall, D., R. Wood, S. Bony, R. Colman, T. Fichefet, J. Fyfe, V. Kattsov, A. Pitman, J. Shukla, J. Srinivasan, R. Stouffer, A. Sumi, and K. Taylor (2007), Cilmate models and their evaluation, *In: Climate Change 2007: The Physical Science Basis. Contribution of Working Group I to the Fourth Assessment Report of the Intergovernmental Panel on Climate Change*, pp. [Solomon, S., D. Qin, M. Manning, Z. Chen, M. Marquis, K.B. Averyt, M.Tignor and H.L. Miller (eds.)]. Cambridge University Press, Cambridge, United Kingdom and New York, NY, USA.

Rhein, M., J. Fischer, W. M. Smethie, D. Smythe-Wright, R. F. Weiss, C. Mertens, D.-H. Min, U. Fleischmann, and A. Putzka (2002), Labrador Sea Water: Pathways, CFC Inventory, and Formation Rates, *Journal of Physical Oceanography*, *32*(2), 648–665, doi: 10.1175/1520-0485(2002)032<0648:LSWPCI>2.0.CO;2.

Rhein, M., D. Kieke, and R. Steinfeldt (2015), Advection of North Atlantic Deep Water from the Labrador Sea to the southern hemisphere, *Journal of Geophysical Research: Oceans*, *120*(4), 2471–2487, doi: 10.1002/2014JC010605.

Rhein, M., R. Steinfeldt, D. Kieke, I. Stendardo, and I. Yashayaev (2017), Ventilation variability of Labrador Sea Water and its impact on oxygen and anthropogenic carbon: a review, *Philosophical Transactions of the Royal Society A: Mathematical, Physical and Engineering Sciences*, *375*(2102), doi: 10.1098/rsta.2016.0321.

Rieck, J. K., C. W. Böning, and K. Getzlaff (2019), The Nature of Eddy Kinetic Energy in the Labrador Sea: Different Types of Mesoscale Eddies, Their Temporal Variability, and Impact on Deep Convection, *Journal of Physical Oceanography*, *49*(8), 2075–2094, doi: 10.1175/JPO-D-18-0243.1.

Roemmich, D., G. C. Johnson, S. Riser, R. Davis, J. Gilson, W. B. Owens, S. L. Garzoli, C. Schmid, and M. Ignaszewski (2009), The Argo Program: Observing the Global Ocean with Profiling Floats, *Oceanography*, *22*(2), 34 – 43, doi: 10.5670/oceanog.2009.36.

Rykova, T., F. Straneo, and A. S. Bower (2015), Seasonal and interannual variability of the West Greenland Current System in the Labrador Sea in 1993-2008, *Journal of Geophysical Research: Oceans*, *120*(2), 1318–1332, doi: 10.1002/2014JC010386.

Saenko, O. A., F. Dupont, D. Yang, P. G. Myers, I. Yashayaev, and G. C. Smith (2014), Role of Resolved and Parameterized Eddies in the Labrador Sea Balance of Heat and Buoyancy, *Journal of Physical Oceanography*, *44*(12), 3008–3032, doi: 10.1175/JPO-D-14-0041.1.

Sarafanov, A., A. Falina, H. Mercier, A. Sokov, P. Lherminier, C. Gourcuff, S. Gladyshev, F. Gaillard, and N. Daniault (2012), Mean full-depth summer circulation and transports at the northern periphery of the atlantic ocean in the 2000s, *Journal of Geophysical Research: Oceans*, *117*(C1), doi: 10.1029/2011JC007572.

Sayol, J.-M., H. Dijkstra, and C. Katsman (2019), Seasonal and regional variations of sinking in the subpolar North Atlantic from a high-resolution ocean model, *Ocean Science*, *15*(4), 1033–1053, doi: 10.5194/os-15-1033-2019.

Schott, F. A., and P. Brandt (2007), *Circulation and Deep Water Export of the Subpolar North Atlantic During the 1990's*, pp. 91–118, American Geophysical Union (AGU), doi: 10.1029/173GM08.

Schulze Chretien, L. M., and E. Frajka-Williams (2018), Wind-driven transport of fresh shelf water into the upper 30m of the Labrador Sea, *Ocean Science*, *14*(5), 1247–1264, doi: 10.5194/os-14-1247-2018.

Send, U., and J. Marshall (1995), Integral Effects of Deep Convection, *Journal of Physical Oceanography*, *25*(5), 855–872, doi: 10.1175/1520-0485(1995)025<0855:IEODC>2.0.CO;2.

Smeed, D. A., G. D. McCarthy, S. A. Cunningham, E. Frajka-Williams, D. Rayner, W. E. Johns, C. S. Meinen, M. O. Baringer, B. I. Moat, A. Duchez, and H. L. Bryden (2014), Observed decline of the Atlantic meridional overturning circulation 2004-2012, *Ocean Science*, *10*(1), 29–38, doi: 10.5194/os-10-29-2014.

Smeed, D. A., S. A. Josey, C. Beaulieu, W. E. Johns, B. I. Moat, E. Frajka-Williams, D. Rayner, C. S. Meinen, M. O. Baringer, H. L. Bryden, and G. D. McCarthy (2018), The North Atlantic Ocean Is in a State of Reduced Overturning, *Geophysical Research Letters*, *45*(3), 1527–1533, doi: 10.1002/2017GL076350.

Smith, R. D., M. E. Maltrud, F. O. Bryan, and M. W. Hecht (2000), Numerical Simulation of the North Atlantic Ocean at 1/10°, *Journal of Physical Oceanography*, *30*(7), 1532–1561, doi: 10.1175/1520-0485(2000)030<1532:NSOTNA>2.0.CO;2.

Solodoch, A., J. C. McWilliams, A. L. Stewart, J. Gula, and L. Renault (2020), Why Does the DeepWestern Boundary Current "Leak" Around Flemish Cap?, *Journal of Physical Oceanography*, doi: 10.1175/JPO-D-1-0247.1.

Spall, M. A. (2004), Boundary Currents and Watermass Transformation in Marginal Seas*, *Journal of Physical Oceanography*, *34*(5), 1197–1213, doi: 10.1175/1520-0485(2004)034<1197:BCAWTI>2.0.CO;2.

Spall, M. A. (2010), Dynamics of Downwelling in an Eddy-Resolving Convective Basin, *Journal of Physical Oceanography*, *40*(10), 2341–2347, doi: 10.1175/2010JPO4465.1.

Spall, M. A. (2011), On the role of eddies and surface forcing in the heat transport and overturning circulation in marginal seas, *Journal of Climate*, *24*(18), 4844–4858, doi: 10.1175/2011JCLI4130.1.

Spall, M. A. (2012), Influences of Precipitation on Water Mass Transformation and Deep Convection, *Journal of Physical Oceanography*, *42*(10), 1684–1700, doi: 10.1175/JPO-D-11-0230.1.

Spall, M. A., and R. S. Pickart (2001), Where Does Dense Water Sink? A Subpolar Gyre Example*, *Journal of Physical Oceanography*, *31*(3), 810–826, doi: 10.1175/1520-0485(2001)031<0810:WDDWSA>2.0.CO;2.

Spence, P., O. A. Saenko, W. Sijp, and E. M. (2012), The Role of Bottom Pressure Torques on the Interior Pathways of North Atlantic Deep Water, *Journal of Physical Oceanography*, *42*, 110–125, doi: 10.1175/2011JPO4584.1.

Spence, P., R. M. Holmes, A. M. Hogg, S. M. Griffies, K. D. Stewart, and M. H. England (2017), Localized rapid warming of West Antarctic subsurface waters by remote winds, *Nature Climate Change*, *7*(8), 595–603, doi: 10.1038/nclimate3335.

Srokosz, M., M. Baringer, H. Bryden, S. Cunningham, T. Delworth, S. Lozier, J. Marotzke, and R. Sutton (2012), Past, present, and future changes in the atlantic meridional overturning circulation, *Bulletin of the American Meteorological Society*, *93*(11), 1663–1676, doi: 10.1175/BAMS-D-11-00151.1.

Stramma, L., D. Kieke, M. Rhein, F. Schott, I. Yashayaev, and K. P. Koltermann (2004), Deep water changes at the western boundary of the subpolar North Atlantic during 1996 to 2001, *Deep Sea Research Part I: Oceanographic Research Papers*, *51*(8), 1033–1056, doi: 10.1016/j.dsr.2004.04.001.

Straneo, F. (2006a), On the Connection between Dense Water Formation, Overturning, and Poleward Heat Transport in a Convective Basin*, *Journal of Physical Oceanography*, *36*(9), 1822–1840, doi: 10.1175/JPO2932.1.

Straneo, F. (2006b), Heat and Freshwater Transport through the Central Labrador Sea*, *Journal of Physical Oceanography*, *36*(4), 606–628, doi: 10.1175/JPO2875.1.

Straneo, F. (2006c), On the Connection between Dense Water Formation, Overturning, and Poleward Heat Transport in a Convective Basin*, *Journal of Physical Oceanography*, *36*(9), 1822–1840, doi: 10.1175/JPO2932.1.

Straneo, F., R. S. Pickart, and K. Lavender (2003), Spreading of Labrador sea water: an advective-diffusive study based on Lagrangian data, *Deep-Sea Research Part I-Oceanographic Research Papers*, *50*(6), 701–719, doi: 10.1016/S0967-0637(03)00057-8.

Straneo, F., P. Heimbach, O. Sergienko, G. Hamilton, G. Catania, S. Griffies, R. Hallberg, A. Jenkins, I. Joughin, R. Motyka, W. T. Pfeffer, S. F. Price, E. Rignot, T. Scambos, M. Truffer, and A. Vieli (2013), Challenges to Understanding the Dynamic Response of Greenland's Marine Terminating Glaciers to Oceanic and Atmospheric Forcing, *Bulletin of the American Meteorological Society*, *94*, 1131–1144, doi: 10.1175/BAMS-D-12-00100.1.

Talley, L. D., and M. S. McCartney (1982), Distribution and Circulation of Labrador Sea Water, *Journal of Physical Oceanography*, *12*(11), 1189–1205, doi: 10.1175/1520-0485(1982)012<1189:DACOLS>2.0.CO;2.

Talley, L. D., G. L. Pickard, W. J. Emery, and J. H. Swift (2011), Chapter 9 - Atlantic Ocean, in *Descriptive Physical Oceanography (Sixth Edition)*, edited by L. D. Talley, G. L. Pickard, W. J. Emery, and J. H. Swift, sixth edition ed., pp. 245 – 301, Academic Press, Boston, doi: 10.1016/B978-0-7506-4552-2.10009-5.

Våge, K., R. S. Pickart, G. W. K. Moore, and M. H. Ribergaard (2008), Winter Mixed Layer Development in the Central Irminger Sea: The Effect of Strong, Intermittent Wind Events, *Journal of Physical Oceanography*, *38*(3), 541–565, doi: 10.1175/2007JPO3678.1.

Våge, K., R. S. Pickart, V. Thierry, G. Reverdin, C. M. Lee, B. Petrie, T. a. Agnew, A. Wong, and M. H. Ribergaard (2009), Surprising return of deep convection to the subpolar North Atlantic Ocean in winter 2007–2008, *Nature Geoscience*, *2*(1), 67–72, doi: 10.1038/ngeo382.

Våge, K., R. S. Pickart, A. Sarafanov, Ø. Knutsen, H. Mercier, P. Lherminier, H. M. van Aken, J. Meincke, D. Quadfasel, and S. Bacon (2011a), The Irminger Gyre: Circulation, convection, and interannual variability, *Deep Sea Research Part I: Oceanographic Research Papers*, *58*(5), 590–614, doi: 10.1016/j.dsr.2011.03.001.

Våge, K., R. S. Pickart, M. A. Spall, H. Valdimarsson, S. Jónsson, D. J. Torres, S. Østerhus, and T. Eldevik (2011b), Significant role of the North Icelandic Jet in the formation of Denmark Strait overflow water, *Nature Geoscience*, *4*(10), 723–727, doi: 10.1038/ngeo1234.

van Sebille, E., P. Spence, M. R. Mazloff, M. H. England, S. R. Rintoul, and O. A. Saenko (2013), Abyssal connections of Antarctic Bottom Water in a Southern Ocean State Estimate, *Geophysical Research Letters*, *40*(10), 2177–2182, doi: 10.1002/grl.50483.

van Sebille, E., S. M. Griffies, R. Abernathey, T. P. Adams, P. Berloff, A. Biastoch, B. Blanke, E. P. Chassignet, Y. Cheng, C. J. Cotter, E. Deleersnijder, K. Döös, H. F. Drake, S. Drijfhout, S. F. Gary, A. W. Heemink, J. Kjellsson, I. M. Koszalka, M. Lange, C. Lique, G. A. MacGilchrist, R. Marsh, C. G. M. Adame, R. McAdam, F. Nencioli, C. B. Paris, M. D. Piggott, J. A. Polton, S. Rühs, S. H. Shah, M. D. Thomas, J. Wang, P. J. Wolfram, L. Zanna, and J. D. Zika (2018), Lagrangian ocean analysis: Fundamentals and practices, *Ocean Modelling*, *121*, 49 – 75, doi: 10.1016/j.ocemod.2017.11.008.

Waldman, R., N. Brüggemann, A. Bosse, M. Spall, S. Somot, and F. Sevault (2018), Overturning the Mediterranean Thermohaline Circulation, *Geophysical Research Letters*, doi: 10.1029/2018GL078502.

Weijer, W., W. Cheng, S. S. Drijfhout, A. V. Fedorov, A. Hu, L. C. Jackson, W. Liu, E. L. McDonagh, J. V. Mecking, and J. Zhang (2019), Stability of the Atlantic Meridional Overturning Circulation: A Review and Synthesis, *Journal of Geophysical Research: Oceans*, *124*(8), 5336–5375, doi: 10.1029/2019JC015083.

Wunsch, C., and P. Heimbach (2006), Estimated Decadal Changes in the North Atlantic Meridional Overturning Circulation and Heat Flux 1993–2004, *Journal of Physical Oceanography*, *36*(11), 2012–2024, doi: 10.1175/JPO2957.1.

Xu, X., P. B. Rhines, and E. P. Chassignet (2016), Temperature-salinity structure of the North Atlantic circulation and associated heat and freshwater transports, *Journal of Climate*, *29*(21), 7723–7742, doi: 10.1175/JCLI-D-15-0798.1.

Xu, X., P. B. Rhines, and E. P. Chassignet (2018), On Mapping the Diapycnal Water Mass Transformation of the Upper North Atlantic Ocean, *Journal of Physical Oceanography*, *48*(10), 2233–2258, doi: 10.1175/JPO-D-17-0223.1.

Yashayaev, I., and A. Clarke (2008), Evolution of North Atlantic Water Masses Inferred from Labrador Sea Salinity Series, *Oceanography*, *21*(1), 30–45, doi: 10.5670/oceanog.2008.65.

Yashayaev, I., and J. W. Loder (2009), Enhanced production of Labrador Sea Water in 2008, *Geophysical Research Letters*, *36*(1), doi: 10.1029/2008GL036162.

Yashayaev, I., and J. W. Loder (2017), Further intensification of deep convection in the Labrador Sea in 2016, *Geophysical Research Letters*, *44*(3), 1429–1438, doi: 10.1002/2016GL071668.

Yashayaev, I., M. Bersch, and H. M. van Aken (2007), Spreading of the Labrador Sea Water to the Irminger and Iceland basins, *Geophysical Research Letters*, *34*(10), doi: 10.1029/2006GL028999.

Yeager, S., and G. Danabasoglu (2014), The Origins of Late-Twentieth-Century Variations in the Large-Scale North Atlantic Circulation, *Journal of Climate*, *27*(9), 3222–3247, doi: 10.1175/JCLI-D-13-00125.1.

Ypma, S., N. Brüggemann, S. Georgiou, P. Spence, H. Dijkstra, J. Pietrzak, and C. Katsman (2019), Pathways and watermass transformation of Atlantic Water entering the Nordic Seas through Denmark Strait in two high resolution ocean models, *Deep Sea Research Part I: Oceanographic Research Papers*, *145*, 59–72, doi: 10.1016/j.dsr.2019.02.002.

Ypma, S. L., M. A. Spall, E. Lambert, S. Georgiou, J. D. Pietrzak, and C. A. Katsman (2020a), The contrasting dynamics of the buoyancy-forced lofoten and greenland basins, *J. Phys. Oceanogr.*, *50*, 1227–1244, doi: 10.1175/JPO-D-19-0280.1.

Ypma, S. L., S. Georgiou, J. S. Dugstad, J. D. Pietrzak, and C. A. Katsman (2020b), Pathways and water mass transformation along and across the mohn-knipovich ridge in the nordic seas, *Journal of Geophysical Research: Oceans*, *125*(9), doi: 10.1029/2020JC016075.

Yu, L., X. Jin, and R. A. Weller (2008), Multidecade global flux datasets from the objectively analyzed air-sea fluxes (oaflux) project: Latent and sensible heat fluxes, ocean evaporation, and related surface meteorological variables, *Tech. rep.*, OAFlux Proj. Tech. Rep. OA-2008–01, Woods Hole Oceanogr. Inst., Woods Hole, Mass.

Zhang, R. (2010), Latitudinal dependence of Atlantic meridional overturning circulation (AMOC) variations, *Geophysical Research Letters*, *37*(16), doi: 10.1029/2010GL044474.

Zhang, W., and X. Yan (2018), Variability of the Labrador Sea Surface Eddy Kinetic Energy Observed by Altimeter From 1993 to 2012, *Journal of Geophysical Research: Oceans*, *123*(1), 601–612, doi: 10.1002/2017JC013508.

Zou, S., and M. S. Lozier (2016), Breaking the Linkage Between Labrador Sea Water Production and Its Advective Export to the Subtropical Gyre, *Journal of Physical Oceanography*, *46*(7), 2169–2182, doi: 10.1175/JPO-D-15-0210.1.

Zou, S., M. S. Lozier, F. Li, R. Abernathey, and L. Jackson (2020), Density-compensated overturning in the Labrador Sea, *Nature Geoscience*, *13*(2), 121–126, doi: 10.1038/s41561-019-0517-1.